University of Wollongong

Research Online

University of Wollongong Thesis Collection 2017+

University of Wollongong Thesis Collections

2022

Fabrication of relaxor-PT single crystals

Lkhagvasuren Baasandorj

Follow this and additional works at: https://ro.uow.edu.au/theses1

University of Wollongong

Copyright Warning

You may print or download ONE copy of this document for the purpose of your own research or study. The University does not authorise you to copy, communicate or otherwise make available electronically to any other person any copyright material contained on this site.

You are reminded of the following: This work is copyright. Apart from any use permitted under the Copyright Act 1968, no part of this work may be reproduced by any process, nor may any other exclusive right be exercised, without the permission of the author. Copyright owners are entitled to take legal action against persons who infringe their copyright. A reproduction of material that is protected by copyright may be a copyright infringement. A court may impose penalties and award damages in relation to offences and infringements relating to copyright material. Higher penalties may apply, and higher damages may be awarded, for offences and infringements involving the conversion of material into digital or electronic form.

Unless otherwise indicated, the views expressed in this thesis are those of the author and do not necessarily represent the views of the University of Wollongong.

Research Online is the open access institutional repository for the University of Wollongong. For further information contact the UOW Library: research-pubs@uow.edu.au

Fabrication of relaxor-PT single crystals

Lkhagvasuren Baasandorj, B.Sc., M.Sc.

Supervisors:
Prof. Shujun Zhang
Prof. Zhenxiang Cheng

This thesis is presented as part of the requirements for the conferral of the degree:
Doctor of Philosophy

University of Wollongong Institute for Superconducting and Electronic Materials
Australian Institute of Innovative Materials

February 2022

Abstract

The ultrahigh properties of relaxor–lead-titanate (relaxor-$PbTiO_3$) crystals have been proved to offer dramatic enhancements to electromechanical devices. The developmental stage of relaxor- $PbTiO_3$ (PT) ferroelectrical crystals comprises three generations. The class of binary $Pb(Zn_{1/3}Nb_{2/3})O_3$-$PbTiO_3$ (PZN-PT) and $Pb(Mg_{1/3}Nb_{2/3})O_3$-$PbTiO_3$ (PMN-PT) single crystals represents the first generation, which exhibits giant electromechanical properties and piezoelectric coefficients. The ternary system $Pb(In_{1/2}Nb_{1/2})O_3$-$Pb(Mg_{1/3}Nb_{2/3})O_3$-$PbTiO_3$ (PIN-PMN-PT) represents the second generation, which demonstrates a greater coercive field (E_C), a higher rhombohedral-to-tetragonal phase transition temperature (T_{r-t}) and a higher Curie temperature (T_C) than those of the first generation. The third generation is Mn-modified $Pb(In_{1/2}Nb_{1/2})O_3$-$Pb(Mg_{1/3}Nb_{2/3})O_3$-$PbTiO_3$ (Mn:PIN-PMN-PT), which possesses a higher mechanical quality factor (Q_m) than those of the first and second generations, while it maintains comparable piezoelectric responses to those of generations I and II.

There are several techniques for the growth of relaxor-PT single crystals. Flux growth is a simple method, but its small output is inconvenient for mass production. The solid-state conversion growth (SSCG) method offers large quantities of single crystals. Furthermore, its operation is simple and cost-effective. The quality of the single crystal is low, however, due to porosity and defects. The modified Bridgman method is a straightforward way of synthesizing large quantities of relaxor-PT crystals. Single crystals are directly grown from a molten ingot passing through a temperature gradient and the solidus line of the solid solution phase diagram. Compositional segregation is an unavoidable disadvantage of this method, although several modifications have introduced to overcome this issue. Rare-earth doping and a continuous feeding approach have been confirmed to produce single crystals with only low segregation.

In this work, PMN-PT, Sm-modified PMN-PT, and Mn-modified PIN-PMN-PT single crystals are grown using the modified Bridgman method. A new vertical Bridgman furnace was assembled in the Institute for Superconducting and Electronic Materials, Australian Institute of Innovative Materials, University of Wollongong. Ceramic materials were prepared using the two-step precursor method. Optimal conditions for ceramic synthesis have been studied. The dielectric and piezoelectric properties of ceramic materials were investigated and confirmed to be good when compared them to reference values. PMN-PT single crystal was grown first. The physical appearance of the as-grown crystal was cloudy, and several grains were developed, as seen from cross-sectional view. The bottom part of the as-grown single crystal was also un-melted. The reason for these issues was that the charge was lifted to a position where the raw ceramic was not able to melt completely. Therefore, only the part in tapered section of the Pt crucible was melted, from which the crystallization was started with different grains. Learning from the first growth experiment, the next crystal growths were carefully carried out with operational condition’s changes. The growth procedure was carried out with a higher charge position and higher temperature in the upper zone to generate a greater temperature gradient. Consequently, pure and high quality Sm-modified PMN-PT and Mn-modified PIN-PMN-PT single crystals were grown.

The recent development of relaxor-PT ferroelectric single crystals is also reviewed in this work. This review includes the growth methods, property improvement strategies, and application prospects based on the recent progress.

Certification

I, Lkhagvasuren Baasandorj, declare that this thesis submitted in fulfilment of the requirements for the conferral of the degree Doctor of Philosophy, from the University of Wollongong, is wholly my own work unless otherwise referenced or acknowledged. This document has not been submitted for qualifications at any other academic institution.

Lkhagvasuren Baasandorj

21st February 2022

Acknowledgment

First of all, I would like to sincerely thank Professor Shujun Zhang for giving me the opportunity to conduct this research. Studying for a graduate degree in materials science was my dream for a long time. I received this chance from Professor Shujun Zhang and the University of Wollongong. His support, guidance, advice, and patience helped me complete this study. I also thank my co-supervisor Professor Zhenxiang Cheng for his support during my study. I would like to offer special thanks to Assistant Professor Zibin Chen at the Hong Kong Polytechnic University, the co-author my review article. His contribution and comments on my manuscript helped the publication of this article.

I also want to express my gratitude to my teammates Dr. Alain Moriana, Dr. Letao Yang, Dr. Xi Kong, and Dr. Xiaoyi Gao. Alain Moriana and I worked together to prepare ceramic samples. He was always willing to help me and share his ideas and experience. Xiaoyi Gao guided me on the details of sample preparation and shared his opinions when I needed to improve sample preparation. Letao Yang and Xi Kong always assisted me, especially on technical issues. Letao Yang shared his invaluable expertise and assisted me in measurements of properties and data treatment.

I am grateful to the Workshop & Process Facilities Manager Mr. Mathew Davies, Senior Technical Officer Mr. Paul Hammersley, and Technical Officers Mr. John Wilton and Mr. Anthony Zanatto. Without technical assistance from these people, it would have been very hard to assemble the high-temperature Bridgman furnace in our laboratory and to solve the technical issues relating to it.

I would like to express my thanks to the ISEM/AIIM administration and management team, ISEM director Professor Xiaolin Wang, Associate Professor Germanas Peleckis, Mrs. Crystal Mahfouz, Ms. Naomi Davies, Ms. Renae Clark, and Ms. Narelle Badger for administrative support. Furthermore, I would like to thank Ms. Joanne George and Dr. Candace Gabelish for their assistance on safe operation of the laboratory. I want to express special thanks to Dr. Tania Silver for helping to edit my manuscripts.

I would like to thank my family; my dear wife and my lovely two daughters. My wife's love, trust and encouragement have always inspired me. I am always motivated my dear father and mother's affection and trust. Thank you, my parents. Also, I want to thank my father-in-law and mother-in-law. I am motivated by their affection, caring and trust as well.

Contents

List of figures

List of tables

List of abbreviations and symbols

Relaxor-PT	Relaxor-$PbTiO_3$
PMN-PT	$Pb(Mg_{1/3}Nb_{2/3})O_3$-$PbTiO_3$
Sm-PMN-PT	Sm-modified $Pb(Mg_{1/3}Nb_{2/3})O_3$-$PbTiO_3$
Mn-PIN-PMN-PT	Mn-modified $Pb(In_{1/2}Nb_{1/2})O_3$-$Pb(Mg_{1/3}Nn_{2/3})O_3$
MPB	Morphotropic phase boundary
BM	Bridgman method
SSCG	Solid state conversion growth
PMN	$Pb(Mn_{1/3}Nb_{2/3})O_3$
PZN-PT	$Pb(Zn_{1/3}Nb_{2/3})O_3$-$PbTiO_3$
PSN-PMN-PT	$Pb(Sc_{0.5}Nb_{0.5})O_3$-$Pb(Mg_{1/3}Nb_{2/3})O_3$-$PbTiO_3$
PMN-PZT	$Pb(Mg_{1/3}Nb_{2/3})O_3$-$PbZrO_3$-$PbTiO_3$
PNRs	Polar nano-regions
CORs	Chemically ordered regions
ODRs	Octahedral distortion regions
ODRs	Octahedral tilt regions
DCP	Direct current (electric-field) poling
ACP	Alternating current (electric-field) poling
DC	Direct current
XRD	X-ray diffraction
CFBG	Continuous feeding Bridgman method
AGG	Abnormal grain growth
C	Capacitance
p	Pyroelectric coefficient

ε_r	Relative permittivity
ε_0	Permittivity of vacuum
$\tan\delta$	Dielectric loss
k	Electromechanical coupling factor
d	Piezoelectric strain coefficient
g	piezoelectric voltage coefficient
V	Voltage
E	Electric field
D	Electric displacement
S	Strain
f	Frequency
Q_m	Mechanical quality factor
T_C	Curie temperature
T_m	dielectric maximum temperature
$T_{f\text{-}f}$	Ferroelectric-to-ferroelectric phase transition temperature
$T_{r\text{-}t}$	Rhombohedral to tetragonal phase transition temperature
E_C	Coercive field
M_A, M_B, M_C	Monoclinic phase
R	Rhombohedral phase
O	Orthorhombic phase
T	Tetragonal phase
E_i	internal field
A	sample area covered by electrode
C-V	Capacitance-voltage

Chapter 1. Statement of problem

The extraordinary properties of relaxor-$PbTiO_3$ (relaxor-PT) single crystals endow them with great potential for dramatic improvement of electromechanical devices. Fabrication of single crystals with sufficient quantity and high quality is important, however, for utilising them in practical applications.

The relaxor-PT single crystals are grown using several methods. The flux method is a good way of growing high quality single crystal, but its small quantity of product is not adequate for mass commercialization. The solid-state conversion growth (SSCG) method can synthesize large quantities of single crystals. Furthermore, operation of this growth method is simple. The single crystals' qualities, such as the existence of porosity and defects, are inferior to those produced by the melt growth methods, which makes it disadvantageous. It is therefore crucial to use a growth method that can grow the single crystals with high quality and in large quantity.

This research aims to grow high quality relaxor-PT single crystals by using the modified Bridgman method. The modified Bridgman method is a straightforward way of growing single crystals. In this method, the single crystals grow directly from a molten ingot passing through a temperature gradient and the solidus line of the solid solution phase diagram. This method can also produce large quantities for scientific and industrial demands.

In this work, $Pb(Mg_{1/3}Nb_{2/3})O_3$-$PbTiO_3$ (PMN-PT), Sm-modified $Pb(Mg_{1/3}Nb_{2/3})O_3$-$PbTiO_3$ (Sm-PMN-PT) and Mn-modified $Pb(In_{1/2}Nb_{1/2})O_3$-$Pb(Mg_{1/3}Nb_{2/3})O_3$ (Mn-PIN-PMN-PT) single crystals were grown. Binary PMN-PT single crystal as a first generation relaxor-PT demonstrated a great piezoelectric coefficient and a giant electromechanical coupling factor. The addition of samarium as a donor to the PMN-PT system offers the greatest enhancements of piezoelectric and dielectric properties. Binary single crystals, however, exhibited low Curie temperatures, low ferroelectric-to-ferroelectric phase transition temperatures, and low mechanical quality factors, which limits their potentials in actuator and sensor applications. The acceptor dopant $Mn^{2+/3+}$ was added to ternary PIN-PMN-PT single crystal and proved to offer higher mechanical quality and lower loss than its binary counterparts. Hence, Mn-PIN-PMN-PT single crystals offer broader relaxor-PT applications in transducers.

Furthermore, this thesis reviews the recent development of relaxor-PT ferroelectric crystals. This review includes the recent progress on single crystal growth methods, strategies for property improvements and perspectives on applications.

Organization of thesis

The second chapter contains a literature review. This includes general concepts related to ferroelectricity, the unique properties of relaxor-PT single crystals and recent property improvements. This chapter also defines the growth methods for single crystals. The third chapter reviews the latest developments of studies on relaxor-PT single crystals. Chapter 4 describes the fabrication methods for the ceramics and their properties. In Chapter 5, the results on the single crystals and their growths are presented. Finally, the conclusions are discussed in Chapter 6.

Chapter 2. Literature review

2.1 Background on piezoelectricity and ferroelectricity

2.1.1 Dielectric permittivity

The dielectric property is the ability of a dielectric material to store charge under an applied electric field. The dielectric property is defined by the relative dielectric permittivity $\varepsilon_{r(ij)}$, that, is the ratio of the dielectric permittivity ε_{ij} to the permittivity of free space ε_0 [1]. The dielectric permittivity includes real and imaginary components expressed as follows:

$$\varepsilon_{ij}'' = \varepsilon_{ij}' \cdot \tan\delta \qquad (2.1)$$

Here, ε_{ij}', ε_{ij}'' and $\tan\delta$ are real component of the dielectric permittivity, the imaginary component, and the dielectric loss, respectively.

2.1.2 Piezoelectricity and related coefficients

Certain materials can be made to generate electric charge by applied mechanical force due to their crystal asymmetry. This phenomenon is called the direct piezoelectric effect. Conversely, such materials also develop strain under an applied electric field. This is called the converse piezoelectric effect [1]. Piezoelectric properties are expressed by four independent variables, including strain (*S*), stress (*T*), dielectric displacement (*D*), and electric field (*E*). Several independent piezoelectric coefficients are derived from the relationships of these variables [1]. The piezoelectric strain (or charge) coefficient *d* is defined as:

$$d = \left({}^{\partial S}/_{\partial E}\right)_T = \left({}^{\partial D}/_{\partial T}\right)_E. \qquad (2.1)$$

Here, the subscript *T* and *E* means constant stress and electric field, respectively.

Conversely, the piezoelectric voltage coefficient *g* is derived from the voltage response to applied stress or the strain in response to a dielectric displacement:

$$g = \left(-{}^{\partial E}/_{\partial T}\right)_D = \left({}^{\partial S}/_{\partial D}\right)_T. \qquad (2.2)$$

Piezoelectric stress coefficient e is the stress response to applied electric field under constant strain or the charge response to strain at a constant electric field:

$$e = \left(-{\partial T}/{\partial E}\right)_S = \left({\partial D}/{\partial S}\right)_E. \tag{2.3}$$

Another coefficient is the piezoelectric stiffness h, which is defined when S and D are independent variables;

$$h = \left(-{\partial T}/{\partial D}\right)_S = \left({\partial E}/{\partial S}\right)_D \tag{2.4}$$

In addition, the piezoelectric coefficients are related to each other [2]:

$$\begin{aligned} d_{mi} &= \varepsilon_{nm}^{T} g_{ni} = e_{mj} s_{ji}^{E}, \\ g_{mi} &= \beta_{nm}^{T} d_{ni} = h_{mj} s_{ji}^{D}, \\ e_{mi} &= \varepsilon_{nm}^{S} h_{ni} = d_{mj} c_{ji}^{E}, \\ h_{mi} &= \beta_{nm}^{S} e_{ni} = g_{mj} c_{ji}^{D}. \end{aligned} \tag{2.5}$$

Here, ε is the permittivity, and β is the dielectric impermeability. The superscripts (T, E, D, S)describe the boundary conditions, and m, n = 1 to 3. The i, j subscripts define the different axes, and i, j = 1 to 6.

2.1.3 Ferroelectricity and related phenomena

Ferroelectricity is defined as the existence of spontaneous polarization in certain materials. An electric field could reorient an existing polarization to more than one direction. This reorientated polarization could be reversed under electric field. The materials with reversible polarization are called ferroelectric materials. As the temperature rises, the ferroelectric phase is transformed to the paraelectric phase. The temperature at which a phase transition from ferroelectric to paraelectric occurs is Curie temperature, T_C. Below T_C, ferroelectric materials could possess a certain compositional boundary that separates two different symmetric phases. Such a boundary composition is the morphotropic phase boundary (MPB). Under a certain amount of electric field, due to domain switching, the relationship between polarization and electric field in ferroelectric materials appears as a *ferroelectric hysteresis loop*, which is another important characteristic of ferroelectrics [1,2].

2.1.4 Pyroelectricity

When a material with a non-symmetrical centre is homogenously heated up, the magnitude of its dipole moment changes. Thermal expansion causes piezoelectric stress in the crystal structure and generates a *polarization*. This dipole effect is the *pyroelectric effect*. The pyroelectric coefficient describes the pyroelectric effect as follows [2]:

$$p_m = \partial P_{sm}/\partial \boldsymbol{T}. \tag{2.6}$$

Here, p is the pyroelectric coefficient with units C m^{-2} K^{-1}, P_s is the spontaneous polarization, and $\boldsymbol{T}$ is the temperature, while $m = 1, 2, 3$.

2.1.5 Electromechanical coupling factor

The electromechanical coupling factor, k, identifies the degree of energy conversion and is expressed as the fraction of electrical energy transformed to mechanical energy (or vice versa when stress is applied as mechanical energy) [1]:

$$k^2 = \frac{converted\ energy}{input\ energy}\ . \tag{2.7}$$

The factor k is related to the piezoelectric coefficients [2, 3]:

$$k_{mi}^2 = \frac{d_{mi}^2}{s_{ii}^E \varepsilon_{mm}^T} = \frac{e_{mi}^2}{\varepsilon_{ii}^S c_{mm}^D} = \frac{g_{mi}^2}{s_{ii}^E \beta_{mm}^T} = \frac{h_{mi}^2}{\beta_{mm}^S c_{ii}^D}. \tag{2.8}$$

2.1.6 Mechanical quality factor.

There is some loss of energy when mechanical energy applied to a piezoelectric element. The reciprocal quantity of this loss is the so-called mechanical quality factor, Q_m, expressed as follows [3]:

$$Q_m = 2\pi \cdot \frac{W_m}{w_m}\ . \tag{2.9}$$

Here, within one complete vibration cycle, W_m is the total mechanical energy and w_m is the loss of the mechanical energy.

2.2 Relaxor–ferroelectrics and their properties

2.2.1 Development of relaxor-ferroelectric single crystals

Relaxors or relaxor-ferroelectrics are structurally long range disordered materials that possess unique structures and extraordinary properties. Macroscopically, several characteristics distinguish them from normal ferroelectrics. In their dielectric response, relaxors do not reveal an exact Curie temperature (T_C) for the ferroelectric-to-paraelectric phase transition, only a temperature range. Furthermore, the temperatures of both the maximum dielectric constant and the maximum dielectric loss are strongly dependent on the frequency of the applied field. Relaxors also show a strong frequency dispersion near the temperature of maximum dielectric constant [4,5].

The development of relaxor-PT materials: 1960s, Pb-based relaxor materials showed high dielectric constants [6]. Among these materials, $Pb(Mg_{1/3}Nb_{2/3})O_3$ (PMN) showed exceptional dielectric and electrostrictive properties reported in the 1980s [4,7]. PMN was also revealed to have more enhanced properties with the addition of the classic ferroelectric $PbTiO_3$ (PMN-PT solid solution) [8]. The two-step precursor method made it possible to produce pure perovskite PMN ceramic, avoiding the parasitic phases and increasing the material's dielectric property even further [9]. In the early 1980s, $Pb(Zn_{1/3}Nb_{2/3})O_3$-$PbTiO_3$ (PZN-PT) single crystal was synthesized by the flux growth technique and showed an ultrahigh piezoelectric coefficient of $d_{33} > 1500$ pm/V and a large electromechanical coupling factor of $k_{33} = 0.92$ [10]. In 1997, a breakthrough in piezoelectric and electromechanical properties was discovered in PMN-PT and PZN-PT single crystals, where giant $d_{33} > 2500$ pC/N and $k_{33} > 0.90$ were observed [11]. This started the first generation of relaxor-PT single crystal [10-16]. Despite ultra-high piezoelectric and electromechanical properties, the first-generation crystals exhibited low values of their ferroelectric-to-ferroelectric phase transition temperature ($T_{f\text{-}f}$), Curie temperature, and coercive field (E_C), so these characteristics limited usage of the first generation for broad areas of electromechanical applications. The ternary single crystals, including $Pb(Sc_{0.5}Nb_{0.5})O_3$-$Pb(Mg_{1/3}Nb_{2/3})O_3$-$PbTiO_3$ (PSN-PMN-PT), $Pb(In_{1/2}Nb_{1/2})O_3$-$Pb(Mg_{1/3}Nb_{2/3})O_3$-$PbTiO_3$ (PIN-PMN-PT), $Pb(Mg_{1/3}Nb_{2/3})O_3$-$PbZrO_3$-$PbTiO_3$ (PMN-PZT-PT) systems were also intensively studied [17-22]. The ternary single crystals demonstrated higher $T_{f\text{-}f}$, T_C, and E_C than the first generation crystals. Therefore, ternary single crystals as generation II crystals broadened practical usage of relaxor-PT crystals due to such features as their wider temperature range. Owing to their high mechanical loss and low mechanical quality factor, however, generation I and II single crystals are not feasible for use in high power transducer and actuator applications. Acceptor-doping in ternary relaxor-PT enabled improvement of mechanical coupling and reduction of loss [23-25]. Mn-doped PIN-PMN-PT single crystals as third generation relaxor-PTs revealed high mechanical quality and high electromechanical coupling factor while retaining comparable piezoelectric properties to earlier generations, making them promising candidates for high power applications [25,26].

2.2.2 Domain engineering

Ferroelectric crystals have equally possible domain variants due to energetic degeneration, so they are macroscopically non-polar. The boundary regions between these domain variants are known as *domain walls*. Some domain polarizations are antiparallel to each other and denoted as 180° domains. An electric force could move them, so the walls are known as ferroelectric domain walls. In the case of other domains, their polarizations are oriented by different angles between them, so they are called non-180° domains. Non-180° domain walls could be shifted by both electric force and mechanical stress. They are thus called *ferroelectric-ferroelastic* domain walls. Using a sufficient external force, the differently-oriented domains could be driven into a desired direction. Such a force is called the coercive field, E_C for the electric coercive field and, σ_C for the coercive stress. When relaxor-PT is poled along one of the crystallographic directions, different domain configurations or single domains will be formed. For instance, when the tetragonal phase is poled along the [111], [011], and [001] directions, this will form the 3T, 2T and 1T domain configurations, respectively shown in **figure 2.1a**. When the rhombohedral phase is poled along the [111], [011], and [001] directions, this will achieve 1R, 2R, and 4R configurations, respectively shown in **figure 2.1b**. In the case of orthorhombic phase, the 3O, 1O, and 4O domain configurations are respectively achieved when the crystal is poled along the [111], [011], and [001] directions [3,27-29]. Such formation of domain structures is the so-called "domain engineering" [27]. Through domain engineering, domain variants could be controlled.

2.2.3 Properties of relaxor-PT ferroelectric crystals

To discuss the properties of relaxor-PT single crystals, the boundary conditions/factors, including temperature, composition, orientation, or external force, should be considered. Variation of the permittivity above the dielectric maximum temperature, T_m, corresponds to the following empirical expression:

$$\frac{1}{\varepsilon} = \frac{1}{\varepsilon_m} + \frac{(T - T_m)^\gamma}{C'}. \tag{2.10}$$

Here, ε_m is the dielectric maximum, T_m is dielectric maximum temperature, C' is a constant, and γ is the diffusiveness exponent. In practice, the value of γ is between 1 and 2 for (1-x)PMN-xPT and (1-x)PZN-xPT. If γ is close to 1, then composition is more ferroelectric, while if it approaches to 2, the composition will behave as a more relaxor. The composition dependent properties of the relaxor-PT ferroelectric crystals have been intensively studied [10,30-44].

The temperature dependence of the dielectric constant for these materials curve shows that the relaxor behaviour becomes dominant with decreasing PT content, while ferroelectric features arise with increasing PT [30-35]. Generally, dielectric and ferroelectric properties in relaxor-ferroelectrics correspond to three states, depending on the temperature range [5]. In state 1, high dielectric permittivity over a range of temperatures is observed, which is attributed to the nanoscale polar regions [4,6]. In state 2, dielectric relaxation as a distinct character of the relaxors and relaxor-ferroelectrics are observed [5,36]. The long-range macroscale domains are transformed into microscale polar domains when a threshold field is applied [36-38]. Polarization-electric field loops in this state becomes slim nonlinear figures due to the microdomain's easy response to the field [39]. Long-range ferroelectric domains are obtained in state 3 with an external field in relaxor-ferroelectrics. High remnant polarization could be achieved in this state [5,36]. Therefore, high piezoelectric properties are observed, especially in the region of the MPB. The polarization-electric field loops turn into 'square' shapes [39]. Ferroelectric to

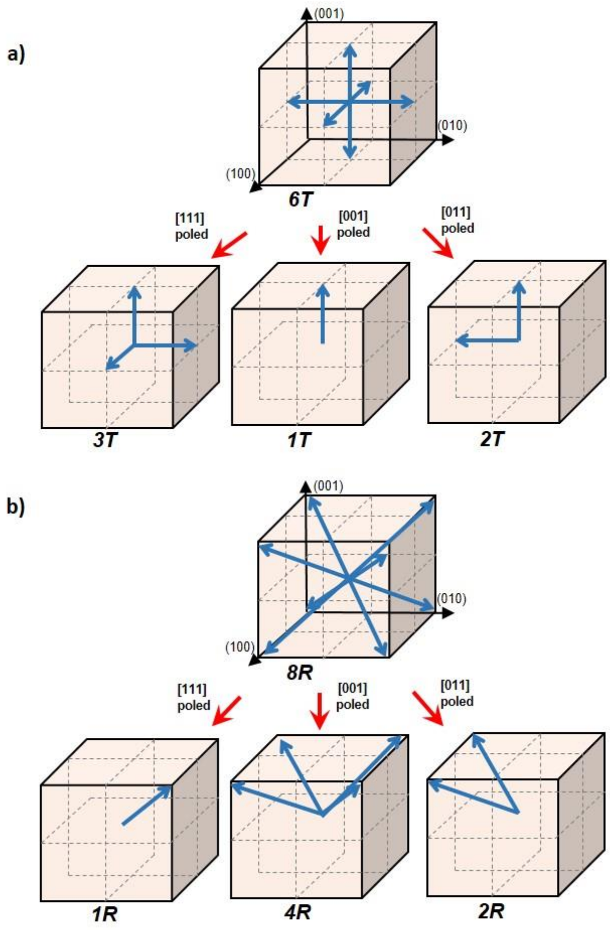

Figure 2.1 Domain configurations a) for tetragonal phase and b) for rhombohedral phase.

ferroelectric phase transitions also occur in state 3. Near the MPB compositions in PMN-PT and PZN-PT single crystals, the phase transition sequence follows: rhombohedral to monoclinic (M_B), monoclinic (M_B) to monoclinic (M_C) and monoclinic (M_C) to tetragonal, occurring as the temperature is increasing with an applied electric field. In this sequence, rhombohedral phase passes through two monoclinic phases in order to transform into tetragonal phase [10,28,30,32,40-44]. Monoclinic phase planes and their rotation directions are shown in **Figure 2.2**.

The influence of electric field on the properties of the relaxor-PT crystals is discussed in section 3.1.1.1.

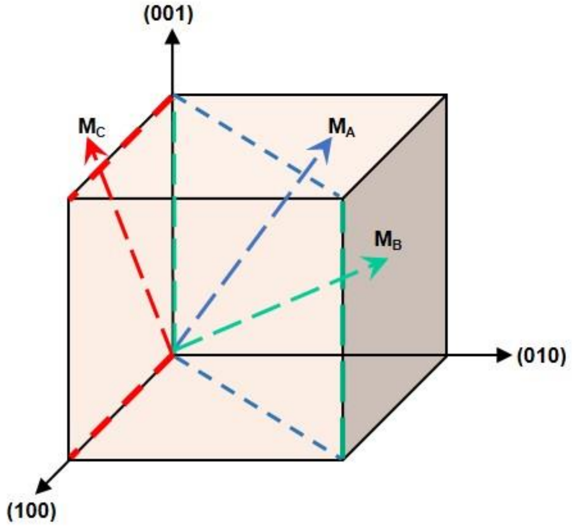

Figure 2.2 Monoclinic phases and their rotation planes.

Mechanical force (stress) changes the properties of the relaxor-PT single crystals [40,45-51]. When a compressive stress (longitudinal force) is applied to the domain-engineered “4R” configuration of relaxor-PT crystal, the polar vector rotates from the $\langle 111\rangle_C$ to the $\langle 011\rangle_C$ direction. The strain and piezoelectric coefficient d_{33} will be enhanced as the stress increases until the loading reaches a certain magnitude [40,46,50,51]. These increases are attributed to the boundary region or intermediate phase region generated by the mechanical loading [46,51]. Then, when the stress increases further, it will lead to the stress-induced *R*-to-*O* phase transition (a first order phase transition). After the phase transition has occurred, both the strain and d_{33} will drop due to the depolarization [40,47-51]. When a transverse stress is applied to the “4R” configuration, its polarization along $[111]_C$ direction rotates towards the $(0\bar{1}0)$ plane [40]. Further increasing stress (to a threshold value) results in a rhombohedral-to-orthorhombic phase transition, another first order phase transition. After the removal of the mechanical loading, the polar vector will be preserved. Under mechanical force, it is suggested that the *R*-to-*O* phase transition occurs via an intermediate *M* phase [40,46].

The potential for usage of both electrical and mechanical forces in the relaxor-ferroelectric single crystals is significant for practical applications [3,26,52]. An electric field along the $[001]_C$ direction suppresses the compressive-stress-generated hysteresis in charge-stress and strain-stress loops [40,46-48]. The electric force here is opposite to the mechanical force, so the rhombohedral polarization is stabilized, leading to higher threshold stress for the phase transition [46-48]. Within a certain electric field range, the stress-dependent ferroelastic and ferroelectric responses will be linearized [47,49]. If the electric bias is applied along the $[011]_C$ direction when compressive stress is loaded, this will lower the energy barrier against polarization rotation along the $(1\bar{1}0)$ plane, and the threshold stress is reduced [49].

2.3 Polar nano regions

Polar nano regions (PNRs) are expected to make a tremendous contribution to the giant electromechanical coupling factor and ultrahigh dielectric property in relaxor-PT single crystals [4,53-56]. This section will briefly discuss polar PNRs and their influence on the piezoelectric property.

2.3.1 Local order

Nanoscale polarization is believed to be related to the compositional local order. In the ground state or in a perfect ferroelectric, each cation, B′ and B″, of complex perovskite $A(B'B'')O_3$ must be placed at its own octahedral sublattice position, creating a complete ordering or superstructure, although such an ordered superstructure is not possible in reality. Diffuse site exchange between the B′ and B″ cations (relaxation) creates the ordering for a certain characteristic time. For PMN, such a diffuse exchange takes too a long time, and its compositional order is quenched below the critical temperature T_B. Consequently, inhomogeneous order-disorder regions are generated in the perovskite structure [56]. The true behaviour of these regions is debatable, however. Different models and reports have been suggested. Earlier experimental results showed 1:1 (Mg:Nb) B-site ordered regions embedded in 1:2 B-site disordered regions, and such chemically ordered regions (CORs) existed at the size of 2 to 5 nm [57-59]. Chemically ordered regions were initially modelled as charge-imbalanced with negative charge, so that they were surrounded by Nb-dominant positively charged disordered regions [57,60]. By contrast, Davies and Akbas reported that CORs were charge-balanced by a random distribution of Mg cations and increased the ordered regions by either thermal treatment or ferroelectric-active substitutions [61]. The Mg/Nb ratio was determined to be fluctuating within both ordered and disordered regions, and the fluctuation is stronger in the boundary between the two chemical regions [62]. Cabral *et al.*, also reported that the degree of the ordering is not uniform but forms a gradient, reducing smoothly from the centre of the COR to the boundary. Such a reduction was measured by an "order metric" [63]. Local heterogeneity was found in anion ordering as well. Oxygen displacement was discovered by neutron elastic diffuse scattering measurements [64]. Using advanced scanning transmission electron microscopy (STEM), the oxygen anions were found to be not only distorted, but also tilted in perovskite octahedral sites, so octahedral distortion regions (ODRs) and octahedral tilt regions (ODRs) also existed. It was further found that the maxima of local polarization was at or near these heterogeneous regions [65]. All local heterogeneities lead to PNRs.

2.3.2 Polar nano regions

Burn and Dacol first observed the presence of microscale polar regions from refraction index measurement in PMN [53]. Experimentally, neutron and X-ray elastic diffuse scattering measurements are widely used to study the behaviour of PNRs in Pb-based relaxor-ferroelectrics. The common feature of neutron scattering is the appearance of "butterfly-shaped" diffuse scattering near the Burn temperature, T_d, with increasing intensity on cooling [66]. Such a diffuse scattering in PMN is distinguished from that of normal ferroelectric $Pb(Zr_{1-x}Ti_x)O_3$ in the background state [67]. This diffuse scattering is therefore believed to represent the emergence of PNRs and relaxor behaviour.

Stock *et al*. used a comparison study of two techniques, the so-called cold-neutron backscattering and the spin-echo technique, and suggested that there are two components of diffuse scattering in PMN. The first one is static and starts near 420 K, corresponding to static PNRs, and the other shows dynamic scattering, in accordance with dynamic PNRs near 450 K. The dynamic component has the highest intensity at 300 K and disappears at 200 K, where PNRs totally freeze [67]. The nano polar vector is oriented to the $[111]_C$ direction in the PMN system [68]. Interestingly, when an electric field is applied along the $[111]_C$ direction to $Pb(Zn_{1/3}Nb_{2/3})O_3$ (PZN) and PZN-PT, the polar direction of PNRs is not aligned to the external field but redistributed to the $\langle 110 \rangle$ or $\langle 0\bar{1}0 \rangle$ directions, perpendicular to a macroscopic polar vector [69,70]. Anisotropy of PNRs was also found in the PMN and PMN-PT systems by neutron studies [71,72]. It, therefore, can be concluded that nanoscale polarization coexists with macroscopic ferroelectric polarization [73].

Another interesting aspect is the size of PNRs. From a simple Lorentzian function, the correlation length, ξ, could be analysed, which could indicate the scale of static PNRs. In PMN crystal, the length scale first starts appearing to be as small as approx. 15 Å near T_d, and then on cooling, it grows to nearly 60 Å at low temperatures [68]. This length increases to three times higher in PMN-10%PT and 30 times higher in PMN-20%PT, respectively [71]. Ti cations cause larger growth of PNRs, leading to the macroscopic domains.

The theory in which PNRs are embedded into the non-polar matrix had been the most popular model [4,5,56]. Contrasting results have been revealed by both simulation and experimental results. By molecular dynamics simulation, Takenake *et al.* revealed that there are nanosized multi-domain states with low-angle domain walls in pure PMN and PMN-PT [74]. Using integrated differential-phase-contrast STEM, the nanoscale domains with sizes from two to 12 nm are separated by low-angle domain walls in PMN-0.25PT [65].

PNRs have been known to play significant roles in the extraordinary properties of relaxor-ferroelectrics. Using cryogenic measurements and phase-field simulation, Fi *et al*. found that PNRs contribute in two ways to ultrahigh dielectric and piezoelectric responses in PMN-PT and PZN-PT. One is non-collinear, in which PNRs easily switch the polar vector aligned to the applied field at low temperature. The other is collinear, where at higher temperature, the polar vector of PNRs that is along the polar direction of the long-range matrix easily rotates to the direction of an applied field due to the energy minimum. This phenomenon also enables adjacent polarizations to rotate along the applied field in order to lower the interfacial energies. This contribution, for instance, shares 75 % of the room temperature dielectric permittivity in PZN-0.15PT [54,55]. Xu *et al*. suggested that phonon-PNR interaction plays an important role in the ultrahigh piezoelectric response. $[110]_C$-oriented PNRs induce a phase instability through transverse acoustic (TA) phonons in $[111]_C$-poled PZN-0.045PT, so such a structural instability could be a sign of the microscopic origin of the ultrahigh piezoelectric performance

[75]. Manley *et al*. reported that diffuse scattering in PNRs merges with lattice dynamics to generate a PNR-phonon hybridization. This hybrid motion plays a crucial role in achieving superior properties [76]. Such a merger is called Lorentzian phonon localization, where phonons are trapped in lattice dynamics, generating PNRs [77].

References

[1] B. Jaffe, W. R. Cook and H. Jaffe, “Piezoelectric Ceramics”, Academic Press Inc. (London) Ltd, 1971, London, pp 7-11, 15

[2] D. Berlincourt, “Piezoelectric Crystals and Ceramics,” in Ultrasonic Transducer Materials, edited by O.E. Mattiat, Plenum Press, New York and London, 1971, p 65,

[3] S. Zhang, and F. Li, High performance ferroelectric relaxor-$PbTiO_3$ single crystal: Status and perspective, *J. Appl. Phys* 111, 031301 (2012).

[4] L. E. Cross, Relaxor ferroelectrics, *Ferroelectrics* 76, 241 (1987).

[5] F. Li, S. Zhang, D. Damjanovic, L. Q. Chen, and T. R. Shrout, Local structural heterogeneity and electromechanical responses of ferroelectrics: Learning from relaxor ferroelectrics, *Adv. Func. Mater*. 28, 1801504 (2018).

[6] G. A. Smolenskii and A. I. Agranovskii, Dielectric polarization of a number of complex compounds, *Sov. Phys. Solid State*, 1, 1429 (1960).

[7] K. Uchino, S. Nomura, L. E. Cross, S. J. Jang, and R. E. Newnham, Electrostrictive effect in lead magnesium niobate single crystals, *J. Appl. Phys*, 51, 1142-1145 (1980).

[8] S. W. Choi, T. R. Shrout, S. J. Jang, and A. S. Bhalla, Morphotropic phase boundary in Pb $(Mg_{13}Nb_{23})$ O_3-$PbTiO_3$ system, *Mater. Lett*, 8, 253-255 (1989).

[9] S. L. Swartz and T. R. Shrout, Fabrication of perovskite lead magnesium niobate, *Mater. Res. Bull.*, 17, 1245 (1982).

[10] J. Kuwata, K. Uchino, and S. Nomura, Dielectric and piezoelectric properties of $0.91Pb(Zn_{1/3}Nb_{2/3})O_3$-$0.09PbTiO_3$ single crystals, *Jpn. J. Appl. Phys*. 21, 12981302 (1982).

[11] S. E. Park and T. R. Shrout, Ultrahigh strain and piezoelectric behavior in relaxor based ferroelectric single crystals, *J. Appl. Phys*., 82, 1804 (1997).

[12] S. E. Park and T. R. Shrout, Relaxor based ferroelectric single crystals for electro-mechanical actuators. *Mater*. *Res*. *Innov*., 1, 20-25 (1997).

[13] H. Luo, G. Xu, P. Wang, and Z. Yin, Growth and characterization of relaxor ferroelectric PMNT single crystals. *Ferroelectrics* 231, 97-102 (1999).

[14] S. Zhang, L. Lebrun, D. Y. Jeong, C. A. Randall, Q. Zhang, and T. R. Shrout, Growth and characterization of Fe-doped $Pb(Zn_{1/3}Nb_{2/3})O_3-PbTiO_3$ single crystals. *J. Appl. Phys.*, 93, 9257-9262 (2003).

[15] S. Zhang, C. A. Randal, and T. R. Shrout, Characterization of perovskite piezoelectric single crystals of $0.43BiScO_3–0.57PbTiO_3$ with high Curie temperature. *J. Appl. Phys.*, 95, 4291-4295 (2004).

[16] S. Zhang, S. Rhee, C. A. Randall, and T. R. Shrout, Dielectric and piezoelectric properties of high Curie temperature single crystals in the $Pb(Yb_{1/2}Nb_{1/2})O_3–xPbTiO_3$ solid solution series. *Jpn. J. Appl. Phys.*, 41, 722 (2002).

[17] S. Zhang, S. M. Lee, D. H. Kim, H. Lee, and T.R. Shrout, Characterization of high T_C $Pb(Mg_{1/3}Nb_{2/3})O_3$-$PbZrO_3$-$PbTiO_3$ single crystals fabricated by solid state crystal growth. *Appl. Phys. Lett.*, 90, 232911 (2007).

[18] J. Tian, P. Han, X. Huang, H. Pan, J. F. Carroll III, and D. A. Payne, Improved stability for piezoelectric crystals grown in the lead indium niobate–lead magnesium niobate–lead titanate system. *Appl. Phys. Lett.*, 91, 222903 (2007).

[19] Y. Hosono, and Y. Yamashita, Piezoelectric ceramics and single crystals for ultrasonic medical transducers. *J. Electroceramics.*, 17, 577-583 (2006).

[20] S. Zhang, J. Luo, W. Hackenberger, and T. R. Shrout, Characterization of $Pb(In_{1/2}Nb_{1/2})O_3–Pb(Mg_{1/3}Nb_{2/3})O_3–PbTiO_3$ ferroelectric crystal with enhanced phase transition temperatures. *J. Appl. Phys.*, 104, 064106 (2008).

[21] X. Liu, S. Zhang, J. Luo, T. R. Shrout, and W. Cao, Complete set of material constants of $Pb(In_{1/2}Nb_{1/2})O_3–Pb(Mg_{1/3}Nb_{2/3})O_3–PbTiO_3$ single crystal with morphotropic phase boundary composition. *J. Appl. Phys.*, 106, 074112 (2009).

[22] S. Zhang, F. Li, N. P. Sherlock, J. Luo, H. J. Lee, R. Xia, R. J. Meyer Jr, W. Hackenberger, and T. R. Shrout, Recent developments on high Curie temperature PIN–PMN–PT ferroelectric crystals. *J. Cryst. Growth*, 318, 846-850 (2011).

[23] S. Zhang, S. M. Lee, D. H. Kim, H. Y. Lee, and T. R. Shrout, Characterization of Mn-modified $Pb(Mg_{1/3}Nb_{2/3})O_3$-$PbZrO_3$-$PbTiO_3$ single crystals for high power broad bandwidth transducers. *Appl. Phys. Lett.*, 93, 122908 (2008).

[24] J. Luo, W. Hackenberger, S. Zhang, and T. R. Shrout, A high Q_m relaxor ferroelectric single crystal: Growth and characterization. In *Proceedings of 2010 IEEE International Ultrasonics Symposium*, pp. 68-71. IEEE, 2010.

[25] Y. H. Chen, K. Uchino, M. Shen, and D. Viehland, Substituent effects on the mechanical quality factor of $Pb(Mg_{1/3}Nb_{2/3})O_3$–$PbTiO_3$ and $Pb(Sc_{1/2}Nb_{1/2})O_3$–$PbTiO_3$ ceramics. *J. Appl. Phys.*, 90, 1455-1458 (2001).

[26] S. Zhang, S. Taylor, F. Li, J. Luo, and R. J. Meyer Jr, Piezoelectric property of relaxor-$PbTiO_3$ crystals under uniaxial transverse stress. *Appl. Phys. Lett.*, 102, 172902 (2013).

[27] A. J. Bell, Phenomenologically derived electric field-temperature phase diagrams and piezoelectric coefficients for single crystal barium titanate under fields along different axes. *J. Appl. Phys.* 89, 3907-3914 (2001).

[28] M. Davis, Phase transitions, anisotropy and domain engineering: the piezoelectric properties of relaxor-ferroelectric single crystals. Doctoral dissertation, The Ecole polytechnique federale de Lausanne, Lausanne, Swiss, 2006.

[29] S. Wada, “Domain wall engineering in piezoelectric crystals with engineered domain configuration,” in Handbook of Advanced Dielectric, Piezoelectric and Ferroelectric Materials – Synthesis, Characterization and Applications, edited by Z. G. Ye (Woodhead, Cambridge, England, 2008), pp. 266–303.

[30] Y. Guo, H. Luo, K. Chen, H. Xu, X. Zhang and Z. Yin, Effect of composition and poling field on the properties and ferroelectric phase-stability of $Pb(Mg_{1/3}Nb_{2/3})O_3$–$PbTiO_3$ crystals, *J. Appl. Phys*., 92, 6134 (2002).

[31] Z. Feng, X. Zhao, and H. Luo, Composition and orientation dependence of dielectric and piezoelectric properties in poled crystals, *J. Appl. Phys*., 100, 024104 (2006).

[32] F. Li, S. Zhang, Z. Xu, Xi. Wei, J. Luo, and T. R. Shrout, Composition and phase dependence of the intrinsic and extrinsic piezoelectric activity of domain engineered $(1-x)Pb(Mg_{1/3}Nb_{2/3})O_3-xPbTiO_3$ crystals, *J. Appl. Phys*. 108, 034106 (2010).

[33] J. Han and W. Cao, Electric field effects on the phase transitions in [001]-oriented $(1-x)Pb(Mg_{1/3}Nb_{2/3})O_3$-$xPbTiO_3$ single crystals with compositions near morphotropic phase boundary, *Phys. Rev. B*, 68, 134102 (2003).

[34] O. Noblanc, P. Gaucher, and G. Calvarin, Structural and dielectric studies of $Pb(Mg_{1/3}Nb_{2/3})O_3$–$PbTiO_3$ ferroelectric solid solutions around the morphotropic boundary, *J. Appl. Phys*. 79, 4291-4297 (1996).

[35] T. R. Shrout, Z. P. Chang, N. C. Kim, and S. Markgraf, Dielectric behaviour of single crystals near the (1-x) $Pb(Mg_{1/3}Nb_{2/3})$-(x)$PbTiO_3$ morphotropic phase boundary, *Ferroelectr. Lett. Sec,* 12, 63-69 (1990).

[36] M. L. Mulvihill, L. E. Cross, W. Cao and K. Uchino, Domain-related phase transitionlike behavior in lead zinc niobate relaxor ferroelectric single crystals, *J. Am. Ceram. Soc*., 80 1462 (1997).

[37] F. Li, Z. Xu and S. Zhang, The effect of polar nanoregions on electromechanical properties of relaxor-$PbTiO_3$ crystals: Extracting from electric-field-induced polarization and strain behaviors, *Appl. Phys. Lett*., 105, 122904 (2014).

[38] H. Fan, L. Kong, L. Zhang, and X. Yao, Phase transitions due to polar region structure in disordered ferroelectrics, *J. Mater. Sci*., 34, 6143–6149, (1999).

[39] L. Jin, F. Li and S. Zhang, Decoding the fingerprint of ferroelectric loops: comprehension of the material properties and structures, *J. Am. Ceram. Soc*., 97, 1-27 (2014).

[40] M. Davis, Dr. Damjanovic, and N. Setter, Electric-field-, temperature-, and stress-induced phase transitions in relaxor ferroelectric single crystals, *Phys. Rev. B.*, 73, 014115 (2006).

[41] Y. Guo, H. Luo, D. Ling, H. Xu, T. He and Z. Yin, The phase transition sequence and the location of the morphotropic phase boundary region in $(1-x)[Pb(Mg_{1/3}Nb_{2/3})O_3]$–$x$$PbTiO_3$ single crystal, *J. Phys.: Condens. Matter.*, 15, L77 (2003).

[42] Z. Li, Z. Xu, X. Yao, and Z.-Y. Cheng, Phase transition and phase stability in [110]-, [001]-, and [111]-oriented $0.68Pb(Mg_{1/3}Nb_{2/3})O_3$–$0.32PbTiO_3$ single crystal under electric field, *J. Appl. Phys.*, 104, 024112 (2008).

[43] E. V. Colla, N. K. Yushin, and D. Viehland, Dielectric properties of $(PMN)_{(1-x)}(PT)_x$ single crystals for various electrical and thermal histories, *J. Appl. Phys*, 83, 3298 (1998).

[44] X. Zhao, B. Fang, H. Cao, Y. Guo and H. Luo, Dielectric and piezoelectric performance of PMN-/PT single crystals with compositions around the MPB: influence of composition, poling field and crystal orientation, *Mater. Sci. Eng.*, B96, 254-262 (2002).

[45] F. Yan, P. Bao and Y. Wang, Phase transition in relaxor ferroelectrics studied by mechanical measurements, *Appl. Phys. Lett.*, 83, 4384 (2003).

[46] Q. Wan, C. Chen, and Y. P. Shen, Effects of stress and electric field on the electromechanical properties of $Pb(Mg_{1/3}Nb_{2/3})O_3$–$0.32PbTiO_3$ single crystals, *J. Appl. Phys*. 98, 024103 (2005).

[47] A. Amin, E. McLaughlin, H. Robinson, and L. Ewart, Mechanical and thermal transitions in morphotropic PZN-PT and PMN-PT single crystals and their implication for sound projectors, *IEEE Trans. Ultrason. Ferroelectr. Freq.Control.*, 54, 1090 (2007).

[48] K. G. Webber, R. Zuo and C. S. Lynch, Ceramic and single-crystal (1 – x)PMN–xPT constitutive behavior under combined stress and electric field loading, *Acta Mater.*, 56, 1219–1227 (2008).

[49] S. Young, M. Staruch, E. A. Patterson, A. N. Caruso, S. E. Lofland and P. Finkel, Thermally induced phase switching in mechanically biased single crystal relaxors, *Appl. Phys. Lett.*, 115, 252901 (2019).

[50] D. Viehland, L. Ewart, J. Powers, and J. F. Li, Stress dependence of the electromechanical properties of ⟨001⟩-oriented $Pb(Mg_{1/3}Nb_{2/3})O_3–PbTiO_3$ crystals: Performance advantages and limitations, *J. Appl. Phys*., 90, 2479 (2001).

[51] P. Finkel, H. Robinson, J. Stace, and A. Amin, Study of phase transitions in ternary lead indium niobate-lead magnesium niobate-lead titanate relaxor ferroelectric morphotropic single crystals, *Appl. Phys. Lett*., 97, 122903 (2010).

[52] S. Zhang, F. Li, X. Jiang, J. Kim, J. Luo, and X. Geng, Advantages and challenges of relaxor-$PbTiO_3$ ferroelectric crystals for electroacoustic transducers–A review. *Prog. Mater. Sci*., 68, 1-66 (2015).

[53] G. Burns, F. H. Dacol, Glassy polarization behavior in ferroelectric compounds $Pb(Mg_{1/3}Nb_{2/3})O_3$ and $Pb(Zn_{1/3}Nb_{2/3})O_3$, *Solid State Commun.*, 48, 853, (1983).

[54] F. Li, S. Zhang, T. Yang, Z. Xu, N. Zhang, G. Liu, J. Wang, J. Wang, Z. Cheng, Z.-G.Ye, J. Luo, T. R. Shrout and L.-Q. Chen, The origin of ultrahigh piezoelectricity in relaxor-ferroelectric solid solution crystals, *Nat. Commun*, 7, 13807 (2016).

[55] F. Li, S. Zhang, Z. Xu, and L.-Q. Chen, The contributions of polar nanoregions to the dielectric and piezoelectric responses in domain-engineered relaxor-$PbTiO_3$ Crystals, *Adv. Funct. Mater.* 27, 1700310, (2017).

[56] A. A. Bokov and Z.-G. Ye, Recent progress in relaxor ferroelectrics with perovskite structure, *J. Mater. Sci*. 41, 31–52, (2006).

[57] J. Chen, H. M. Chan, and M. P. Harme, Ordering structure and dielectric properties of undoped and La/Na-doped $Pb(Mg_{1/3}Nb_{2/3})0_3$, *J. Am. Ceram. Soc*, 72, 593-598 (1989).

[58] C. Boulesteix, F. Varnier, A. Llebaria and E.Husson, Numerical determination of the local ordering $Pb(Mg_{1/3}Nb_{2/3})0_3$ (PMN) from high resolution electron microscopy images, *J. Solid State Chem.* 108, 141 (1994).

[59] M. Yoshida, S. Mori, N. Yamamoto, Y. Uesu and J. M. Kiat, TEM observation of polar domains in relaxor ferroelectric $Pb(Mg_{1/3}Nb_{2/3})O_3$, *Ferroelectrics*, 217:1, 327-333 (1998).

[60] H. D. Rosenfeld and T. Egami, A model of short and intermediate range atomic structure in the relaxor ferroelectric $Pb(Mg_{1/3},Nb_{2/3})O_3$, *Ferroelectrics*, 158, 351 (1994).

[61] P. K. Davies and M. A. Akbas, Chemical order in PMN-related relaxors: Structure, stability, modification, and impact on properties, *J. Phys. Chem. Solids*, 61, 159 (2000).

[62] H. Z. Jin, J. Zhu, S. Miao, X. W. Zhang, and Z. Y. Cheng, Ordered domains and polar clusters in lead magnesium niobate $Pb(Mg_{1/3}Nb_{2/3})O_3$, *J. Appl. Phys*., 89, 5048-5052 (2001).

[63] M. J. Cabral, S. Zhang, E. C. Dickey, and J. M. LeBeau, Gradient chemical order in the relaxor $Pb(Mg_{1/3}Nb_{2/3})O_3$, *Appl. Phys. Lett*., 112, 082901 (2018).

[64] M. J. Krogstad, P. M. Gehring, S. Rosenkranz, R. Osborn, F. Ye, Y. Liu, J. P. C. Ruff, W. Chen, J. M. Wozniak, H. Luo, O. Chmaissem, Z.-G. Ye, The relation of local order to material properties in relaxor ferroelectrics, *Nat. Mater*., 17, 718–724 (2018).

[65] A. Kumar, J. N. Baker, P. C. Bowes, M. J. Cabral, S. Zhang, E. C. Dickey, D. L. Irving, J. M. LeBeau, Atomic-resolution electron microscopy of nanoscale local structure in lead-based relaxor ferroelectrics, *Nat. Mater.*, 20, 62–67 (2021).

[66] S. Vakhrushev, A. Nabereznov, S. K. Sinha, Y. P. Feng and T. Egami, Synchrotron X-ray scattering study of lead magnoniobate relaxor ferroelectric crystals, *J. Phys. Chem. Solids*. 57, 1517 (1996).

[67] C. Stock, L. Van Eijck, P. Fouquet, M. Maccarini, P. M. Gehring, G. Xu, H. Luo, X. Zhao, J.-F. Li, D. Viehland, Interplay between static and dynamic polar correlations in relaxor $Pb(Mg_{1/3}Nb_{2/3})O_3$, *Phys. Rev. B*. 81, 144127 (2010).

[68] G. Xu, G. Shirane, J. R. D. Copley and P. M. Gehring, Neutron elastic diffuse scattering study of $Pb(Mg_{1/3}Nb_{2/3})O_3$ *Phys. Rev. B* 69, 064112 (2004).

[69] G. Xu, Z. Zhong, Y. Bing, Z.-G. Ye and G. Shirane, Electric-field-induced redistribution of polar nano-regions in a relaxor ferroelectric, *Nat. Mater,* 5, 134-140 (2006).

[70] G. Xu, Z. Zhog, H Hiraka, and G. Shirane, Three-dimensional mapping of diffuse scattering in $Pb(Zn_{1/3}Nb_{2/3})O_3$-$x$$PbTiO_3$, *Phys. Rev. B*, 70, 174109 (2004).

[71] M. Matsuura, K. Hirota, P. M. Gehring, Z.-G. Ye, W. Chen, and G. Shirane, Composition dependence of the diffuse scattering in the relaxor ferroelectric compound $(1-x)Pb(Mg_{1/3}Nb_{2/3})O_3-xPbTiO_3$ ($0\leq x\leq 0.40$), *Phys. Rev. B*, 74, 144107 (2006).

[72] C. Stock, P. M. Gehring, H. Hiraka, I. Swainson, G. Xu, Z.-G. Ye, H. Luo, J.-F. Li, and D. Viehland, Evidence for anisotropic polar nanoregions in relaxor $Pb(Mg_{1/3}Nb_{2/3})O_3$: A neutron study of the elastic constants and anomalous TA phonon damping in PMN, *Phys. Rev. B* 86, 104108 (2012).

[73] G. Xu, P. M. Gehring, and G. Shirane, Coexistence and competition of local- and long-range polar orders in a ferroelectric relaxor, *Phys. Rev. B*. 74, 104110 (2006).

[74] H. Takenaka, I. Grinberg, S. Liu and A. M. Rappe, Slush-like polar structures in single-crystal relaxors, *Nature*, 546, 391 (2017).

[75] G. Y. Xu, J. S. Wen, C. Stock, and P. M. Gehring, Phase instability induced by polar nanoregions in a relaxor ferroelectric system. *Nat. Mater*. 7, 562–566 (2008).

[76] M. E. Manley, J. W. Lynn, D. L. Abernathy, E. D. Specht, O. Delaire, A. R. Bishop, R. Sahul, J. D. Budai, Phonon localization drives polar nanoregions in a relaxor ferroelectric, *Nat. Commun*, 5, 3683 (2014).

[77] M. E. Manley, D. L. Abernathy, R. Sahu, D. E. Parshall, J. W. Lynn, A. D. Christianson, P. J. Stonaha, E. D. Specht, and J. D. Budai, Giant electromechanical coupling of relaxor ferroelectrics controlled by polar nanoregion vibrations, *Sci. Adv*. 2, e1501814 (2016).

Chapter 3. Recent development of relaxor-PT ferroelectric crystals

This section reviews the recent development of the relaxor-PT single crystals. This work is published as a review article in *Crystals **2022**, 12, 56* by *Baasandorj. L and Chen. Z,* [1].

3.1 Property improvements

Achievement of the MPB composition in solid solution Pb-based ferroelectric materials has been a traditional strategy in the last several decades to reach the highest dielectric and piezoelectric responses [2-5]. Nonetheless, this strategy was shown to reach a plateau where no further enhancement could be expected. In addition to the MPB, the local structure heterogeneity inherently associated with the randomly located B-site cations of the relaxor-PT ferroelectrics also contributes greatly to the properties [6,7].

3.1.1 Poling strategy

Applying an external field enables us to control the ferroelectric/ferroelastic domains and to use the related properties for practical demands. Producing desirable domain configurations is thus of both scientific and technological interest [8]. Poling techniques for relaxor-PT crystals, including traditional direct current (electric-field) poling (DCP) [2,3,9] and alternating current (electric-field) poling (ACP), have recently attracting a lot of attention [10,11].

3.1.1.1 DCP

DCP is a traditional technique used to align the polarization of ferroelectric materials, thus exhibiting piezoelectricity. In relaxor-PT single crystals, the poling along nonpolar direction will lead to engineered domain configurations, accounting for the high piezoelectricity observed in single crystals when compared to their ceramic counterparts. The effects of field strength and the influence of temperature are always of interest in maximizing material properties [12].

Threshold DC field and over-poling effect: To reveal the maximum piezoelectric property in a ferroelectric material, a low direct current (DC) field is not sufficient for full polarization. However, a field that is too high could over-polarize the material and degrade its properties. It is thus crucial to find an appropriate field range for an efficient poling procedure [13]. The DC electric field effect on the properties of relaxor-PT crystals has been intensively studied [14-31]. In general, the longitudinal piezoelectric coefficient in PMN-PT single crystal is achieved under a moderate DC-field at room temperature. The highest order of d_{33} is found in the MPB composition, where polar rotation exists from rhombohedral to monoclinic (M_A) phase [23,24,32-34]. For the 0.70PMN-0.30PT composition, M_A phase is induced starting from a ~2.0 kV/cm field (with its coercive field 2.2-2.5 kV/cm). The maximum value of d_{33} is reached at ~4.0 – 6.0 kV/cm [22,23,26]. In order to achieve a sufficiently poled sample, an electric field at 2-3 times the coercive field is applied in practice. After continuously increasing the electric field, the over-poling effect takes place, and the piezoelectric coefficient decreases, owing to the stability of the new electric field-induced phase [22,24], vulnerability to sample cracking [35], and the tetragonal phase transition [14,36,37]. It is important to note that the magnitudes of electric fields are varied in different compositions of crystals because of the coercive field difference.

In order to avoid degrading the piezoelectric property during the poling process, it is always important to find the threshold of the over-poling field for practical applications of relaxor-PT single crystals.

High-temperature DCP: High-temperature poling enhances the piezoelectric response in relaxor-PT single crystals. **Table 3.1** gives a comparison of the values of the longitudinal piezoelectric coefficient and the dielectric constant for poling at different temperatures. **Figure 3.1** exhibits the maximum piezoelectric response and corresponding poling field depending on temperature. It is shown that the dielectric constant $\varepsilon^T_{33}/\varepsilon_0$ and piezoelectric d_{33} are increased by high-temperature poling when compared to the values for room-temperature poling. The domain size in the high-temperature poled samples is reduced as well [28,29]. The electric field strength is also lowered at elevated temperatures shown in **figure 3.1**. It was explained that, when a DC field is applied to a single crystal at a temperature around T_C, microdomains are aligned along the applied field. When the temperature is reduced under the applied field, small ferroelectric domains with a high density of domain walls are created. The increase of d_{33} is thus attributed to the higher domain wall motion as an extrinsic contribution

[13,36,38,39]. Further, at elevated temperatures, the high mobility of domain walls requires a lower electric field [13].

Besides property improvement, high-temperature poling offers other benefits. Temperature stability in ferroelectric crystals is desirable for electromechanical applications. A single crystal poled at elevated temperature showed enhanced piezoelectric stability [36,39]. The d_{33} and k_{33} in [111]-poled orthorhombic PMN-PT crystal were stable up to 75 °C, which was attributed to the fine domains achieved in high temperature poling [39]. The high-temperature poling technique also made it possible to form crack-free single domain configuration. An electric DC-field along [001] was applied to a tetragonal PIN-PMN-PT crystal at a temperature above T_C, and then on cooling, only the [001]-oriented domain was formed while the formation of non-180° domains was avoided. The reduced non-180° ferroelectric domains decreased the strain variation, resulting in achieving a crack-free single domain [35]. The resulting single-domain crystal showed that there was no cost to the piezoelectricity but a high mechanical quality factor [35].

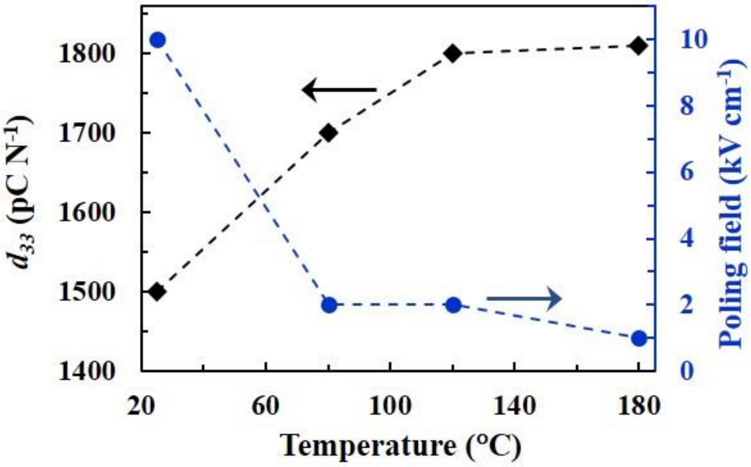

Figure 3.1 Temperature dependent piezoelectric response and poling field [13].

.

Table 3.1 Property comparison of DCP at different temperatures.

Single crystal	Domain configuration	DC field (kV cm^{-1})	Poling temp. (°C)	Domain size (μm)	$\varepsilon_{33}/\varepsilon_0$	Loss (%)	d_{33} (pC N^{-1})
PIN–PMN–PT[a)]	3T	4.0	210	0.5	13800	0.7	1630
PIN–PMN–PT	3T	4.0	150	50.0	3000	0.4	450
0.68PMN–0.32PT[b)]	3O	2.0	150	~2.0	6400	0.3	900
0.68PMN–0.32PT	3O	4.0	25	~20.0	4400	0.4	450

a) Reference [38]
b) Reference [39]

3.1.1.2 ACP

In previous section, DCP technique was discussed. This section will discuss ACP. These two sections are clearly exhibited the differences and features between conventional and new poling techniques. This section further enables to recognize how and what new property improvements have been brought by ACP technique. The ACP technique has been recently proved to be a very efficient way of improving performance in relaxor-PT crystals, including electromechanical and piezoelectric properties.

Increase of piezoelectricity: ACP was recently proved to be a very efficient way of engineering domains in relaxor-PT crystals. It provides greater improvement of the piezoelectric and electromechanical properties than DCP [10,11]. **Table 3.2** presents a property comparison of AC- and DC-poled samples with the poling conditions. The dielectric constant and longitudinal piezoelectric coefficients of ACP in the three generations of single crystals are enhanced compared to those of DCP. It was suggested that this enhancement of the properties is attributable to ACP-induced intermediate phases and increased domain wall density, while another argument about the ACP induced enlargement of domains was proposed later. The main difference between ACP and DCP is associated with the domain structure. ACP creates well-ordered domains. In particular, it is claimed that 109° and 71° domain walls in [001]-poled rhombohedral single crystals evolve to more regular patterns with narrower widths, giving rise to a higher domain wall density [10,40-42]. The resulting high domain wall density contributes to the enhanced properties as an extrinsic contribution. Luo *et al.* explained the ACP effect on the formation of a uniform domain pattern. Under DCP, not all domains are oriented along the electric field, while some domains remain depolarized due to the stable DC field in the same direction [41].

Furthermore, the intrinsic contribution accounts for the improvement of piezoelectricity. ACP initiates intermediate monoclinic phases [40,41,43-45] and lattice distortion [45,46]. There is easy polarization rotation via monoclinic phases, resulting in a significant increase of the piezoelectric property [14,47,48].

In contrast to the decreased domain size and increased domain wall motion, the enlargement of domains is suggested to be a contribution to the enhanced piezoelectric response in the AC poled ferroelectric crystals. The ACP effect was explained by the repeated reversal of the electric field using a phase-field simulation, which leads to the flipping of adjacent 71° domain walls to eventually merge with each other in [001]-poled rhombohedral PMN-PT crystal. The enlargement of 71° domain widths reduces the polarization variation from the [111] polarization direction and flattens the free-energy profile. As a result, the piezoelectricity is enhanced [11]. The widened 71° domains were experimentally observed by polarized light microscopy and high-resolution synchrotron X-ray diffraction (XRD) techniques [11,49]. The domain evolution on reduction of 71° domain wall density is consistent with other reports [42,50-52].

It was also reported that ACP-induced PNRs further support the enhancement of piezoelectricity [43,53,54]. In the single-domain tetragonal 0.25PIN-0.43PMN-0.32PT crystal, the dielectric constant after ACP is much larger than that after DCP, and the temperature-dependent dielectric constant also shows a relaxor-like frequency dispersion. This phenomenon corresponds to the existence of PNRs [44].

It should also be noted that the improvement depends on the poling conditions, including field strength, frequency, cycle, and temperature. Generally, better piezoelectric improvement is developed at lower frequencies of the alternating current [42,50] and a higher poling temperature [55-58]. The high-temperature poling initiates multiple intermediate phases [58] and also increases the domain wall density [53]. Both intrinsic and extrinsic contributions are thus caused by high-temperature poling. At lower frequency, there is a lower energy barrier against polarization switching and lower friction or loss attributable to the property enhancement [59,60].

The ACP technique has been proved to be a very efficient method to increase the dielectric and piezoelectric properties of relaxor-PT single crystals.

Improvement of transparency: The ACP technique offers another great advantage for domain engineering, in that relaxor-PT crystals could retain high multifunctional performance. Pure and modified PMN-PT systems were found to have superior properties compared with the conventional materials in optical and electro-optical applications, making them good candidates for practical needs [61,62]. AC-poled 0.72PMN-0.28PT crystal along the [001] direction was revealed with a high electro-optical coefficient (γ_{33}) of 220 pm V^{-1} and almost complete light transmittance at wavelengths higher than 400 nm. The birefringence and longitudinal piezoelectric coefficient of this sample were also improved to nearly 10 times higher and 30 % greater than those of its DC-poled counterpart, respectively [11]. The improvement of the properties is associated with ACP-induced domain engineering. In section 3.1.2.2, the mechanisms of domain change and piezoelectric enhancement are explained. The light transmittance is thus enhanced in the sample with enlarged 71° domain walls size [11,49]. ACP's effect on domain size is still critical. Contradicting results would be derived from results of a variety of techniques [11,40,46,50,51], different orientation [40,45,51] or surface vulnerability [46]. However, enlargement of domain size might be more reasonable because this could explain various property improvements (piezoelectric and optical properties) [11]. Also, decrease of 71 ° domain wall density was supported by different reports [42,46,50,51].

Table 3.2 Dielectric and piezoelectric property comparisons of ACP and DCP relaxor-PT single crystals at under different poling conditions.

						Poling condition			
Single crystal (poling)	$\varepsilon^T_{33}/\varepsilon_0$	**Differ. from DCP**	**tanδ (%)**	d_{33} **(pC N^{-1})**	**Differ. from DCP**	**Field (kV cm^{-1})**	**Freq. (Hz)**	**Cycle**	**Temp. (°C)**
0.75PMN-0.25PT (DCP) [10]	5321	/	/	1220	/	6.0-18.0	/	/	RT
0.75PMN-0.25PT(ACP)	6397	20 %	/	1730	40 %	12.0-18.0	20-40	20	RT
0.71PMN-0.29PT (DCP) [43]	7740	/	0.60	2030	/	5.0	/	/	50
0.71PMN-0.29PT (ACP)	8840	12 %	0.98	2850	28 %	12.0 (V_{p-p})	20	40	50
0.70PMN-0.30PT (DCP) [43]	8490	/	0.41	2710	/	5.0	/	/	50
0.70PMN-0.30PT (ACP)	8800	4 %	0.45	3050	12 %	12.0 (V_{p-p})	20	40	50
0.70PMN-0.30PT (DCP) [40]	6160	/	/	1650	/	10.0	/	/	RT

0.70PMN-0.30PT (ACP)	8500	38%	/	2000	21%	10.0 (V_{p-p})	1.0	7	RT
0.70PMN-0.30PT (DCP) [41]	5110	/	0.39	1760	/	8.0	/	/	50
0.70PMN-0.30PT (ACP)	8330	35 %	0.33	2750	56 %	4.0 (rms)	0.1	20	100 to 70
0.24PIN-0.46PMN-0.30PT (DCP) [56]	5440	/	/	1810	/	4.0	/	/	50
0.24PIN-0.46PMN-0.30PT (ACP)	7000	29 %	0.59	2340	29 %	4.0 (rms)	10	12	90
Mn: PIN-PMN-27PT (DCP) [42]	3700	/	0.30	1350	/	5.0-15.0	/	/	RT
Mn: PIN-PMN-27PT (ACP)	5300	43 %	0.30	1750	29 %	20.0 (V_{p-p})	0.1	20	RT

3.1.2 Doping strategy

Piezoelectric materials are modified for practical demands. Doping exerts two effects on Pb-based piezoelectric materials: ‘’hardening” and “softening”. In the hardening process, acceptor-dopants facilitate defect dipoles that generate an internal field (E_i), so that they clamp the domain wall motion. Consequently, the Q_m increases as the dielectric and mechanical losses are reduced. In contrast, in the softening effect, donor-dopants increase the domain wall mobility. The donor-doping leads to opposite effects to those of acceptor-dopants, including high dielectric and piezoelectric constants, a large electromechanical coupling factor, and high dielectric loss, but low Q_m [2,12,63]. The following section will discuss the donor and acceptor dopants in relaxor-PT single crystals and their effects on properties.

3.1.2.1. Hard piezoelectric single crystals

The “hard” PZT ceramics are the-state-of-the-art materials for high power transducer and resonance actuator technologies. Ultrahigh piezoelectric and electromechanical properties in relaxor-PT single crystals provide piezoelectric transducers with broader bandwidths and better sensitivity compared to conventional piezoceramics [2,12,64]. However, the low coercive field, high mechanical loss, and low rhombohedral to tetragonal transition temperature ($T_{r\text{-}t}$) and T_C of the first generation relaxor-PT single crystals restrict their use in transducer applications [3]. Their low mechanical quality factor causes mechanical heat dissipation during resonance based transducer operations, which leads to device failure [4,65,66]. Furthermore, the coercive field of the first generation is low, so an external dc bias is used to prevent depoling, leading to extra cost [3,12]. It is therefore necessary for materials to have a high mechanical quality factor, a great electromechanical coupling factor, low losses, and a high coercive field in high-power and actuator applications. On the other hand, high values of Q_m, the electromechanical coupling factor k, and the piezoelectric charge constant d are the material's figure of merit ($k^2 \cdot Q_m$ or $d \cdot Q_m$) for applications [12].

The acceptor-doped ternary PIN-PMN-PT material is a promising candidate for high power applications. To meet the requirement of a high $k^2 \cdot Q_m$ or $d \cdot Q_m$, the relaxor-PT single crystals are modified by Mn dopant [67,69-71], in an analogous way to "hard" PZT ceramics. The $Mn^{3+,2+}$ cation substitutes for the Ti^{4+} cation, since the ionic sizes of both are close. Oxygen vacancy defects consequently occur in order to compensate for the charge imbalance, and it creates defect dipoles. Those defect dipoles realign in the energetically preferred direction along with the spontaneous polarization, leading to an internal field that pins domain wall motion and restricts polarization rotation. As a result, the "hardening" effect in a single crystal (the third generation relaxor-PT single crystal) is achieved [72-74]. **Table 3.3** shows the properties of different Mn-doped Pb-based single crystals compared to those of their undoped counterparts. Among them, the Mn-doped ternary PIN-PMN-PT has drawn intensive attention. Its mechanical quality factor is 4-5 times higher than its undoped counterpart, owing to the "hardening effect" by its acceptor-dopant [68,75]. Its piezoelectric and dielectric properties values are comparable to those of its undoped counterpart. Hence, with its giant Q_m and comparable d and k values, the greater figures of merit $d \cdot Q_m$ and $k^2 \cdot Q_m$ could be achieved with Mn-doped ternary PT-relaxors. Furthermore, Q_m, being on the order of > 1000 in these single crystals, is comparable to those of "hard" PZTs. Higher k and d on the order of > 0.90 and > 1000, respectively, are also found. The figure of merit value, therefore, is far superior to that of the conventional PZT ceramics [3,64,67,68,72]. After modifying the relaxor-PT single crystal, it was also confirmed to be stable in external fields. The coercive field is 2 to 3 times higher than that of the first generation of single crystals [3,72,73,76] and slightly greater than that of its second generation counterparts with the same domain structure due to the acceptor-induced internal field [67,72,75,77]. The existence of internal bias in the third-generation crystals provide higher allowable ac drive fields and could avoid the depolarization [78] due to stabilized domain motion. In Table 3.3, it is also shown that single-domain crystals demonstrate a much higher quality factor compared to those of multi-domain crystals due to the fact that there is the least polarization rotation involved [64,73,76,79,80]. All of these property improvements are ascribed to the defect-dipole-induced internal field, which clamps domain wall motion and constrains the polarization rotation.

Mn-doped ternary PIN-PMN-PT and PMN-PZT single crystals are hence suitable materials for use in high power transducer applications due to high Q_m and E_C values, low losses, and a comparable piezoelectric response and electromechanical coupling factor.

3.1.2.2 Soft piezoelectric single crystals

For ultrasound transducer technologies, the high sensitivity of a device requires materials with a large electromechanical coupling factor, great piezoelectric coefficient, and high elastic compliance [3,81]. In order to improve the electromechanical coupling factor and piezoelectric response, donor additives are introduced into conventional PZT ceramics. The resulting phenomenon is a “softening” effect opposite to that of “hardening”. In donor-doped piezoelectric perovskite materials, an A-site vacancy is induced to neutralize charge imbalance. A pair of La^{3+} cations, for instance, create one Pb^{2+}-vacancy. The Pb-vacancy enhances the domain wall mobility, leading to a low coercive field, large dielectric constant and piezoelectric coefficient, a high electromechanical coupling factor, and high elastic compliance, but a reduced mechanical quality factor [1]. The donor-dopant La^{3+} in PZT has been intensively studied because it increases the dielectric constant due to relaxor behavior and is suitable for electro-optical applications [82-86]. Sm^{3+} has recently drawn attention due to its contribution to a giant electromechanical coupling factor and drastic increase of the piezoelectric coefficient in relaxor-PT systems [87-95]. A certain addition of Sm dopant is confirmed to lead to the highest values of d_{33}, being on the order of 1,500 pC N^{-1}, and $\varepsilon_{33}^{T}/\varepsilon_0$ being on the order of 13,000 in PMN-PT ceramic, and d_{33} being on the order of 4100 pC N^{-1} and $\varepsilon_{33}^{T}/\varepsilon_0$ of ~12,000 in PMN-PT single crystal, respectively [91,96]. Alongside the “softening” effect, A-site substituted Sm^{3+} doping enhances the local heterogeneity that minimizes the local free energy via competition between the bulk and interfacial energies. The lower free energy facilitates a large dielectric constant and a large piezoelectric coefficient

[7,91]. It is also important to note that the ionic size of samarium doping is the most suitable formation among other rare-earths ions to enhance the local heterogeneity, so this dopant results in the largest property values [96,97]. Donor dopants induce increased dielectric constant but a decreased Curie temperature [88,91,96]. It was explained that the random fields induced by donor dopants and the A-site vacancies affect the Curie temperature [96,98].

Donor-doped relaxor-ferroelectric materials demonstrate outstanding dielectric and piezoelectric performances, owing to the local structural heterogeneity in addition to "softening" effect, where the local structural heterogeneity plays the dominant role. The improved properties are suitable to use for enhancing actuator and medical imaging devices.

Table 3.3 Property comparisons of pure PMN-PT, pure and Mn-doped PIN-PMN-PT, pure and Mn-doped 0.88PZN-0.12PT, pure and Mn-doped 0.4PMN–0.25PZ–0.35PT, and Mn-doped 0.68PIN-0.32PT single crystals.

Material (domain state)	**Orientation**	**T_C (°C)**	**E_C (kV/cm)**	**$\varepsilon^T_{33}/\varepsilon_0$**	**tanδ (%)**	**Q_{33}**	**k_{33}**	**d_{33} (pC/N)**	**Growth method**	**Ref.**
0.70PMN–0.33PT	$[001]_C$	155	2.8	8200	/	100	0.94	2820	MB[b]	[3]
PIN–PMN–PT (MPB)[a]	$[001]_C$	197	5.5	7244	/	120	0.95	2742	MB	[3]
PIN-PMN-PT:Mn (2R)[a]	$[011]_C$	197	5.1	3523	0.6	1000	0.90	1053	MB	[72]
0.27PIN-0.46PMN-0.27PT:Mn (1R)	$[111]_C$	194	9.1	1299	/	1200	0.346	95	MB	[73]
0.26PIN-0.42PMN-0.32PT:Mn (1O)	$[011]_C$	208	5.6	1240	0.1	1230	0.70	267	MB	[76]
0.26PIN-0.42PMN-0.32PT:Mn (4O)	$[001]_C$	208	4.9	4280	0.4	300	0.91	1370	MB	[76]
0.88PZN-0.12PT:Mn	$[110]_C$	180	8.6	5300	0.4	750	0.60	500–600	CFG[c]	[70]
0.88PZN-0.12PT	$[110]_C$	185	12.3	5500	/	150	0.615	530	CFG	[70]
0.4PMN–0.25PZ–0.35PT:Mn	$[001]_C$	203	6.3	3410	0.2	1050	0.92	1140	SSCG[d]	[67]
0.4PMN–0.25PZ–0.35PT	$[001]_C$	211	4.5	4850	0.5	100	0.93	1530	SSCG	[67]
0.68PIN-0.32PT:Mn	$[001]_C$	231	9.7	1284	1.0	/	0.80	730	CFG	[71]

[a] The exact composition of the single crystals are not given.

[b] The Modified Bridgman method.

[c] Conventional flux growth method.

[d] Solid state conversion growth method.

3.2 Anisotropic features

3.2.1 Anisotropic factor

Different formations of domain configuration in relaxor-PT single crystals lead to highly anisotropic piezoelectric tensors. The degree of piezoelectric anisotropy is defined by the “anisotropic factor” as following ratio [12,99]:

$$\left(\frac{d_{15}}{d_{33}}\right) = 2\frac{Q_{13}}{Q_{33}}\left(\frac{\chi_{11}}{\chi_{33}}\right) \qquad (3.1)$$

Where, d_{33} and d_{15} are the longitudinal and shear piezoelectric coefficients, Q_{33} and Q_{13} are the longitudinal and shear electrostrictive coefficients, and χ_{33} and χ_{11} are the longitudinal and transverse dielectric susceptibility, respectively.

Table 3.4 summarizes the anisotropy of the principal properties in the second generation relaxor-PT crystals. **Figure 3.2** compared the anisotropic factors of different ferroelectric single crystals. Based on the piezoelectric values from **Table 3.4** and **figure 3.2**, the anisotropic factors are high in relaxor-PT single crystals, indicating that relaxor-PT crystals are highly anisotropic.

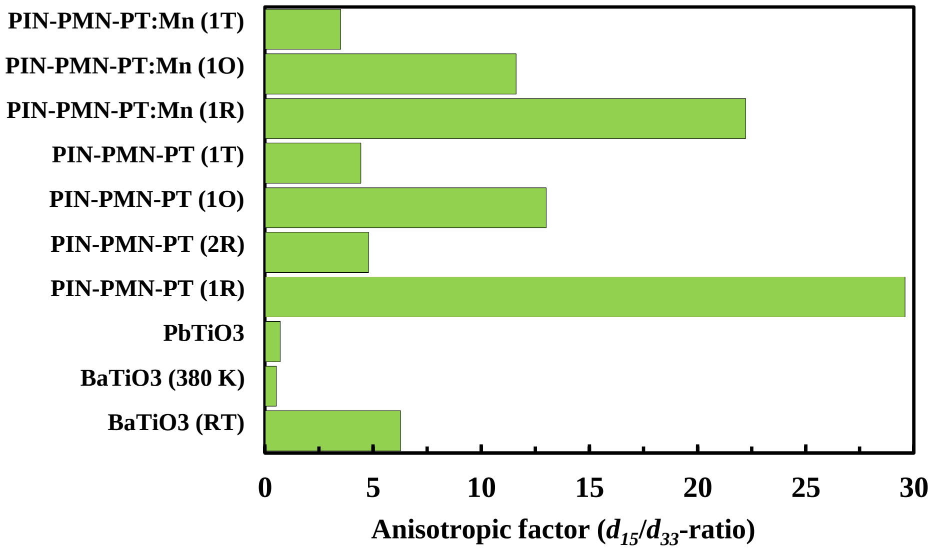

Figure 3.2 Anisotropic factors of various ferroelectric single crystals. Data from references [73,76,79,99,102,103,105,116,117].

Table 3.4 Anisotropic properties of the second generation relaxor-PT ferroelectric crystals.

Composition	**Domain configur.**	$\varepsilon_{33}^{T}/\varepsilon_0$	$\varepsilon_{11}^{T}/\varepsilon_0$	$\varepsilon_{22}^{T}/\varepsilon_0$	d_{15} **(pC·N^{-1})**	d_{31} **(pC·N^{-1})**	d_{32} **(pC·N^{-1})**	d_{33} **(pC·N^{-1})**	k_{31}	k_{33}	k_{15}	**Ref.**
PIN–PMN–28PT	2R	2920	5000	1030	2203	460	-1156	782	0.67	0.87	0.91	[77]
PIN–PMN–28PT	1R	702	6286	/	2190	-34	/	74	0.13	0.36	0.92	[105]
PIN–PMN–33PT	4O	7244	10081	/	232	-1337	/	2742	0.65	0.95	0.20	[114]
PIN–PMN–33PT	1O	1500	8070	30000	4550	153	-346	350	0.44	0.74	0.96	[103]
PIN–PMN–(39-41)PT	1T	1090	15000	/	2350	-200	/	530	0.50	0.84	0.85	[102]

3.2.2 Orientation dependence

It was shown that the shear piezoelectric coefficient is the highest in the single domain configuration [77,100-106]. From calculations of the orientation dependence, the maximum dielectric constant was observed in the direction perpendicular to the poling electric field, i.e., transverse dielectric constant, near the ferroelectric-to-ferroelectric phase transition in single domain state [101,105]. In single domain tetragonal symmetry, when an electric field is applied along an arbitrary direction, the longitudinal piezoelectric coefficient is expressed as following [99]:

$$d_{33}^{*} = \cos\theta \cdot \sin^2\theta \cdot d_{31} + \cos\theta \cdot \sin^2\theta \cdot d_{15} + \cos^3\theta \cdot d_{33} \tag{3.2}$$

Here "*" refers to away from polar axis. D. Damijanovic *et al*, analysed that the longitudinal piezoelectric coefficient, d_{33}* of single domain BaTiO$_3$ crystal is 194 pC/N at θ = 49.6° from polar axis in room temperature. However, this coefficient at θ = zero is 92 pC/N [107]. For single domain 3*m* crystal, the longitudinal piezoelectric coefficient, d_{33}* at any arbitrary direction is expressed as following [99]:

$$\begin{gathered} d_{33}^{*} = \cos\theta \cdot \sin^2\theta \cdot \sin^2\phi\,(d_{15} + d_{31}) + \cos^3\theta \cdot d_{33} + \sin^3\theta \\ \cdot \cos\phi \cdot (3\sin^2\phi - \cos^2\phi)d_{22} \end{gathered} \tag{3.3}$$

Here, analysis for piezoelectric coefficients in an arbitrary, non-polar direction of both *mm*2 and 3*m* crystals uses two Euler angles θ and ϕ. X. Liu *et al*, calculated the maximum values of d_{33}* and k_{33}* are in 64.1° and 79.2°, respectively, away from polar axis in single domain 3*m* PIN-PMN-PT crystal.

Their calculated values are; d_{33}* = 1122 pC/N and k_{33}* = 89% [105], and are nearly equal to their experimental values; d_{33}* = 1130 pC/N and k_{33}* = 89%, respectively. Damjanovic *et al*, also estimated, for single domain rhombohedral PMN-33PT crystal, the maximum value of d_{33}* = 2410 pC/N when angle θ is 62.9° and angle ϕ is 0° away from polar axis [108]. They found this piezoelectric coefficient is quite comparable to the measured value of multidomain in the same single crystal.

d_{33}* for orthorhombic *mm*2 symmetry at an arbitrary direction is expressed as:

$$d_{33}^{*} = \cos\theta \cdot \sin^{2}\theta \cdot \sin^{2}\phi\,(d_{15} + d_{31}) + \cos^{3}\theta \cdot d_{33} + \cos\theta \cdot \sin^{2}\theta \cdot \cos^{2}\phi\,(d_{24} + d_{32}) \qquad (3.4)$$

The maximum d_{33}* of single domain orthorhombic $Pb(Zn_{1/3}Nb_{2/3})O_3$-$PbTiO_3$ (PZN-PT) crystal was estimated as 1262 pC/N and this value occurs at θ = 53.2° and ϕ = 0° from polar axis [99].

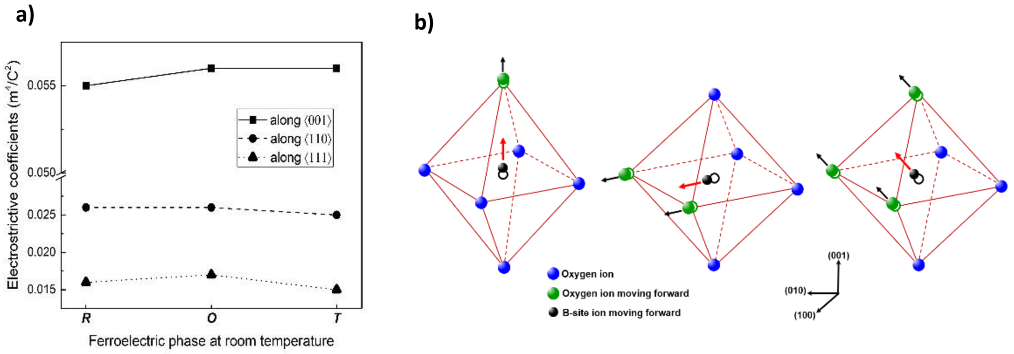

Figure 3.3 a) Calculated longitudinal electrostrictive coefficients along ⟨111⟩, ⟨110⟩, and ⟨100⟩ directions for rhombohedral, orthorhombic and tetragonal phases [119]. b) Oxygen ion displacement in octahedral structure with three different polarization direction.

The high value of the shear piezoelectric coefficient is related to the change in the transverse dielectric constant that arises from polarization rotation. Owing to free-energy profile flattening, polarization rotation simply occurs in the vicinity of a ferroelectric-to-ferroelectric phase transition [109]. For relaxor-PT single crystals, there is a high possibility of different phase transitions induced by composition, electric field, or temperature that lead to easy rotation of the polar vector [14,99]. The longitudinal piezoelectric coefficient has a low value, however, in the single domain configuration. This response is attributed to the polarization extension. The polarization extends towards an electric field direction when the electric field is applied along the polar direction. Therefore, the longitudinal piezoelectric property is ascribed to change in the longitudinal dielectric constant [66,99].

A high longitudinal piezoelectric coefficient exists in multi-domain configurations. From the calculation of the orientation dependence, maximum values of d_{33} are found at a certain angle away from the spontaneous polarization direction, indicating a contribution from the polarization rotation [101,102,110-114]. The longitudinal piezoelectric response in multi-domain single crystal also benefits from the shear piezoelectric phenomenon. The greatest values of d_{33} were revealed in 4O and 4R domain-engineered single crystals [9,20,101,102,108,111,114-118]. Furthermore, another anisotropic source contributes to the high piezoelectric response. As seen in expression (3.1), the anisotropy of piezoelectricity is also dependent on the anisotropy of electrostrictive coefficients. From calculations of the orientation dependence, the maximum electrostrictive coefficient was found in the ⟨100⟩ direction where similar values are observed among the *R*, *O,* and *T* phases. The minimum value was calculated in the ⟨111⟩ direction, and similar values were also observed in the three phases in **figure 3.3a**. The electrostrictive coefficient is related to the oxygen octahedra. For ⟨001⟩ direction phases, one oxygen ion moves upwards in order to release the B-O pair potential in **figure 3.3b**. For the ⟨111⟩ direction, three oxygen ions along a perpendicular direction to the [111] direction need to be displaced, and this motion reduces the electrostrictive property shown in **figure 3.3b**. Therefore, under an electric field along the $[001]_C$ direction, the maximum value of the electrostrictive coefficient contributes to the ultrahigh value of d_{33} in 4R and 4O domain-engineered single crystals [119,120].

3.2.3 Feature of '2R' configuration

Intense attention was focused on the '2R' domain configuration of [011]-poled rhombohedral single crystal. The uniqueness of this configuration is due to the simultaneously high values of its longitudinal, shear, and transverse piezoelectric properties. Furthermore, it presents a greater mechanical quality factor than that of the 4R domain configuration because of the lower polarization rotation angle [121-125].

3.2.4 Anisotropy of Q_m

Another important anisotropic property of relaxor-PT crystals was found in the mechanical quality factory in modified relaxor-PT ferroelectric crystals [126-129]. Generally, in relaxor-PT single crystal, Q_{33} is high but Q_{15} is lower. This is due to the fact that a larger polarization rotation angle is involved in the case of the shear property than that of longitudinal response. Improvement of the mechanical quality factor in Mn-modified single crystal is because the defect dipole-induced internal bias inhibits polarization rotation [68,32,76,130]. There is another pinning effect that is revealed when an electric field is applied along the lateral direction. Zheng *et al.* determined that in [001]-poled PIN-PMN-27PT:Mn single crystal, the internal bias was 1.44 kV/cm with the external electric field parallel to the poling direction, while it was 0.12 kV/cm with a perpendicular external field. In addition, with a perpendicular electric field, the external contribution to piezoelectricity is 3.7 times lower than that of the parallel electric field. With manganese doping, however, Q_{33} and Q_{15} are improved to 360 % and 400 %, respectively, indicating that another pinning mechanism serves for the shear direction [131]. In unpoled ferroelectrics, neutral domain walls minimize elastic energy. In a manganese-doped sample, however, 109° charged domain walls are favorable. In charged domain walls, due to the repelling force of opposite charges, Mn ions stay in head-to-head positions in the domain wall while oxygen vacancies are pushed to the tail-to-tail position. Consequently, a strong electrostatic force is created that is hard to break by a transverse electric field. Such charged domains clamp domain wall motion and inhibit polarization rotation in the lateral direction rather than the internal field [131,132].

3.3 Application Perspectives

In general, the giant electromechanical coupling factor and ultrahigh piezoelectric property in relaxor-PT single crystals enable them to carry out the higher broadband operation and exhibit better sensitivity in transducer applications when compared to those properties in traditional PZT ceramics [3,12]. This section discusses perspectives on the current progress on relaxor-PT crystals and provides some current examples for electromechanical applications.

3.3.1 Doping advantage

Piezoelectric materials are widely applied in underwater acoustic transducers. For underwater acoustics, the most common designs comprise the cymbal, 1–3 composite, and Tonpilz designs [65,133]. PMN-PT single crystals have been used as the active element in Tonpilz transducers, and they featured an expanded bandwidth and reduced stack length, owing to the high electromechanical coupling factor of the single crystals [66,134–136]. Despite some performance improvements in the Tonpilz design, a crucial issue has been the self-heating in piezoelectric elements, which is associated with a low mechanical quality factor and high loss of the single crystals. A Mn-PIN-PMN-PT element in the Tonpilz design was proven to exhibit excellent energy conversion with the least heat dissipation when compared to its PMN-PT and PIN-PMN-PT counterparts [130,133]. In addition, the Mn-modified Tonpilz design showed great stability of principal properties over operational limits of driving field and temperature. In **Figure 3.4**, the bandwidths of Tonpilz are compared with three generation of the single crystals and the conventional ceramic material. A Mn-modified transducer also exhibited superior bandwidth and energy source level to those of conventional ceramic-made transducers and higher mechanical quality factor compared to PMN-PT and PIN-PMN-PT transducers [137]. All these improvements are attributed to restricted polarization rotation and pinned domain wall motion caused by the “hardening effect”. Low heat generation was also observed in other types of underwater acoustic devices when using Mn-doped single crystal. For instance, a Mn-PIN-PNM-PT flextensional transducer exhibits lower heat generation than unmodified single crystals and PZT polycrystals [138].

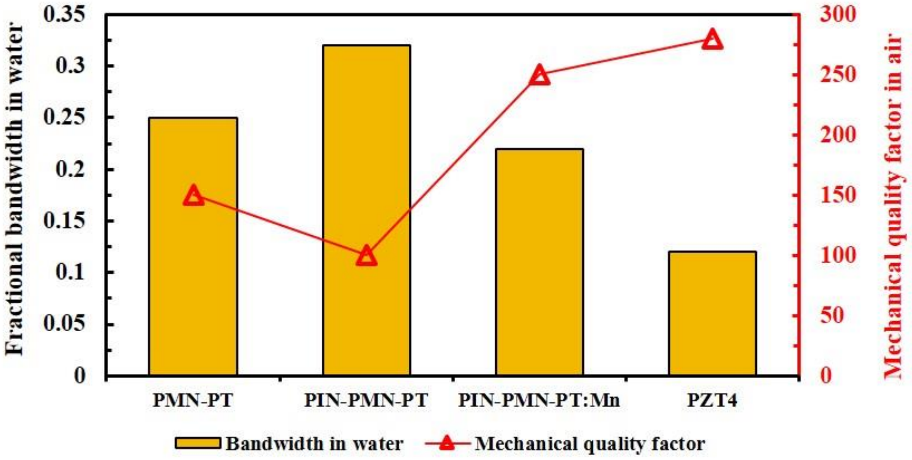

Figure 3.4 Bandwidths and quality factors of Tonpilz-design transducers made of PMN-PT,PIN-PMN-PT, Mn-modified PIN-PMN-PT crystals and PZT4 ceramic [137].

Relaxor-PT single crystals were confirmed to be suitable for use in a number of medical applications, including ultrasound diagnostic imaging, ultrasound therapy, and high intensity focused ultrasound, to mention a few [81,139]. The type of medical transducer and its application frequency range depends on the biological tissues [81]. The most important demand for medical transducers is for the improvement of imaging. Although the imaging depends on various characteristics of the device, the electromechanical coupling of the piezoelectric element makes the main contribution to the image resolution. Therefore, enhancement of the coupling factor is a crucial necessity for medical application [81,139]. Furthermore, high power medical transducers are intensively used in medical applications. The figure of the merit in medical applications, hence, is derived from high *k*. Overall, the relaxor-PT single crystals enhance the bandwidth and sensitivity of medical transducers [3,140–143]. In particular, the medical therapy devices work on the resonance frequency, signifying the requirement of a piezoelectric element with a high mechanical quality factor and low loss [140].

Medical transducers operate at higher frequencies 1-3 order higher than their underwater acoustic counterparts [3,81]. Principally, a higher frequency transducer requires smaller sizes of its piezoelectric material [3,12,139]. However, scaling degrades material’s property. **Figure 3.5** shows piezoelectric coefficient of PMN-PT single crystal which is a function of thickness.

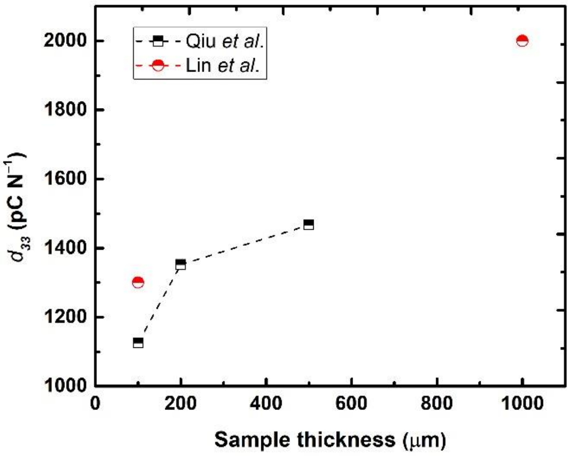

Figure 3.5 Longitudinal piezoelectric coefficient of PMN-PT single crystal is a function of sample's thickness [160,164].

Geometric features on relaxor-PT single crystals were shown to enhance the performance of miniaturized transducers [144,145]. For intravascular ultrasound transducer imaging, dimpled PMN-PT crystals at 30–80 MHz demonstrated a broader bandwidth, higher centre frequency, and sharper focus of images than those of their plane element counterparts, and the enhancement is associated with thickness reduction and multi-resonances varying along the concave surface, but at the cost of increase of the insertion loss [146,147]. The piezoelectric/epoxy composite design is one of the most promising approaches to improve transducer performance [140,143,148,149]. Relaxor-PT single crystals were successfully applied in the composite transducers [150–152]. The 1–3 crystal/polymer composite transducer is of particular interest. In this design, the best aspect ratio of the active element offers a great coupling factor, the low acoustic impedance provides better matching of energy between the transducer and the medium, and the composite array reduces lateral vibration modes [140,152–154]. Therefore, the 1–3 composite design improves transducer performance much more than the single piezo-element design does.

To achieve the device with high *k*, Mn-doped single crystal was applied in medical therapy applications. For instance, a Mn-modified PIN-PMN-PT-based needle transducer showed high performance up to 140 °C. Mn doping lowers the heat dissipation and allows the transducer to operate at elevated temperatures [155].

Drastic increases in dielectric and piezoelectric properties in donor-doped “soft” single crystals are very advantageous for electromechanical applications. Rare-earth Sm-doped PMN-PT single crystal possesses the largest values of d_{33} and $\varepsilon_{33}/\varepsilon_0$ among all the piezoelectric materials. These properties could be of particular benefit to high frequency medical transducers where giant property values would be less affected by the scaling process [91,96].

3.3.2 Poling advantage

High frequency electromechanical devices require small-sized piezoelectric materials as active elements. The scaling effect restricts the improvement of the electromechanical properties of ferroelectric single crystals for high frequency transducers. It was reported that smaller ferroelectric domains in 1–3 PIN-PMN-PT/epoxy transducer resulted in better electromechanical improvement than in a larger domain PMN-PT crystal, where the surface boundary clamped large domains [156,157]. It was also reported that high-temperature DC poling induced small-sized ferroelectric domains in relaxor-PT single crystal [13,36,39]. Therefore, small domains of single crystals induced by high-temperature poling could alleviate the scaling effect and achieve better electromechanical improvement in high-frequency transducers.

ACP-induced improvements of piezoelectric and electromechanical properties in relaxor-PT single crystals have made it possible to further broaden the bandwidth and thus, increase the sensitivity at a greater distance in transducer devices [158,159].

The piezoelectric and dielectric performances in Mn-doped PIN-PMN-PT are lower than the first- and the second-generation crystals [3,12,68]. The AC-poling technique could help reduce this gap. In AC-poled Mn-doped PIN-PMN-PT, $\varepsilon^T_{33}/\varepsilon_0$ and d_{33} increased to 45% and 29%, respectively (as shown in **table 3.2**). Longitudinal and lateral electromechanical coupling factors were also improved by ACP [42]. Therefore, the resulting property changes resulted in significant enhancement of the FOM $k^2 \cdot Q_m$ in transducer applications.

AC-poled relaxor-PT single crystals were also studied to understand the scaling effect. Increases of dielectric and piezoelectric properties in AC-poled PMN-PT crystals were higher than those in its DC-poled counterpart when the sample's thickness was as low as 100 μm. A scaling effect was observed in a 100 μm thick sample, but it was weak when the thickness was larger than 200 μm [160]. The weak scaling effect in AC-poled samples could support improvements of high-frequency transducer technology.

Multifunctional performance in ferroelectric materials has always been a challenge. For optical and electro-optical devices, searching for a material that has good properties in terms of both optics and piezoelectricity is a difficult quest. $LiNbO_3$ is a prototype material for optical communication and shows good transparency, but its piezoelectricity and electromechanical coupling are too low. Additionally, La-doped PZT ceramic is a good electrostrictor and possesses a good electro-optical coefficient, but it shows a polarization-dependent scattering loss [161]. The high multifunctional performance of AC-poled PMN-PT crystal was discussed in Section 3.1.2. Therefore, AC-poled relaxor single crystal is shown to be able to compensate for the disadvantages of the conventional materials and opens new frontiers for the improvement of optical and electro-optical devices [11].

3.3.3. Anisotropic advantage

From the applications point of view, the majority of studies on relaxor-PT crystals have been focused on the rhombohedral composition on the left side of the MPB or the pure MPB composition, owing to their ultrahigh piezoelectric and electromechanical properties. Nevertheless, the tetragonal single crystals have some advantages over their rhombohedral counterparts, having higher coercive fields, greater T_C, and no occurrence of a ferroelectric-to-ferroelectric phase transition up to T_C [99,162–164]. The anisotropic features of tetragonal relaxor-PT single crystals offer further potential for transducer applications. For high-frequency transducer devices, the piezoelectric element needs to be scaled down to a thin layer [81]. As mentioned above, however, the scaling involves property deterioration. Piezoelectric response reduces as the thickness of sample decreases shown in **figure 3.5**. The [111]-oriented tetragonal PIN-PMN-PT single crystal offers a higher frequency constant than those of its rhombohedral counterpart and of PZT ceramics, which is associated with a high elastic stiffness constant along the ⟨111⟩ direction in the perovskite structure. In addition, this single crystal shows a very high free and clamped longitudinal dielectric constant that benefits from the transverse dielectric constant of its single domain structure [165]. Hence, such advances in [111]-oriented tetragonal PIN-PMN-PT make it a favorable candidate for high-frequency transducer application. The ‘1T’ single domain tetragonal Mn: PIN-PMN-PT crystal possesses a large Q_m > ~2000. The high value of Q_m is related to the reduction of polarization rotation and the absence of domain wall motion, due to the single domain state and doping-induced E_i. Consequently, such a Mn-modified tetragonal single crystal provides the highest FOM $d{\cdot}Q$, giving it a perfect potential for high power transducer applications [79].

The anisotropic characteristic of relaxor-PT single crystal also offers better performance in the design of actuators [166,167]. The Zt ± 45° cut of [011]-oriented rhombohedral relaxor-PT crystal exhibits excellent face-shear properties of d_{36} and k_{36}, as well as high stability over different ranges of temperature and driving field [124,125]. The advantages of face-shear mode in [011]-poled Zt ± 45° cut PIN-PMN-0.30PT crystal allow to be used to develop an ultrasound motor with doubled values of its power density of $1.48{\cdot}10^{-4}$ W/mm^3 and its electromechanical coupling factor of 0.65, as well as a lower driving frequency (72 kHz), when compared to the prototype k_{31} mode PZT motor. Furthermore, the unique in-plane anisotropy of [011]-poled Zt ± 45° cut PMN-0.28PT single crystal was proven to be feasible material for linear ultrasound actuators [168]. The asymmetric and non-isomorphic face-shear mode of this sample provides the ultrasound motor with a greater driving field of 1.5 N under a lower driving voltage of 22 V_{pp} [169].

The low driven voltage and high driving field of face-shear mode have been paid immense attention. Heat dissipation is a serious concern, however, when ultrasound actuators operate at their resonance frequency. Hence, without improvement of the mechanical quality factor, it is impossible to achieve further advances in actuator applications using relaxor-PT single crystals. A k_{31}-mode typical ultrasound motor was developed using Mn-modified PIN-PMN-PT single crystal poled along the [001] direction. The motor achieved better output performance compared to those based on both PZT ceramic and face-shear relaxor-PT single crystal. The output power of Mn-modified motor is compared to those of face-shear and ceramic motors in **figure 3.6**. The output power density of 0.45 W/cm^3 was three times larger than those of a PZT ceramic motor and a face-shear relaxor-PT crystal motor. The reason for the enhancement was the low thermal generation, and in particular, it is ascribed to the "hardening effect" induced by dipole-defects arising from Mn-modification [170]. Therefore, in the case of resonance-based motor application, the Mn-doped relaxor-PT single crystal is advantageous over the face shear counterpart.

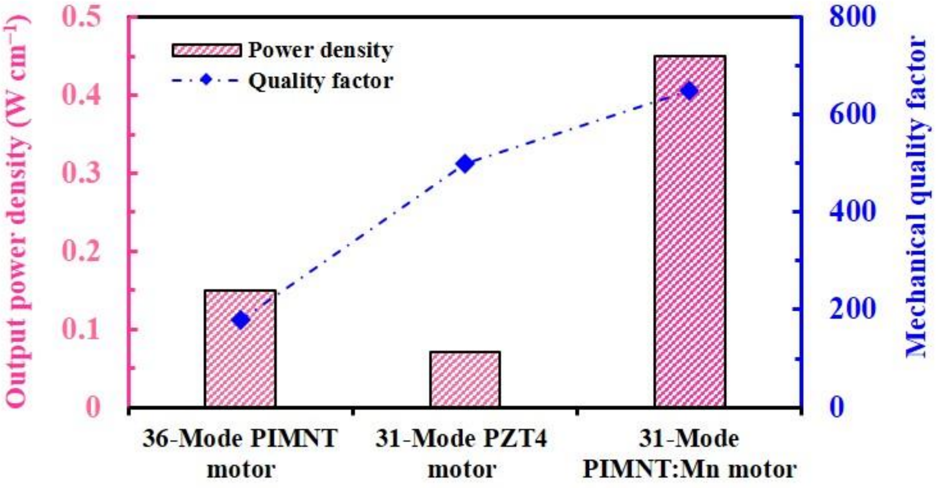

Figure 3.6 Output powers of 36-mode single crystal, 31-mode Mn-modified single crystals and 31-mode PZT4 ceramic ultrasound motors [127,167,170].

3.4 Growth methods of relaxor-PT ferroelectric crystals

Relaxor-PT single crystals are synthesized by different methods, including conventional flux growth, flux Bridgman growth, modified Bridgman growth, and solid-state conversion growth. This section highlights two growth methods: modified Bridgman growth and solid-state conversion growth. These two growth methods are suitable for the fabrication of single crystals with high quality on an industrial scale.

3.4.1 Modified Bridgman method

Bridgman technique (or also known as Bridgman-Stockbarger technique) is a straightforward ways of growing the relaxor-$PbTiO_3$ single crystals. P. W. Bridgman first reported a newly method for growth of metal crystals in 1924. **Figure 3.7** shows Bridgman's original mould that made of glass or quartz tubing. This tubing consisted of four parts: A, B, C and D in **figure 3.7**. Prior to the process beginning, mineral oil and petroleum ether are used to wash in order to detach crystallized material from inner walls. Sufficient amount of solid materials were introduced to the part B through the open mouth (part A). The mould with the filled materials was vertically placed in a furnace. Then it was heated up to higher temperature than that of material's melting point. After the material melted, the melt was poured down to the rest of the mould. The mould was lowered into cool air or cool oil bath to allow crystallization. Lowering is slower than the velocity of material's crystallization, and otherwise differently oriented crystal could be grown. Crystallization begins from the part D where the melt grew with several grains. The different grains compete to grow up but the narrow capillary between the part C and the part D filtered the most competitive single grain. Thus, this filtration helped grow a whole single crystal [171]. After his initial design, several modifications had been experimented. In 1933, D. C. Stockbarger brought a more sophisticated modification. He used vertically positioned two furnaces with different temperatures, upper of which was at higher temperature than that of lower furnace had lower temperature, where sufficient thermal gradient could occur to solidify molten. He used vertically separated two furnaces and platinum crucible [172].

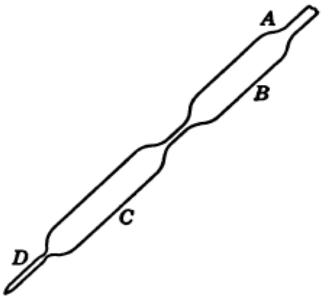

Figure 3.7 Bridgman's original tubing for crystal growth [178].

By using this method, large, high-quality relaxor-PT single crystals can be grown [172-189]. The material is melted at a higher temperature than its melting point. Then, it is slowly transported into a lower temperature zone. During the transport, the melt is gradually crystallized through the temperature gradient and solidus line of the solid solution phase diagram [171,175]. Prior to the crystal growth, it is necessary to pre-synthesize $MgNb_2O_6$ to avoid achieving parasitic-pyrochlore phase, using the two-step Columbite precursor method [181]. The sintered ceramic sample is introduced into an ultrapure platinum crucible. The high purity of the crucible prevents any reaction between the melting materials and the platinum [175]. The platinum crucible is sealed, and then placed in a cylindrical alumina crucible. The space between the two crucibles is filled with alumina sand for the purposes of supporting the Pt crucible and absorption of any volatiles. The alumina crucible is then placed on a ceramic tube that is part of the translation system. General scheme for Bridgman growth method is exhibited in **figure 3.8**. The furnace used in Bridgman growth method consists of two zones. Zone I provides high temperature where the material is melted. In zone II, there is lower temperature given for generation of temperature gradient between the two zones while the charge is being moved. After the material is melted, the ingot is dwelled for a certain period. Then, the translation system moves the charge down to zone II with a speed that is slower than that of the material's crystallization [175,177]. Usually, the charge is translated with the rate of 0.6-1.0 mm/h. It is common that the temperature gradient is higher than 20 °C/cm. The temperature of the crystallization process is monitored by several thermocouples. One thermocouple controls zone I while other one measures the zone II. Also, another thermocouple estimates the temperature gradient in alumina crucible. Single crystals can be grown along the major crystallographic orientations of <111>, <110> and <001>. To control the growth orientation, an orientated single-crystal seed is used [176,177].

Shimanuki and colleagues grew the first relaxor-PT single crystal using the vertical Bridgman method. They charged a mixture powder of highly pure oxides into cylindered platinum crucible and, then suspended it inside of a high temperature furnace. The oxide mixture is covered by PbO powder as a flux. Then the charge was suspended inside the furnace, and it was then moved down to the lower zone to be crystallized. They successfully grew PZN-PT single crystals. However, they could not avoid compositional segregation [187]. H. Luo *et al*, modified the Bridgman technique and reported the larger single crystal of PMN-PT. There were several advances in their work. They used ultra-high pure oxide powders, charged them into platinum crucible and sealed it to prevent from evaporation of volatiles. In addition, instead of the suspension technique, an automatic up-down mechanism was used to control the charge movement, a platinum crucible was shaped to a tapered end enabling a single crystal growth, and the crucible was also sealed with a lid that protected the contents from volatile at high temperature. The melting point was chosen based on thermogravimetric measurements. The properties of the single crystal are: piezoelectric charge coefficient, d_{33} > 2000 pC/N, dielectric constant, ε~5500, and electromechanical coupling factor, k_{33}~93% at the MPB [172,178]. Zawilski and co-workers conducted detailed composition study of the as-grown single crystal. They grew PMN-PTs (with 0.1PT and 0.35PT) and found that composition varied from 0.30 to 0.70 PT along growing axis of whole boule [179]. **Figure 3.9** exhibits longitudinal piezoelectric coefficients of compositions near to the MPB and the MPB compositions in PMN-PT single crystals.

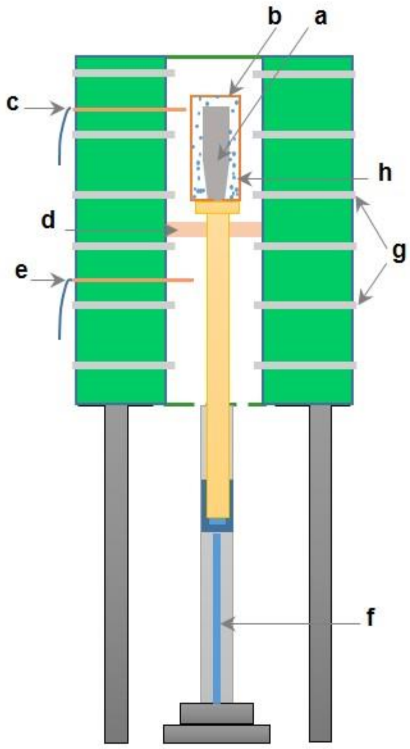

Figure 3.8 Schematic diagram of vertical Bridgman furnace. a. platinum crucible, b. alumina crucible, c. thermocouple for zone I, d. adiabatic zone, e. thermocouple for zone II, f. lifting mechanism, g. heating elements, h. alumina balls.

Composition segregation is an unavoidable disadvantage of the Bridgman method for growing solid solution crystals. Because of different melting points and various densities of the composition members, this method is unavoidably producing inhomogeneous products. Ti^{4+} cation is the most segregated ion while Pb^{2+} cation is relatively homogeneous along the growth axis of the as-grown boule. This segregation leads to property variation and cost increase [18,19,173,180,189]. It is found that property homogeneity is stable in the radial direction but varies along the growth direction [175]. For instance, magnesium oxide and lead oxide melt at 1285 °C and 886 °C, respectively. In addition, distinctions between components' density affect homogeneity. Density of magnesium oxide is 3.58 g/cm^3 while lead oxide has density of 9.53 g/cm^3.

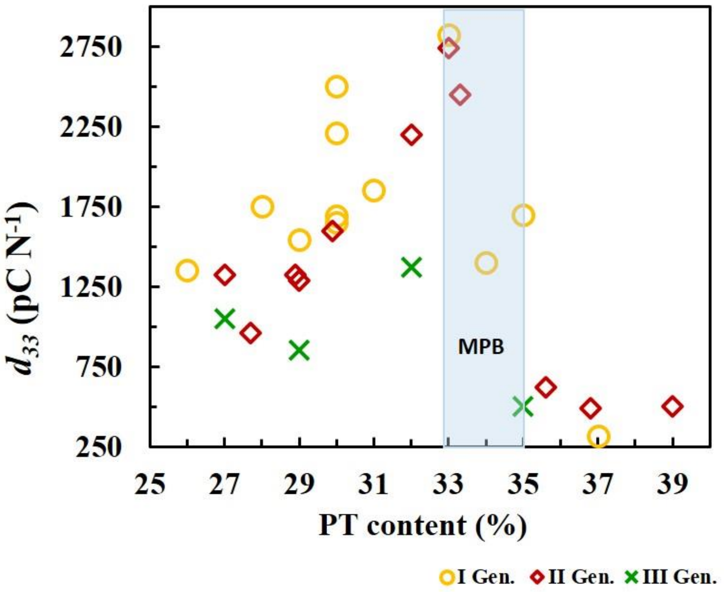

Figure 3.9 Longitudinal piezoelectric coefficients in three generation relaxor-PT crystals [31,33,45,75,103,114,174,180,189].

To avoid compositional variation, Zawilski et al. used the vertical zone levelling technique, resulting in homogeneous Ti^{4+} content over a 60 mm length along the growth direction [190].

Rare-earth doped PMN-PT single crystal also showed a reduced property variation along the growth direction. In Sm-doped PMN-PT single crystals, Sm^{3+} and Ti^{4+} cations favour the tetragonal phase but the segregation of these two cations show opposite trend, and as a result, property homogeneity is expanded [96].

The continuous feeding Bridgman method (CFBG) is an advanced modified method with advantages for addressing size and segregation issues. During the crystallization, pre-synthesized material of the same composition is continuously introduced into the melt to enlarge the final boule. This modification also provides uniform distributions of the 0.70PMN–0.30PT, 0.24PIN–0.46PMN–0.30PT and 0.31PIN–0.43PMN–0.26PT compositions along the axis direction [191–193]. The PMN-PT single crystal with 80 mm in diameter and 320 mm in length was grown with this method, and variations of d_{33} and Ti^{4+} segregation were within 10% and 6% along the growth direction, respectively [191]. In the case of a PIN-PMN-PT single crystal, the property variation and Ti^{4+} segregation were reduced to 15% and 6%, respectively, over the axis length of the as-grown boule [193].

The multi-crucible configuration is another modified Bridgman method for both reducing cost and increasing mass production [175,194,195]. In this modified method, the high-temperature furnace has five chambers, each of which comprises three zones: upper, hot, and lower. Using this configuration, Han et al. grew PMN-PT crystals with 75 mm in diameter [175]. In the case of PIN-PMN-PT crystal, the size of the grown crystal was 101.6 mm in diameter and 100 mm in length [194].

The Bridgman growth method is a consistent way of growing large, high-quality single crystals. This method has the disadvantage of compositional non-uniformity. There have recently been several advances on this issue, however, including doping, continuous feeding, and multi-furnace growth. These advances enable the production of large crystals with low cost and a higher grade for commercial needs.

3.4.2 Solid-State Conversion Growth Method

In the modified Bridgman methods, cost and operational complications remain unsolved. The flux method for the growth of single crystals is an alternative way for simple operation and fabricating homogenous single crystals. However, its small quantity of output is inconvenient for mass production.

The solid-state conversion growth (SSCG) method has appreciable advantages with respect to cost and operational complications over the melt growth methods. This method could produce cost-efficient, homogeneous, and large single crystals. The operation for crystal growth is also simpler compared to the melt growth methods.

In polycrystalline materials, grains grow in two major ways: normal grain growth and non-normal grain growth. In the real system, non-normal grain growth occurs, and different models for it have been proposed. Abnormal grain growth (AGG) is a type of non-normal grain growth, [196–198]. In AGG, the grains grow via either atomic diffusion or interface reaction, depending on the driving force for migration of boundary. In AGG, faceted boundary migration is dominant [199,200]. By applying the grain growth mechanism, a polycrystalline material could be converted into a single crystal [196,201-207]. In the polycrystalline-single crystal conversion process, a single crystal seed is used to nucleate the AGG. Here, the seed could act as a large AGG grain that consumes the fine grains of the matrix to further grow the single crystal. As shown in **Figure 3.10**, the seed with preferred orientation could be either embedded or bonded in the matrix, depending on the characteristics of the particular material. Afterwards, the sample is annealed at a high temperature but below the melting point. This method is therefore useful for materials that have a high melting point and easy volatility. The most important aspect of the conversion method is controlling the microstructure [200,208]. Generally, a non-uniform grain-size distribution of the matrix entails AGG grains in a matrix. When the matrix AGG grains are nucleated, they impinge on the newly grown single crystal and restrict its growth. It is therefore crucial to provide fine grains in the matrix. To control the grains in the matrix, dopants are used to inhibit AGG of the matrix. Li_2O dopant, for instance, reduces the critical driving force of grain growth, and leads to small grains [209]. Porosity is the main drawback of the SSCG method. Pores degrade the physical properties of single crystals. Various attempts have been studied to reduce the porosity, where adding a dopant is one of the ways [210]. Choosing an [001]-oriented seed is another way because the low speed of growth leads to minimum porosity and this orientation provides the slowest growth rate compared to the [111] and [110] orientations [211]. Changing the atmosphere, such as the oxygen pressure for sintering, could also reduce pores [209]. Of particular importance is that hot-pressing of the ceramic matrix will positively reduce porosity in the as-grown crystal [212,213].

Relaxor-PT crystals, including PMN-PT and $Pb(Mg_{1/3}Nb_{2/3})O_3$–$PbZrO_3$–$PbTiO_3$ (PMN-PZ-PT) single crystals, were successfully grown by the SSCG method. A certain excess of PbO was added to increase the kinetics of growth. This is because the liquid phase of PbO wets the grain boundaries during the sintering [209,211-214]. For relaxor-PT single crystal growth, the seed is chosen with regard to growth kinetics [211,214], stability [212,215], and lattice matching [209]. The properties of early single crystals grown by SSCG were inferior to those grown by the melt growth methods. Due to the successful attempts to overcome the porosity issue, however, the relaxor-PT single crystals grown by the SSCG method produced quite similar piezoelectric and electromechanical responses to those grown by the melt methods [212,215]. In addition, since the SSCG method has demonstrated that it could produce large size commercial products with high piezoelectric performance, this technique is able to directly grow specifically designed crystals for a particular application [196,200], leading to savings in time and cost.

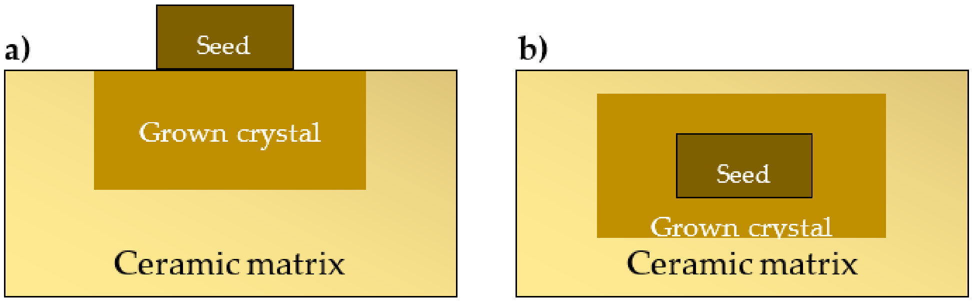

Figure 3.10 Crystal growth from seed into ceramix matrix. (a) templeted growth and (b) embedded growth.

3.5 Summary

The current progress on relaxor-PT ferroelectric crystals and their opportunities in electromechanical applications have been reviewed. Two single crystal growth methods were emphasized, the modified Bridgman and solid-state conversion growth methods. These methods provide an adequate way of fabricating large quantities of relaxor-PT single crystals. Both methods have struggled with the quality of their as-grown crystals, although recent progress on these methods has been solving this issue.

Doping was proved to be an efficient strategy for achieving improvements in piezoelectric and electromechanical performance. Acceptor doping exhibits a “hardening” effect, which leads to improved mechanical coupling and reduced loss, while donor doping demonstrates a “softening” effect that results in enhanced piezoelectricity and electromechanical coupling. In the “hard” piezoelectric single crystals, doping-induced defect-dipoles pin domain wall motion and restrict polarization rotation, so that heat dissipation is reduced. Therefore, “hard” single crystals benefit the high-power transducer and ultrasonic motor applications. Enhanced dielectric and piezoelectric properties induced by donor dopants are advantageous, especially for high-frequency transducer devices. The poling technique is another effective way of increasing piezoelectric and electromechanical properties. High-temperature DC-poling was confirmed to increase the piezoelectric response. Recently, AC-poling has been intensively studied. This technique offers much more improvement of dielectric and piezoelectric properties than for the DC-poling method in relaxor-PT crystals. This technique also increases coupling factors. The induced property improvements in the single crystals pave the way for the improvement of diverse electromechanical applications. The anisotropy of relaxor-PT single crystals always offers unique features in the material’s behavior.

3.6 Prospective

Intensive attempts have been focused on improving the compositional homogeneity of the as-grown crystals using the modified Bridgman growth method. SSCG is an alternative method to produce more homogeneous crystals at low cost. Meanwhile, since melting does not occur during SSCG, relaxor-PT crystals with refractory components have been successfully achieved. It is expected relaxor-PT crystals with different end member components can increase the Curie temperature and coercive field, enabling a broader usage temperature range and drive stability compared with their binary PMN-PT and ternary PIN-PMN-PT counterparts.

Ferroelectric materials must be poled to exhibit piezoelectricity. The poling condition is extremely important for a ferroelectric material, which has been actively studied in the last many decades. ACP technique attracts immense attention in relaxor-PT ferroelectric crystals because it greatly benefits the piezoelectric and dielectric properties. However, the underlying mechanism responsible for the ACP induced property enhancement is still open, meanwhile the reliability and stability of the property under different external stimuli, including electric field, stress field and temperature, are not yet fully understood. Thus further research on the ACP poled ferroelectric crystals is desired in order to take full advantage of the enhanced properties for practical electromechanical applications

Reference

[1] L. Baasandorj, and Z. Chen, Recent developments on relaxor-$PbTiO_3$ ferroelectric crystals. *Crystals*, **12**, 56 (2022).

[2] B. Jaffe, W. R. Cook and H. Jaffe, “Piezoelectric Ceramics”, Academic press Inc. (London) Ltd, 1971, London, pp 7-11, 15.

[3] S. Zhang, and F. Li, High performance ferroelectric relaxor-$PbTiO_3$ single crystal: Status and perspective, *J. Appl. Phys* **111**, 031301 (2012).

[4] S. E. Park and T. R. Shrout, Ultrahigh strain and piezoelectric behavior in relaxor based ferroelectric single crystals, *J. Appl. Phys*., **82**, 1804 (1997).

[5] G. Liu, L. Kong, Q. Hu, S. Zhang, Diffused morphotropic phase boundary in relaxor-$PbTiO_3$ crystals: High piezoelectricity with improved thermal stability. *Appl. Phys. Rev*., **7**, 021405 (2020).

[6] F. Li, S. Zhang, T. Yang, Z. Xu, N. Zhang, G. Liu, J. Wang, J. Wang, Z. Cheng, Z.-G.Ye, J. Luo, T. R. Shrout and L.-Q. Chen, The origin of ultrahigh piezoelectricity in relaxor-ferroelectric solid solution crystals, *Nat. Commun*, **7**, 13807 (2016).

[7] F. Li, S. Zhang, D. Damjanovic, L. Q. Chen, and T. R. Shrout, Local structural heterogeneity and electromechanical responses of ferroelectrics: learning from relaxor ferroelectrics, *Adv. Func. Mater*. **28**, 1801504 (2018).

[8] A. J. Bell, Phenomenologically derived electric field-temperature phase diagrams and piezoelectric coefficients for single crystal barium titanate under fields along different axes. *J. Appl. Phys*. **89**, 3907-3914 (2001).

[9] S. E. Park and T. R. Shrout, Relaxor based ferroelectric single crystals for electro-mechanical actuators. *Mater. Res. Innov*., **1**, 20-25 (1997)

[10] J. Xu, H. Deng, Z. Zeng, Z. Zhang, K. Zhao, J. Chen, N. Nakamori, F. Wang, J. Ma, X. Li, H. Luo, Piezoelectric performance enhancement of $Pb(Mg_{1/3}Nb_{2/3})O_3$-$0.25PbTiO_3$ crystals by alternating current polarization for ultrasonic transducer. *Appl. Phys. Lett*., **112**, 182901 (2018).

[11] C. Qiu, B. Wang, N. Zhang, S. Zhang, J. Liu, D. Walker, Y. Wang, H. Tian, T. R. Shrout, Z. Xu, L. Q. Chen, F. Li, Transparent ferroelectric crystals with ultrahigh piezoelectricity. *Nature*, **577**, 350-354 *(*2020).

[12] S. Zhang, F. Li, X. Jiang, J. Kim, J. Luo, and X. Geng, Advantages and challenges of relaxor-$PbTiO_3$ ferroelectric crystals for electroacoustic transducers–A review. *Prog. Mater. Sci.*, **68**, 1-66 (2015).

[13] Z. Feng, X. Zhao, H. Luo, Effect of poling field and temperature on dielectric and piezoelectric property of ⟨001⟩-oriented $0.70Pb(Mg_{1/3}Nb_{2/3})O_3$–$0.30PbTiO_3$ crystals. *Mater. Res. Bull.*, **41**, 1133-1137 (2006).

[14] M. Davis, Phase transitions, anisotropy and domain engineering: the piezoelectric properties of relaxor-ferroelectric single crystals. Doctoral dissertation, EPFL, Lausanne, Swiss, 2006.

[15] J. Han and W. Cao, Electric field effects on the phase transitions in [001]-oriented $(1-x)Pb(Mg_{1/3}Nb_{2/3})O_3$-$xPbTiO_3$ single crystals with compositions near morphotropic phase boundary, *Phys. Rev. B*, **68**, 134102 (2003).

[16] Y. Guo, H. Luo, D. Ling, H. Xu, T. He and Z. Yin, The phase transition sequence and the location of the morphotropic phase boundary region in $(1 - x)[Pb(Mg_{1/3}Nb_{2/3})O_3]$–$xPbTiO_3$ single crystal, *J. Phys.: Condens. Matter.*,**15**, L77 (2003).

[17] Z. Li, Z. Xu, X. Yao, and Z.-Y. Cheng, Phase transition and phase stability in [110]-, [001]-, and [111]-oriented 0.68Pb(Mg1/3Nb2/3)O3−0.32PbTiO3 single crystal under electric field, *J. Appl. Phys.*, **104**, 024112 (2008).

[18] E. V. Colla, N. K. Yushin, D. Viehland, Dielectric properties of $(PMN)_{(1-x)}(PT)_x$ single crystals for various electrical and thermal histories, *J. Appl. Phys*, 83, 3298 (1998).

[19] X. Zhao, B. Fang, H. Cao, Y. Guo and H. Luo, Dielectric and piezoelectric performance of PMN-/PT single crystals with compositions around the MPB: influence of composition, poling field and crystal orientation, *Mater. Sci. Eng.*, **B96**, 254-/262 (2002).

[20] J. Kuwata, K. Uchino and S. Nomura, Dielectric and piezoelectric properties of $0.91Pb(Zn_{1/3}Nb_{2/3})O_3$-$0.09PbTiO_3$ single crystals, *Jpn. J. Appl. Phys.*, **21**, 1298-1302 (1982).

[21] Y. Guo, H. Luo, K. Chen, H. Xu, X. Zhang and Z. Yin, Effect of composition and poling field on the properties and ferroelectric phase-stability of $Pb(Mg_{1/3}Nb_{2/3})O_3$–$PbTiO_3$ crystals, *J. Appl. Phys.*, **92**, 6134 (2002).

[22] A. A. Bokov, Z. G. Ye, Field-induced shift of morphotropic phase boundary and effect of overpoling in $(1-x)Pb(Mg_{1/3}Nb_{2/3})O_3$–$xPbTiO_3$ piezocrystals. *Appl. Phys. Lett.*, **92**, 082901 (2008).

[23] C. S. Tu, R. R. Chien, S. C. Lee, V. H. Schmidt, H. Luo, Rapid piezoelectric response and origin in (001)$Pb(In_{1/2}Nb_{1/2})_{0.70}Ti_{0.30}O_3$ crystal. *J. Appl. Phys.*, **106**, 016102 (2009).

[24] C. S. Tu, C. M. Hsieh, V. H. Schmidt, R. R. Chien, H. Luo, Piezoelectric response and origin in (001)$Pb(Mg_{1/3}Nb_{2/3})_{0.70}Ti_{0.30}O_3$ crystal. *Appl. Phys. Lett.*, **93**, 172905 (2008).

[25] Z. Jiang, Over-poling study of PMN-PT and PIN-PMN-PT crystal grown by Vertical Gradient Freeze method. In 2016 Joint IEEE International Symposium on the Applications of Ferroelectrics, European Conference on Application of Polar Dielectrics, and Piezoelectric Force Microscopy Workshop (ISAF/ECAPD/PFM), Darmstadt, Germany, pp. 1-4.

[26] N. Yamamoto, Y. Yamashita, K. Itsumi, Y. Hosono, Temperature dependence of dielectric constant with different poling fields in lead magnesium niobate-lead titanate single crystal. *Trans. Mater. Res. Soc. Jpn.*, **35**, 95-98 (2010).

[27] H. Y. Chen, C. S. Tu, C. M. Hung, R. R. Chien, V. H. Schmidt, C. S. Ku, H. Y. Lee, Poling effect and piezoelectric response in high-strain ferroelectric $0.70Pb(Mg_{1/3}Nb_{2/3})O_3$–$0.30\ PbTiO_3$ crystal. *J. Appl. Phys.*, **108**, 044101 (2010).

[28] Z. Chen, L. Hong, F. Wang, S. P. Ringer, L . Q. Chen, H. Luo, X. Liao, Facilitation of ferroelectric switching via mechanical manipulation of hierarchical nanoscale domain structures. *Phys. Rev. Lett.*, **118**, 017601 (2017).

[29] Z. Chen, L. Hong, F. Wang, X. An, X. Wang, S. Ringer, L. Q. Chen, H. Luo, X. Liao, Kinetics of domain switching by mechanical and electrical stimulation in relaxor-based ferroelectrics. *Phys. Rev. Appl.*, **8**, 064005 (2017).

[30] Z. Chen, F. Li, Q. Huang, F. Liu, F. Wang, S. P. Ringer, H. Luo, S. Zhang, L. Q. Chen, X. Liao, Giant tuning of ferroelectricity in single crystals by thickness engineering. *Sci. Adv.*, **6**, eabc7156 (2020).

[31] Q. Huang, Z. Chen, M. J. Cabral, F. Wang, S. Zhang, F. Li, Y. Li, S. P. Ringer, H. Luo, Y. W. Mai, X. Liao, Direct observation of nanoscale dynamics of ferroelectric degradation. *Nat. Commun.*, **12**, 1-7 (2021).

[32] B. Noheda, Z. Zhong, D. E. Cox, G. Shirane, S. E. Park, P. Rehrig, Electric-field-induced phase transitions in rhombohedral $Pb(Zn_{1/3}Nb_{2/3})_{1-x}Ti_xO_3$. *Phys. Rev. B*, **65**, 224101 (2002).

[33] F. Bai, N. Wang, J. Li, D. Viehland, P. M. Gehring, G. Xu, G. Shirane, X-ray and neutron diffraction investigations of the structural phase transformation sequence under electric field in $0.7Pb(Mg_{1/3}Nb_{2/3})$-$0.3PbTiO_3$ crystal. *J. Appl. Phys.*, **96**, 1620-1627 (2004).

[34] Y. Wang, D. Wang, G. Yuan, H. Ma, F. Xu, J. Li, D. Viehland, P. M. Gehring, Fragile morphotropic phase boundary and phase stability in the near-surface region of the relaxor ferroelectric $(1-x)Pb(Zn_{1/3}Nb_{2/3})O_3-xPbTiO_3$:[001] field-cooled phase diagrams. *Phys. Rev. B*, **94**, 174103 (2016).

[35] F. Li, L. Wang, L. Jin, Z. Xu, S. Zhang, Achieving single domain relaxor-PT crystals by high temperature poling. *CrystEngComm*, **16**, 2892-2897 (2014).

[36] W. Hu, Z. Xi, P. Fang, W. Long, X. Li, Q. Bu, A novel poling technique to obtain excellent piezoelectric properties of $Pb(Mg_{1/3}Nb_{2/3})O_3$–$0.32PbTiO_3$ single crystals. *J. Mater. Sci. Mater. Electron.*, **26**, 3282-3286 (2015).

[37] F. Li, S. Zhang, Z. Xu, Z. Li, X. Wei, DC bias electric field dependent piezoelectricity for [001] poled $Pb(In_{1/2}Nb_{1/2})O_3$–$Pb(Mg_{1/3}Nb_{2/3})O_3$–$PbTiO_3$ crystals. *J. Adv. Dielectr.*, **1**, 303-308 (2011).

[38] D. Lin, S. Zhang, Z. Li, F. Li, Z. Xu, S. Wada, J. Luo, T. R. Shrout, Domain size engineering in tetragonal $Pb(In_{1/2}Nb_{1/2})O_3$-$Pb(Mg_{1/3}Nb_{2/3})O_3$-$PbTiO_3$ crystals. *J. Appl. Phys.*, **110**, 084110 (2011).

[39] Z. Y. Shen, Y. Tang, S. Zhang, J. Luo, Y. Li, T. R. Shrout, Enhanced piezoelectric activity and temperature stability of [111]-oriented orthorhombic $0.68Pb(Mg_{1/3}Nb_{2/3})O_3$–$0.32PbTiO_3$ single crystals by domain size engineering. *Scr. Mater.*, **72**, 17-20 (2014).

[40] W. Y. Chang, C. C. Chung, C. Luo, T. Kim, Y. Yamashita, J. L. Jones,

X. Jiang, Dielectric and piezoelectric properties of $0.7Pb(Mg_{1/3}Nb_{2/3})O_3$-$0.3PbTiO_3$ single crystal poled using alternating current. *Mater. Res. Lett.* **2018**, *6*, 537-544.

[41] C. Luo, T. Karaki, Z. Wang, Y. Sun, Y Y. Yamashita, J. Xu, Ultrahigh piezoelectricity after field cooling AC poling in ferroelectric crystals manufactured by continuous-feeding Bridgman. DOI: 10.21203/rs.3.rs-334314/v1.

[42] H. Wan, C. Luo, C. C. Chung, Y. Yamashita, X. Jiang, Enhanced dielectric and piezoelectric properties of manganese-doped $Pb(In_{1/2}Nb_{1/2})O_3$-Pb $(Mg_{1/3}Nb_{2/3})O_3$-$PbTiO_3$ single crystals by alternating current poling. *Appl. Phys. Lett.*, **118**, 102904 (2021).

[43] Y. Sun, T. Karaki, T. Fujii, Y. Yamashita, Alternate current poling and direct current poling for $Pb(Mg_{1/3}Nb_{2/3})O_3$–$PbTiO_3$ single crystals. *Jpn. J. Appl. Phys.*, **58**, SLLC06 (2019).

[44] M. Ma, S. Xia, K. Song, H. Guo, S. Fan, Z. Li, Enhanced dielectric and piezoelectric properties in the [001]-poled $0.25Pb(In_{1/2}Nb_{1/2})O_3$-$0.43Pb(Mg_{1/3}Nb_{2/3})O_3$-$0.32PbTiO_3$ single crystal near morphotropic phase boundary by alternating current treatment. *J. Appl. Phys.*, **127**, 064106 (2020).

[45] L. Guo, B. Su, C. Wang, X. He, Z. Wang, X. Yang, X. Long, C. He, Orientation dependence of dielectric and piezoelectric properties of tetragonal relaxor ferroelectric single crystals by alternate current poling. *J. Appl. Phys.*, **127**, 184104 (2020).

[46] C. He, T. Karaki, X. Yang, Y. J. Yamashita, Y. Sun, X. Long, Dielectric and piezoelectric properties of $Pb[(Mg_{1/3}Nb_{2/3})0.52(Yb_{1/2}Nb_{1/2})0.15Ti_{0.33}]O_3$ single-crystal rectangular plate and beam mode transducers poled by alternate current poling. *Jpn. J. Appl. Phys.*, **58**, SLLD06 (2019).

[47] D. Vanderbilt, M. H. Cohen, Monoclinic and triclinic phases in higher-order Devonshire theory. *Phys. Rev. B*, **63**, 094108 (2001).

[48] B. Noheda, D. E. Cox, G. Shirane, S. E. Park, L. E. Cross, Z. Zhong, Polarization rotation via a monoclinic phase in the piezoelectric 92%$PbZn_{1/3}Nb_{2/3}O_3$-8%$PbTiO_3$. *Phys*. *Rev*. *Lett*., **86**, 3891 (2001).

[49] C. Qiu, Z. Xu, Z. An, J. Liu, G. Zhang, S. Zhang, L. Q. Chen, N. Zhang, F. Li, In-situ domain structure characterization of $Pb(Mg_{1/3}Nb_{2/3})O_3$-$PbTiO_3$ crystals under alternating current electric field poling. *Acta Mater*., **210**, 116853 (2021).

[50] H. Wan, C. Luo, C. Liu, W. Y. Chang, Y. Yamashita, X. Jiang, Alternating current poling on sliver-mode rhombohedral $Pb(Mg_{1/3}Nb_{2/3})O_3$-$PbTiO_3$ single crystals. *Acta Mater*., **208**, 116759 (2021).

[51] J. Liu, C. Qiu, L. Qiao, K. Song, H. Guo, Z. Xu, F. Li, Impact of alternating current electric field poling on piezoelectric and dielectric properties of $Pb(In_{1/2}Nb_{1/2})O_3$–$Pb(Mg_{1/3}Nb_{2/3})O_3$–$PbTiO_3$ ferroelectric crystals. *J*. *Appl*. *Phys*., **128**, 094104 (2021).

[52] B. Wang, F. Li, L. Q. Chen, Inverse domain-size dependence of piezoelectricity in ferroelectric crystals. *Adv*. *Mater*., 2105071 (2021).

[53] M. Ma, S. Xia, K. Song, H. Guo, Z. Xu, Z. Li, Temperature dependence of the transverse piezoelectric properties in the [001]-poled $0.25Pb(In_{1/2}Nb_{1/2})O_3$-$0.42Pb(Mg_{1/3}Nb_{2/3})O_3$-$0.33PbTiO_3$ single crystal with alternating current treatment. *J*. *Appl*. *Phys*., **129**, 114102 (2021).

[54] T. Deng, B. Fang, Z. Chen, J. Chen, H. Luo, Improving fatigue resistance of PIMNT single crystal via two-step poling process. *J*. *Phys*. *Chem*. *Solids*, **161**, 110378 (2022).

[55] Y. Sun, T. Karaki, T. Fujii, Y. J. Yamashita, Spurious-mode vibrations caused by alternating current poling and their solution process for $Pb(Mg_{1/3}Nb_{2/3})O_3$-$PbTiO_3$ single crystals. *J*. *Materiomics* (2021), https://doi.org/10.1016/j.jmat.2021.05.002.

[56] C. Luo, T. Karaki, Y. J. Yamashita, J. Xu, High temperature and low voltage AC poling for $0.24Pb(In_{1/2}Nb_{1/2})O_3$-$0.46Pb(Mg_{1/3}Nb_{2/3})O_3$-$0.30PbTiO_3$ piezoelectric single crystals manufactured by continuous-feeding Bridgman method. *J*. *Materiomics*, **7**, 621-628 (2021).

[57] H. Wan, C. Luo, W. Y. Chang, Y. Yamashita, X. Jiang, Effect of poling temperature on piezoelectric and dielectric properties of $0.7Pb(Mg_{1/3}Nb_{2/3})O_3$-0.3PbTiO3 single crystals under alternating current poling. *Appl*. *Phys*. *Lett*., **114**, 172901 (2019).

[58] C. Luo, T. Karaki, Y. Sun, Y. J. Yamashita, J. Xu, Effect of field cooling AC poling on electrical and physical properties for $Pb(Mg_{1/3}Nb_{2/3})O_3$-$PbTiO_3$-based single crystals manufactured by a continuous-feeding Bridgman process. *Jpn. J. Appl. Phys.*, **59**, SPPD07 (**2020)**.

[59] C. Luo, H. Wan, W. Y. Chang, Y. Yamashita, A. R. Paterson, J. Jones, X. Jiang, Effect of low-frequency alternating current poling on 5-mm-thick $0.7Pb(Mg_{1/3}Nb_{2/3})O_3$-$0.3PbTiO_3$ single crystals. *Appl. Phys. Lett.*, **115**, 192904 (2019).

[60] Y. Sun, T. Karaki, T. Fujii, Y. Yamashita, Enhanced electric property of relaxor ferroelectric crystals with low AC voltage high-temperature poling. *Jpn. J. Appl. Phys.*, **59**, SPPD08 (2020).

[61] H. Jiang, Y. K. Zou, Q. Chen, K. K. Li, R. Zhang, Y. Wang, H. Ming, and Z. Zheng, Transparent electro-optic ceramics and devices. *Proc. SPIE*, **5644,** 380-394 (2005).

[62] Z. Fang, X. Jiang, X. Tian, F. Zheng, M. Cheng, E. Zhao, W. Ye, Y. Qin, and Y. Zhang, Ultratransparent PMN-PT electro-optic ceramics and its application in optical communication. *Adv. Opt. Mater.*, **9**, 2002139 (2021).

[63] D. Berlincourt, Piezoelectric ceramic compositional development. *J. Acoust. Soc. Am.*, **91**, 3034-3040 (1992).

[64] N. Luo, S. Zhang, Q. Li, Q. Yan, Y. Zhang, T. Ansell, J. Luo, and T. R. Shrout, Crystallographic dependence of internal bias in domain engineered Mn-doped relaxor-$PbTiO_3$ single crystals. *J. Mater. Chem. C*, **4**, 4568-4576 (2016).

[65] N. P. Sherlock, S. Zhang, J. Luo, H. Y. Lee, T. R. Shrout, and R. J. Meyer Jr, Large signal electromechanical properties of low loss $(1-x)Pb(Mg_{1/3}Nb_{2/3})O_3-xPbTiO_3$ single crystals. *J. Appl. Phys.*, **107**, 074108 **(2010)**.

[66] M. B. Moffett, H. C. Robinson, J. M. Powers, and P. D. Baird, Single-crystal lead magnesium niobate-lead titanate (PMN/PT) as a broadband high power transduction material. *J. Acoust. Soc. Am.*, **121**, 2591-2599 (2007).

[67] S. Zhang, S. M. Lee, D. H. Kim, H. Y. Lee, and T. R. Shrout, Characterization of Mn-modified Pb($Mg_{1/3}Nb_{2/3}$)O_3-$PbZrO_3$-$PbTiO_3$ single crystals for high power broad bandwidth transducers. *Appl. Phys. Lett.*, **93**, 122908 (2008).

[68] J. Luo, W. Hackenberger, S. Zhang, and T. R. Shrout, A high Qm relaxor ferroelectric single crystal: growth and characterization. In *2010 IEEE International Ultrasonics Symposium*, pp. 68-71. IEEE, 2010.

[69] Y. H. Chen, K. Uchino, M. Shen, and D. Viehland, Substituent effects on the mechanical quality factor of Pb($Mg_{1/3}Nb_{2/3}$)O_3–$PbTiO_3$ and Pb($Sc_{1/2}Nb_{1/2}$)O_3–$PbTiO_3$ ceramics. *J. Appl. Phys.*, **90**, 1455-1458 (2001).

[70] S. Zhang, L. Lebrun, C. A. Randall, and T. R. Shrout, Orientation dependence properties of modified tetragonal 0.88Pb($Zn_{1/3}Nb_{2/3}$)O_3–0.12$PbTiO_3$ single crystals. *Phys. Status Solidi A*, **202**, 151-157 (2005).

[71] H. Qiao, C. He, Z. Wang, D. Pang, X. Li, Y. Liu, and X. Long, Influence of Mn dopants on the electrical properties of Pb($In_{0.5}Nb_{0.5}$)O_3–$PbTiO_3$ ferroelectric single crystals. *RSC Adv.*, **7**, 32607-32612 (2017).

[72] X. Huo, S. Zhang, G. Liu, R. Zhang, J. Luo, R. Sahul, W. Cao, T. R. Shrout, Complete set of elastic, dielectric, and piezoelectric constants of $[011]_C$ poled rhombohedral Pb($In_{0.5}Nb_{0.5}$)O_3-Pb($Mg_{1/3}Nb_{2/3}$)O_3-$PbTiO_3$:Mn single crystals. *J. Appl. Phys.*, **113**, 074106 (2013).

[73] L. Zheng, R. Sahul, S. Zhang, W. Jiang, S. Li, and W. Cao, Orientation dependence of piezoelectric properties and mechanical quality factors of 0.27Pb($In_{1/2}Nb_{1/2}$)O_3-0.46Pb($Mg_{1/3}Nb_{2/3}$)O_3-0.27$PbTiO_3$:Mn single crystals. *J. Appl. Phys.*, **114**, 104105 (2013).

[74] S. Zhang, R. Xia, L. Lebrun, D. Anderson, T. R. Shrout, Piezoelectric materials for high power, high temperature applications. *Mater. Lett.*, **59**, 3471-3475 (2005).

[75] E. Sun, R. Zhang, F. Wu, B. Yang, W. Cao, Influence of manganese doping to the full tensor properties of 0.24Pb($In_{1/2}Nb_{1/2}$)O_3-0.47Pb($Mg_{1/3}Nb_{2/3}$)O_3-0.29$PbTiO_3$ single crystals. *J. Appl. Phys.*, **113**, 074108 (2013).

[76] X. Huo, S. Zhang, G. Liu, R. Zhang, J. Luo, R. Sahul, W. Cao, and T. R. Shrout, Elastic, dielectric and piezoelectric characterization of single domain PIN-PMN-PT: Mn crystals. *J. Appl. Phys.*, **112**, 124113 (2012).

[77] E. Sun, S. Zhang, J. Luo, T. R. Shrout, W. Cao, Elastic, dielectric, and piezoelectric constants of $Pb(In_{1/2}Nb_{1/2})O_3–Pb(Mg_{1/3}Nb_{2/3})O_3–PbTiO_3$ single crystal poled along $[011]_c$. *Appl. Phys. Lett.*, **97**, 032902 (2010).

[78] S. Zhang, S. Taylor, F. Li, J. Luo, and R. J. Meyer Jr, Piezoelectric property of relaxor-$PbTiO_3$ crystals under uniaxial transverse stress. *Appl. Phys. Lett.*, **102**, 172902 (2013).

[79] L. Kong, G. Liu, S. Zhang, and H. Liu, The role of tetragonal side morphotropic phase boundary in modified relaxor-$PbTiO_3$ crystals for high power transducer applications. *J. Appl. Phys.*, **114**, 144106 (2013).

[80] G. Liu, S. Zhang, W. Jiang, and W. Cao, Losses in ferroelectric materials. *Mater. Sci. Eng. R Rep.*, **89**, 1-48 (2015).

[81] S. M. Rhim, M. C. Shin, S. G. Lee, Piezoelectric single crystals for medical ultrasonic transducers. In *Handbook of Advanced Dielectric, Piezoelectric and Ferroelectric Materials*, Ye, Z.G.; Woodhead Publishing: Cambridge, England, 2008; pp. 101-129.

[82] D. Viehland, J. F. Li, S. J. Jang, L. E. Cross, M. Wuttig, Glassy polarization behavior of relaxor ferroelectrics. *Phys. Rev. B*, **46**, 8013 (1992).

[83] G. H. Haertling, Ferroelectric ceramics: history and technology. *J. Am. Ceram. Soc.*, **82**, 797-818 (1999).

[84] X. Dai, A. DiGiovanni, and D. Viehland, Dielectric properties of tetragonal lanthanum modified lead zirconate titanate ceramics. *J. Appl. Phys.*, **74**, 3399-3405 (1993).

[85] G. A. Samara, The relaxational properties of compositionally disordered ABO_3 perovskites. *J. Condens. Matter Phys.*, **15**, R367 (2003).

[86] Y. Liu, Z. Ling, Z. Zhuo, High piezoelectricity of PLZT ceramics with strong frequency-dielectric dispersion below depolarization temperature. *J. Alloys Compd.*, **727**, 925-930 (2017).

[87] S. B. Seshadri, M. M. Nolan, G. Tutuncu, J. S. Forrester, E. Sapper, G. Esteves, T. Granzow, P. A. Thomas, J. C. Nino, T. Rojac, and J. L. Jones, Unexpectedly high piezoelectricity of Sm-doped lead zirconate titanate in the Curie point region. *Sci*. *Rep*. **2018**, *8*, 1-13.

[88] B. Gao, Z. Yao, D. Lai, Q. Guo, W. Pan, H. Hao, M. Cao, and H. Liu, Unexpectedly high piezoelectric response in Sm-doped PZT ceramics beyond the morphotropic phase boundary region. *J*. *Alloys Compd*., **836**, 155474 (2020).

[89] N. Kumar, A. Mishra, A. De, U. Shankar, and R. Ranjan, Factors contributing to the local polar-structural heterogeneity and ultrahigh piezoelectricity in Sm-modified $Pb(Mg_{1/3}Nb_{2/3})O_3$–$PbTiO_3$. *J*. *Phys*. *D*: *Appl*. *Phys*., **53**, 165302 (2020).

[90] Y. Li, M. Borbely, and A. Bell, The influence of oxygen vacancies on piezoelectricity in samarium-doped $Pb(Mg_{1/3}Nb_{2/3})O_3$-$PbTiO_3$ ceramics. *J*. *Am*. *Ceram*. *Soc*., **104**, 2678-2688 (2021).

[91] F. Li, D. Lin, Z. Chen, Z. Cheng, J. Wang, C. Li, Z. Xu, Q. Huang, X. Liao, L. Q. Chen, T. R Shrout, and S. Zhang, Ultrahigh piezoelectricity in ferroelectric ceramics by design. *Nat*. *Mater*., **17**, 349-354 (2018).

[92] Q. Guo, X. Meng, F. Li, F. Xia, P. Wang, X. Gao, J. Wu, H. Sun, H. Hao, H. Liu, and S. Zhang, Temperature-insensitive PMN-PZ-PT ferroelectric ceramics for actuator applications. *Acta Mater*., **211**, 116871 (2021).

[93] P. Wang, Q. Guo, F. Li, F. Xia, H. Hao, H. Sun, H. Liu, and S. Zhang, Modified $Pb(Mg_{1/3}Nb_{2/3})O_3$-$PbZrO_3$–$PbTiO_3$ ceramics with high piezoelectricity and temperature stability. *J*. *Am*. *Ceram*. *Soc*., **104**, 5127-5137 (2021).

[94] Q. Guo, F. Li, F. Xia, P. Wang, X. Gao, H. Hao, H. Liu, H. Sun, and Zhang, S. Piezoelectric ceramics with high piezoelectricity and broad temperature usage range. *J*. *Materiomics*, **7**, 683-692 (2021).

[95] Q. Guo, F. Li, F. Xia, X. Gao, P. Wang, H. Hao, H. Sun, H. Liu, and S. Zhang, High-performance Sm-doped $Pb(Mg_{1/3}Nb_{2/3})O_3$-$PbZrO_3$–$PbTiO_3$-based piezoceramics. *ACS Appl*. *Mater*. *Interfaces*, **11,** 43359-43367 (2019).

[96] F. Li, M. J. Cabral, B. Xu, Z. Cheng, E. C. Dickey, J. M. LeBeau, J. Wang, J. Luo, S. Taylor, W. Hackenberger, L. Bellaiche, Z. Xu, L.-Q. Chen, T. R. Shrout, and S. Zhang, Giant piezoelectricity of Sm-doped $Pb(Mg_{1/3}Nb_{2/3})O_3$-$PbTiO_3$ single crystals. *Science*, **364**, 264-268 (2019).

[97] C. Li, B. Xu, D. Lin, S. Zhang, L. Bellaiche, T. R. Shrout, and F. Li, Atomic-scale origin of ultrahigh piezoelectricity in samarium-doped PMN-PT ceramics. *Phys. Rev. B*, **101**, 140102 (2020).

[98] B. Srimathy, and J. Kumar, Effect of donor dopants on the properties of flux grown PZN-PT single crystals. *Appl. Phys. A*, **127**, 1-7 (2021).

[99] M. Davis, M. Budimir, D. Damjanovic, and N. Setter, Rotator and extender ferroelectrics: Importance of the shear coefficient to the piezoelectric properties of domain engineered crystals and ceramics, *J. Appl. Phys.*, **101**, 054112 (2007).

[100] J. Jin, K. K. Rajan, L. C. Lim, Properties of single domain $Pb(Zn_{1/3}Nb_{2/3})O_3$–(6–7)%$PbTiO_3$ single crystal. *Jpn. J. Appl. Phys.*, **45**, 8744 (2006).

[101] R. Zhang, B. Jiang, W. Cao, Orientation dependence of piezoelectric properties of single domain $0.67Pb(Mn_{1/3}Nb_{2/3})O_3$–$0.33PbTiO_3$ crystals. *Appl. Phys. Lett.*, **82**, 3737-3739 (2003).

[102] F. Li, S. Zhang, Z. Xu, X. Wei, J. Luo, and T. R. Shrout, Electromechanical properties of tetragonal $Pb(In_{1/2}Nb_{1/2})O_3$−$Pb(Mg_{1/3}Nb_{2/3})O_3$−$PbTiO_3$ ferroelectric crystals. *J. Appl. Phys.*, **107**, 054107 (2010).

[103] S. Zhang, G. Liu, W. Jiang, J. Luo, W. Cao, T. R. Shrout, Characterization of single domain $Pb(In_{0.5}Nb_{0.5})O_3$-$Pb(Mg_{1/3}Nb_{2/3})O_3$-$PbTiO_3$ crystals with monoclinic phase. *J. Appl. Phys.* **2011**, *110*, 064108.

[104] (152) E. Sun, X. Qi, W. Cao, R. Zhang, B. Yang, and L. Zhao, Electromechanical properties of orthorhombic $0.24Pb(In_{1/2}Nb_{1/2})O_3$–$0.43Pb(Mg_{1/3}Nb_{2/3})O_3$–$0.33PbTiO_3$ single-domain crystal. *Mater. Lett.*, **157**, 163-165 (2015).

[105] X. Liu, S. Zhang, J. Luo, T. R. Shrout, W. Cao, A complete set of material properties of single domain $0.26Pb(In_{1/2}Nb_{1/2})O_3$–$0.46Pb(Mg_{1/3}Nb_{2/3})O_3$–$0.28PbTiO_3$ single crystals. *Appl. Phys. Lett.*, **96**, 012907 (2010).

[106] H. Cao and H. Luo, Elastic, piezoelectric and dielectric properties of $Pb(Mg_{1/3}Nb_{2/3})O_3$ - 38%$PbTiO_3$ single crystal, *Ferroelectrics*., **274**, 309 (2002).

[107] D. Damijanovic, F. Brem, N. Setter, Crystal orientation dependence of the piezoelectric d_{33} coefficient in tetragonal $BaTiO_3$ as a function of temperature, *Appl. Phys. Lett.* **80**, 652 (2002).

[108] D. Damjanovic, M. Budmir, M. Davis, N. Setter, Monodomain versus polydomain piezoelectric response of $0.67Pb(Mg_{1/3}Nb_{2/3})O_3$-$0.33PbTiO_3$ single crystals along nonpolar directions, *Appl. Phys. Lett.* **83**, 3 (2003).

[109] D. A. Damjanovic, A morphotropic phase boundary system based on polarization rotation and polarization extension. *Appl. Phys. Lett.*, **97**, 062906 (2010).

[110] Han, P.; Yan, W.; Tian, J.; Huang, X.; Pan, H. Cut directions for the optimization of piezoelectric coefficients of lead magnesium niobate–lead titanate ferroelectric crystals. *Appl. Phys. Lett.* **2005**, *86*, 052902.

[111] H. Dammak, A.-E. Renault, P. Gaucher, M. P. Thi, and G. Calvarin, Origin of the giant piezoelectric properties in the [001] domain engineered relaxor single crystals, *Jpn. J. Appl. Phys.*, Part 1 **10**, 6477 (2003).

[112] E. Sun, W. Cao, W. Jiang, P. Han, Complete set of material properties of single domain $0.24Pb(In_{1/2}Nb_{1/2})O_3$-$0.49Pb(Mg_{1/3}Nb_{2/3})O_3$-$0.27PbTiO_3$ single crystal and the orientation effects. *Appl. Phys. Lett.*, *99*, 032901 (2011).

[113] Y. Jing, L. Zheng, W. Lü, Z. Xi, P. Zheng, J. Du, R. Zhang, Full tensor properties of single-domain tetragonal $0.63Pb(Mg_{1/3}Nb_{2/3})O_3$-$0.37PbTiO_3$ single crystal and their orientation dependence. *Phys. Status Solidi B*, **253**, 1994-2000 (2016).

[114] X. Liu, S. Zhang, J. Luo, T. R. Shrout, and W. Cao, Complete set of material constants of $Pb(In_{1/2}Nb_{1/2})O_3$–$Pb(Mg_{1/3}Nb_{2/3})O_3$–$PbTiO_3$ single crystal with morphotropic phase boundary composition. *J. Appl. Phys.*, **106**, 074112 (2009).

[115] Z. Luan, G. Jiang, J. Wang, D. Liu, B. Yang, F. Wu, The intrinsic and extrinsic contributions in [001] oriented $(1-x)Pb(Mg_{1/3}Nb_{2/3})O_3$-$xPbTiO_3$ crystals. *Ferroelectrics*, **548**, 26-33 (2019).

[116] M. J. Haun, E. Furman, S. J. Jang, H. A. McKinstry, L. E. Cross, Thermodynamic theory of $PbTiO_3$. *J. Appl. Phys.*, **62**, 3331-3338 (1987).

[117] M. Zgonik, P. Bernasconi, M. Duelli, R. Schlesser, P. Günter, M. H. Garrett, D. Rytz, Y. Zhu, X. Wu, Dielectric, elastic, piezoelectric, electro-optic, and elasto-optic tensors of $BaTiO_3$ crystals. *Phys. Rev. B*, **50**, 5941 (1994).

[118] S. Zhang, N. P. Sherlock, R. J. Meyer Jr, and T. R. Shrout, Crystallographic dependence of loss in domain engineered relaxor-PT single crystals. *Appl. Phys. Lett.*, **94**, 162906 (2009).

[119] F. Li, L. Jin, Z. Xu, D. Wang, and S. Zhang, Electrostrictive effect in $Pb(Mg_{1/3}Nb_{2/3})O_3$-$xPbTiO_3$ crystals. *Appl. Phys. Lett.*, **102**, 152910 (2013).

[120] F. Li, L. Jin, Z. Xu, and S. Zhang, Electrostrictive effect in ferroelectrics: An alternative approach to improve piezoelectricity. *Appl. Phys. Rev.*, **1**, 011103 (2014).

[121] F. Li, S. Zhang, Z. Xu, X. Wei, J. Luo, and T. R. Shrout, Temperature independent shear piezoelectric response in relaxor-$PbTiO_3$ based crystals. *Appl. Phys. Lett.*, **97**, 252903 (2010).

[122] S. Zhang, F. Li, J. Luo, R. Xia, W. Hackenberger, T. R. Shrout, Investigation of single and multidomain $Pb(In_{0.5}Nb_{0.5})O_3$–$Pb(Mg_{1/3}Nb_{2/3})O_3$–$PbTiO_3$ crystals with mm 2 symmetry. *Appl. Phys. Lett.*, **97**, 132903 (2010).

[123] S. Zhang, L. Laurent, S. Liu, S. Rhee, C. A. Randall, T. R. Shrout, Piezoelectric shear coefficients of $Pb(Zn_{1/3}Nb_{2/3})O_3$–$PbTiO_3$ single crystals. *Jpn. J. Appl. Phys.*, **41**, L1099 (2002).

[124] S. Zhang, W. Jiang, R. J. Meyer Jr, F. Li, J. Luo, W. Cao, Measurements of face shear properties in relaxor-$PbTiO_3$ single crystals. *J. Appl. Phys.*, 110, 064106 (2011).

[125] 171 S. Zhang, F. Li, W. Jiang, J. Luo, R. J. Meyer Jr, W. Cao, and T. R. Shrout, Face shear piezoelectric properties of relaxor-$PbTiO_3$ single crystals. *Appl. Phys. Lett.*, **98**, 182903 (2011).

[126] Y. Zhou, Q. Li, C. Xu, F. Zhuo, D. Liu, Q. Yan, Y. Zhang, X. Chu, Anisotropic temperature–electric field phase diagrams and domain structure evolution in rhombohedral Mn-doped PIN–PMN–PT single crystals. *CrystEngComm*, **20**, 5169-5179 (2018).

[127] H. Fang, L. Wang, W. Kuai, J. Du, G. Jiang, X. Lu, M. Zhao, C. Wang, W. Su, L. Zheng, C. Wang, and C. Wang, Reversible and irreversible domain wall dynamics in $[011]_C$ oriented relaxor ferroelectric single crystals. *J. Am. Ceram. Soc.*, **103**, 3257-3264 (2020).

[128] Y. Zhou, Q. Li, F. Zhuo, C. Xu, Q. Yan, Y. Zhang, X. Chu, Domain switching and polarization fatigue in rhombohedral PIN-PMN-PT and Mn-doped PIN-PMN-PT single crystals. *J. Am. Ceram. Soc.*, **102**, 6668-6679 (2019).

[129] A. Thakre, A. Kumar, D. Y. Jeong, G. T. Hwang, W. H. Yoon, H. Y. Lee, J. Ryu, Enhanced mechanical quality factor of 32 mode Mn doped $71Pb(Mg_{1/3}Nb_{2/3})O_3$–$29PbZrTiO_3$ piezoelectric single crystals. *Electron. Mater. Lett.*, **16**, 156-163 (2020).

[130] N. P. Sherlock, L. M. Garten, S. J. Zhang, T. R. Shrout, R. J. Meyer Jr, Nonlinear dielectric response in piezoelectric materials for underwater transducers. *J. Appl. Phys.*, **112**, 124108 (2012).

[131] L. Zheng, L. Yang, Y. Li, X. Lu, D. Huo, W. Lü, R. Zhang, B. Yang, W. Cao, Origin of improvement in mechanical quality factor in acceptor-doped relaxor-based ferroelectric single crystals. *Phys. Rev. Appl.*, **9**, 064028 (2018).

[132] Y. Jing, L. Zheng, F. Liu, X. Qi, G. Jiang, J. Fan, G. Liu, W. Lü, A large and anisotropic enhancement of the mechanical quality factor in ternary relaxor-$PbTiO_3$ single crystals. *Appl. Phys. Lett.*, 118, 182902 (2021).

[133] N. P. Sherlock, Relaxor-PT single crystals for broad bandwidth, high power sonar projectors. Doctral dissertaiton, The Pennsylvania State University, University Park, Pennsylvania, United States, 2010.

[134] R. J. Meyer, T. C. Montgomery, and W. J. Hughes, Tonpilz transducers designed using single crystal piezoelectrics. In 2002 *OCEANS'02 MTS/IEEE, 4,* pp. 2328-2333.

[135] S. C. Thompson, R. J. Meyer, and D. C. Markley, Performance of tonpilz transducers with segmented piezoelectric stacks using materials with high electromechanical coupling coefficient. *J. Acoust. Soc. Am.*, **135**, 155-164 (2014).

[136] K. Zhang, D. Huang, B. R. Chen, and Y. Z. Tang, Wideband single crystal longitudinal transducer for underwater sound. In 2019 14th Symposium on Piezoelectricity, Acoustic Waves and Device Applications (SPAWDA), Shijiazhuang, China, pp. 1-3. IEEE.

[137] N. P. Sherlock, and R. J. Meyer, Modified single crystals for high-power underwater projectors. *IEEE Trans. Ultrason. Ferroelectr. Freq. Control*, **59**, 1285-1291 (2012).

[138] R. Guo, S. Li, D. An, T. Han, J. Chen, and W. Cao, Comprehensive analysis of Mn:PIN-PMN-PT single crystals for Class IV flextensional transducer. *Ceram. Int.*, **44**, 2864-2868 (2018).

[139] Q. Zhou, K. H. Lam, H. Zheng, W. Qiu, and K. K. Shung, Piezoelectric single crystal ultrasonic transducers for biomedical applications. *Prog. Mater. Sci.*, **66**, 87-111 (2014).

[140] H. J. Lee, S. Zhang, Y. Bar-Cohen, and S. Sherrit, High temperature, high power piezoelectric composite transducers. *Sensor***,** **14**, 14526-14552 (2014).

[141] Q. Zhou, D. Wu, J. Jin, C. H. Hu, X. Xu, J. Williams, J. M. Cannata, L. Lim, and K. K. Shung, Design and fabrication of PZN-7%PT single crystal high frequency angled needle ultrasound transducers. *IEEE Trans. Ultrason. Ferroelectr. Freq. Control*, **55**, 1394-1399 (2008).

[142] Q. Zhou, X. Xu, E. J. Gottlieb, L. Sun, J. M. Cannata, H. Ameri, M. S. Humayun, P. Han, and K. K. Shung, PMN-PT single crystal, high-frequency ultrasonic needle transducers for pulsed-wave Doppler application. *IEEE Trans. Ultrason. Ferroelectr. Freq. Control*, **54**, 668-675 (2007).

[143] K. K. Shung, J. M. Cannata, and Q. F. Zhou, Piezoelectric materials for high frequency medical imaging applications: A review. *J. Electroceram.*, **19**, 141–147 (2007).

[144] K. H. Lam, Y. Chen, K. F. Cheung, and J. Y. Dai, PMN–PT single crystal focusing transducer fabricated using a mechanical dimpling technique. *Ultrasonics*, **52**, 20-24 (2012).

[145] Y. Chen, K. H. Lam, D. Zhou, W. F. Cheng, J. Y. Dai, H. S. Luo, and H. L. W. Chan, High frequency PMN–PT single crystal focusing transducer fabricated by a mechanical dimpling technique. *Ultrasonics*, **53**, 345-349 (2013).

[146] Y. Chen, W. B. Qiu, K. H. Lam, B. Q. Liu, X. P. Jiang, H. R. Zheng, H. S. Luo, H. L. W. Chan, and J. Y. Dai, Focused intravascular ultrasonic probe using dimpled transducer elements. *Ultrasonics*, **56**, 227-231 (2015).

[147] C. Fei, Y. Yang, F. Guo, P. Lin, Q. Chen, Q. Zhou, and L. Sun, PMN-PT single crystal ultrasonic transducer with half-concave geometric design for IVUS imaging. *IEEE Trans*. *Biomed*. *Eng*., **65**, 2087-2092 (2017).

[148] H. J. Lee, S. Zhang, R. J. Meyer Jr, N. P. Sherlock, and T. R. Shrout, Characterization of piezoelectric ceramics and 1-3 composites for high power transducers. *Appl*. *Phys*. *Lett*., **101**, 032902 (2012).

[149] H. J. Lee, and S. Zhang, Design of low-loss 1-3 piezoelectric composites for high-power transducer applications. *IEEE Trans. Ultrason. Ferroelectr. Freq. Control* **2012**, *59*, 1969-1975.

[150] C. M. Wong, Y. Chen, H. Luo, J. Dai, K. H. Lam, and H. L. W. Chan, Development of a 20-MHz wide-bandwidth PMN-PT single crystal phased-array ultrasound transducer. *Ultrasonics*, **73**, 181-186 (2017).

[151] D. Zhou, J. Chen, and H. Luo, Piezoelectric single crystals of $Pb(Mg_{1/3}Nb_{2/3})O_3$-$PbTiO_3$ and their applications in medical ultrasonic transducers. In 2008 International Conference on BioMedical Engineering and Informatics, *2*, pp. 662-666. IEEE.

[152] D. Zhou, K. F. Cheung, Y. Chen, S. T. Lau, Q. Zhou, K. K. Shung, H. S. Luo, J. Dai, and H. L. W. Chan, Fabrication and performance of endoscopic ultrasound radial arrays based on PMN-PT single crystal/epoxy 1-3 composite. *IEEE Trans. Ultrason. Ferroelectr. Freq. Control*, **58**, 477-484 (2011).

[153] S. T. Lau, H. Li, K. S. Wong, Q. F. Zhou, D. Zhou, Y. C. Li, H. C. Luo, K. K. Shung, and J. Y. Dai, Multiple matching scheme for broadband $0.72Pb(Mg_{1/3}Nb_{2/3})O_3{-}0.28PbTiO_3$ single crystal phased-array transducer. *J*. *Appl*. *Phys*., **105**, 094908 (2009).

[154] J. Wang, M. Chen, X. Zhao, F. Wang, Y. Tang, D. Lin, and H. Luo, Fabrication and high acoustic performance of high frequency needle ultrasound transducer with PMN-PT/Epoxy 1-3 piezoelectric composite prepared by dice and fill method. *Sens*. *Actuator A Phys*., **318**, 112528 (2021).

[155] X. Yang, Z. Li, C. Fei, Y. Liu, D. Li, S. Hou, L. Zhang, F. Li, Y. Yang, Q. Zhou, and Z. Xu, High frequency needle ultrasonic transducers based on Mn doped piezoelectric single crystal. *J. Alloys Compd.*, **832**, 154951 (2020).

[156] H. J. Lee, S. Zhang, J. Luo, F. Li, and T. R. Shrout, Thickness-dependent properties of relaxor-$PbTiO_3$ ferroelectrics for ultrasonic transducers. *Adv. Funct. Mater.*, **20**, 3154-3162 (2010).

[157] H. J. Lee, S. Zhang, and T. R. Shrout, Scaling effects of relaxor-$PbTiO_3$ crystals and composites for high frequency ultrasound. *J. Appl. Phys.*, **107**, 124107 (2010).

[158] H. Wan H. Kim, H. Wu, C. Luo, and X. Jiang, Characterization of high-frequency ultrasound transducers made of alternating current poled $Pb(Mg_{1/3}Nb_{2/3})O_3$-$xPbTiO_3$ single crystals. In 2020 IEEE International Ultrasonics Symposium (IUS), pp. 1-4. IEEE.

[159] J. Xu, Z. Zhang, S. Liu, J. Xiao, Q. Yue, H. Deng, X. Wang, D. Lin, F. Wang, R. Zhang, and X. Li, Optimizing the piezoelectric vibration of $Pb(Mg_{1/3}Nb_{2/3})O_3$-$0.25PbTiO_3$ single crystal by alternating current polarization for ultrasonic transducer. *Appl. Phys. Lett.*, **116**, 202903 (2020).

[160] C. Qiu, J. Liu, F. Li, and Z. Xu, Thickness dependence of dielectric and piezoelectric properties for alternating current electric-field-poled relaxor-$PbTiO_3$ crystals. *J. Appl. Phys.*, **125**, 014102 (2019).

[161] K. Uchino, Electro-optic ceramics and their display applications. *Ceram. Int.*, **21**, 309-315 (1995).

[162] L. Zheng, Y. Jing, X. Lu, S. Li, L. Yang, W. Lü, and W. Cao, Temperature dependent piezoelectric anisotropy in tetragonal $0.63Pb(Mg_{1/3}Nb_{2/3})$-$0.37PbTiO_3$ single crystal. *Appl. Phys. Lett.*, **113**, 102903 (2018).

[163] F. Li, S. Zhang, D. Lin, J. Luo, Z. Xu, X. Wei, and T. R. Shrout, Electromechanical properties of $Pb(In_{1/2}Nb_{1/2})O_3$–$Pb(Mg_{1/3}Nb_{2/3})O_3$–$PbTiO_3$ single crystals. *J. Appl. Phys.*, **109**, 014108 (2011).

[164] D. Lin, H. J. Lee, S. Zhang, F. Li, Z. Li, Z. Xu, and T. R. Shrout, Influence of domain size on the scaling effects $Pb(Mg_{1/3}Nb_{2/3})O_3$-$PbTiO_3$ ferroelectric crystals. *Scr. Mater.*, **64**, 1149–1151 (2011).

[165] F. Li, S. Zhang, J. Luo, X. Geng, Z. Xu, and T. R. Shrout, [111]-oriented PIN-PMN-PT crystals with ultrahigh dielectric permittivity and high frequency constant for high-frequency transducer applications. *J. Appl. Phys.*, **120**, 074105 (2016).

[166] L. Lebrun, G. Sebald, B. Guiffard, C. Richard, D. Guyomar, and E. Pleska, Investigations on ferroelectric PMN–PT and PZN–PT single crystals ability for power or resonant actuators. *Ultrasonics*, **42**, 501-505 (2004).

[167] X. Y. Hou, H. P. Lee, S. P. Lim, and C. J. Ong, Performance enhancement of ultrasonic motors using single crystalline piezo-materials. In *2012 Digest APMRC*, pp. 1-2. IEEE.

[168] S. Li, W. Jiang, L. Zheng, and W. Cao, A face-shear mode single crystal ultrasonic motor. *Appl. Phys. Lett.*, **102**, 183512 (2013).

[169] P. Ci, G. Liu, Z. Chen, S. Zhang, and S. Dong, High-order face-shear modes of relaxor-$PbTiO_3$ crystals for piezoelectric motor applications. *Appl. Phys. Lett.*, **104**, 242911 (2014).

[170] W. Ou, S. Li, W. Cao, and M. Yang, A single-mode Mn-doped 0.27PIN-0.46PMN-0.27PT single-crystal ultrasonic motor. *J. Electroceramics*, **37**, 121-126 (2016).

[171] P. W. Bridgman, Certain physical properties of single crystals of tungsten, antimony, bismuth, tellurium, cadmium, zinc, and tin , *Proc. Am. Acad. Arts Sci.* 60, 305 (1925).

[172] D. C. Stockbarger, The production of large single crystals of lithium fluoride, *Rev. Sci. Instrum.* 7, 133 (1936).

[172] H. Luo, G. Xu, P. Wang, and Z. Yin, Growth and characterization of relaxor ferroelectric PMNT single crystals. *Ferroelectrics* **231,** 97-102 (1999).

[173] S. Zhang, J. Luo, W. Hackenberger, and T. R. Shrout, Characterization of $Pb(In_{1/2}Nb_{1/2})O_3$–$Pb(Mg_{1/3}Nb_{2/3})O_3$–$PbTiO_3$ ferroelectric crystal with enhanced phase transition temperatures. *J. Appl. Phys.*, **104**, 064106 (2008).

[174] G. Xu, K. Chen, D. Yang, and J. Li, Growth and electrical properties of large size $Pb(In_{1/2}Nb_{1/2})O_3$-$Pb(Mg_{1/3}Nb_{2/3})O_3$-$PbTiO_3$ crystals prepared by the vertical Bridgman technique. *Appl. Phys. Lett.*, **90**, 032901 (2007).

[175] P. Han, J. Tian, and W. Yan, Bridgman growth and properties of PMN-PT-based single crystals. In *Handbook of Advanced Dielectric, Piezoelectric and Ferroelectric Materials: Synthesis, Properties and Applications*; Ye, Z.G., Ed.; Woodhead: Cambridge, UK, 2008; pp. 3–37.

[176] W. Hackenberger, J. Luo, X. N. Jiang, K. A. Snook, P. W. Rehrig, S. J. Zhang, and T. R. Shrout, Recent developments and applications of piezoelectric crystals. In *Handbook of Advanced Dielectric, Piezoelectric and Ferroelectric Materials–Synthesis, Characterization and Applications*; Ye, Z.G., Ed.; Woodhead: Cambridge, UK, 2008; pp. 73–100.

[177] J. Luo, and S. Zhang, Advances in the growth and characterization of relaxor-PT-based ferroelectric single crystals. *Crystals*, **4**, 306–330 (2014).

[178] H. Luo, G. Xu, H. Xu, P. Wang, and Z. Yin, Compositional homogeneity and electrical properties of lead magnesium niobate titanate single crystals grown by a modified Bridgman technique. *Jpn. J. Appl. Phys.***,** 39, 5581 (2000).

[179] K. T. Zawilski, M. C. C. Custodio, R. C. DeMattei, S. G. Lee, R. G. Monteiro, H. Odagawa, and R. S. Feigelson, Segregation during the vertical Bridgman growth of lead magnesium niobate–lead titanate single crystals. *J. Cryst. Growth*, 258, 353–367 (2003).

[180] W. Zhang, Z. Wang, X. Yang, X. Long, C. He, Composition uniformity of $Pb(In_{1/2}Nb_{1/2})O_3$-Pb $(Mg_{1/3}Nb_{2/3})O_3$-$PbTiO_3$ single crystals grown in ⟨001⟩ direction. *J. Cryst. Growth*, **560**, 126061 (2021).

[181] S. L. Swartz, and T. R. Shrout, Fabrication of perovskite lead magnesium niobate. *Mater. Res. Bull.*, **17**, 1245–1250 (1982).

[182] F. Liao, Y. Zhao, Z. Chen, Y. Zheng, and H Chen, Bridgman growth and photoelectronic property of relaxor-based ferroelectric single crystal $Pb(Sm_{1/2}Nb_{1/2})O_3$-$Pb(Mg_{1/3}Nb_{2/3})O_3$-$PbTiO_3$, *Crystals*, **11**, 402 (2021).

[183] S. J. Zhang, J. Luo, and T. R. Shrout, T High-performance, high-T_C piezoelectric crystals, In *Handbook of Advanced Dielectric, Piezoelectric and Ferroelectric Materials*; Ye, Z.G., Ed.; Woodhead: Cambridge, UK, 2008; pp. 130–151.

[184] Y. J. Yamashita and Y. Hosono, High Curie temperature piezoelectric single crystals of the $Pb(In_{1/2}Nb_{1/2})O_3$–$Pb(Mg_{1/3}Nb_{2/3})O_3$–$PbTiO_3$ ternary materials system, *Handbook of Advanced Dielectric, Piezoelectric and Ferroelectric Materials*; Ye, Z.G., Ed.; Woodhead: Cambridge, UK, 2008; pp. 205–229.

[185] T. Liu and C. S. Lynch, Energy analysis of field-induced phase transitions in relaxor-based piezo- and ferroelectric crystals, *Handbook of Advanced Dielectric, Piezoelectric and Ferroelectric Materials*; Ye, Z.G., Ed.; Woodhead: Cambridge, UK, 2008; pp. 366–383.

[186] J. M. Kiat and B. Dkhil, From the structure of relaxors to the structure of MPB systems, *Handbook of Advanced Dielectric, Piezoelectric and Ferroelectric Materials*; Ye, Z.G., Ed.; Woodhead: Cambridge, UK, 2008; pp. 391–440.

[187] S. Shimanuki, S. Saito, and Y. Yamashita, Single crystal of the $Pb(Zn_{1/3}Nb_{2/3})O_3$–$PbTiO_3$ system grown by the vertical Bridgeman method and its characterization. *Jpn. J. Appl. Phys.*, **37**, 3382 (1998).

[188] W. Cao, Full-set material properties and domain engineering principles of ferroelectric single crystals. In *Handbook of Advanced Dielectric, Piezoelectric and Ferroelectric Materials*; Ye, Z.G., Ed.; Woodhead: Cambridge, UK, 2008; pp. 2358–265.

[189] K. Song, Z. Li, H. Guo, Z. Xu, S. Fan, Compositional segregation and electrical properties characterization of [001]-and [011]-oriented co-growth $Pb(In_{1/2}Nb_{1/2})O_3$-$Pb(Mg_{1/3}Nb_{2/3})O_3$-$PbTiO_3$ single crystal. *J. Appl. Phys.*, **123**, 154107 (2018).

[190] K. T. Zawilski, R. C. DeMattei, and R. S. Feigelson, Zone levelling of lead magnesium niobate–lead titanate crystals using RF heating. *J. Cryst. Growth*, **277**, 393–400 (2005).

[191] K. Echizenya, and M. Matsushita, Continuous feed growth and characterization of PMN-PT single crystals. In Proceedings of the 2011 IEEE International Ultrasonics Symposium, Orlando, FL, USA, 18–21 October 2011; pp. 1813–1816.

[192] M. Matsushitata, and K. Echizenya, Continuous feeding growth of ternary PIN-PMN-PT single crystals. In Proceedings of the 2014 Joint IEEE International Symposium on the Applications of Ferroelectric, International Workshop on Acoustic Transduction Materials and Devices & Workshop on Piezoresponse Force Microscopy, University Park, PA, USA, 12–16 May 2014; pp. 1–4.

[193] K. Echizenya, K. Nakamura, and K. Mizuno, PMN-PT and PIN-PMN-PT single crystals grown by continuous-feeding Bridgman method. *J. Cryst. Growth*, **531**, 125364 (2020).

[194] Z. Li, K. Song, H. Guo, Y. Liu, M. Ma, S. Fan, and Z. Xu, High composition uniformity of 4″ of PIN-PMN-PT single crystals grown by the modified Bridgman method. *J. Cryst. Growth*, **468**, 331–334 (2017).

[195] K. Song, Q. Li, H. Guo, Q. Hu, Z. Li, F. Li, S. Fan, and Z. Xu, Composition and electrical properties characterization of a 5″ diameter PIN-PMN-PT single crystal by the modified Bridgman method. *J. Alloys Compd*., **851**, 156145 (2021).

[196] H. Y. Lee, Development of high-performance piezoelectric single crystals by using solid-state single crystal growth (SSCG) method. In *Handbook of Advanced Dielectric, Piezoelectric and Ferroelectric Materials*; Ye, Z.G., Ed.; Woodhead: Cambridge, UK, 2008; pp. 158–172.

[197] P. Kabakov, C. Dean, V. Kurusingal, Z. Cheng, H. Y. Lee, and S. Zhang, S. Solid-state crystal growth of lead-free ferroelectrics. *J. Mater. Chem. C*, **8**, 7606–7649 (2020).

[198] S. Zhang, S. M. Lee, D. H. Kim, H. Y. Lee, and T. R. Shrout, T.R. Electromechanical properties of PMN–PZT piezoelectric single crystals near morphotropic phase boundary compositions. *J. Am. Ceram. Soc*., **90**, 3859–3862 (2007).

[199] S. J. L. Kang, J. H. Park, S. Y. Ko, and H. Y. Lee, Solid-state conversion of single crystals: The principle and the state-of-the-art. *J. Am. Ceram. Soc*., **98**, 347–360 (2015).

[200] S. J. L. Kang, S. Y. Ko, and S. Y. Moon, Mixed control of boundary migration and the principle of microstructural evolution. *J. Ceram. Soc. Jpn*., **124,** 259–267 (2016).

[201] T. Yamamoto, and T. Sakuma, Fabrication of barium titanate single crystals by solid-state grain growth. *J. Am. Ceram. Soc*., **77**, 1107–1109 (1994).

[202] Y. S. Yoo, M. K. Kang, J. H. Han, H. Kim, and D. Y. Kim, Fabrication of $BaTiO_3$ single crystals by using the exaggerated grain growth method. *J. Eur. Ceram. Soc*., **17**, 1725–1727 (1997).

[203] P. W. Rehrig, G. L. Messing, and S. Trolier-McKinstry, Templated grain growth of barium titanate single crystals. *J. Am. Ceram. Soc*., **83**, 2654–2660 (2000).

[204] H. Y. Lee, J. S. Kim, and D. Y. Kim, Fabrication of $BaTiO_3$ single crystals using secondary abnormal grain growth. *J. Eur. Ceram. Soc*., **20**, 1595–1597 (2000).

[205] T. Li, A. M. Scotch, H. M. Chan, M. P. Harmer, S. E. Park, T. R. Shrout, and J. R. Michael, Single crystals of $Pb(Mg_{1/3}Nb_{2/3})O_3$—35mol%$PbTiO_3$ from polycrystalline precursors. *J. Am. Ceram. Soc.*, **81**, 244–248 (1998).

[206] E. M. Sabolsky, A. R. James, S. Kwon, S. Trolier-McKinstry, and G. L. Messing, Piezoelectric properties of ⟨001⟩ textured $Pb(Mg_{1/3}Nb_{2/3})O_3$–$PbTiO_3$ ceramics, *Appl. Phys. Lett.* **78**, 2551 (2001).

[207] C. J. Stringer, and C. A. Randall, In situ tem investigations of the high-temperature relaxor ferroelectric BiScO3–$Pb(Mg_{1/3}Nb_{2/3})O_3$–$PbTiO_3$ ternary solid solution, *J. Am. Ceram. Soc.*, **90**, 1802-1807 (2007).

[208] Z. Chen, X. Liao, J. Chen, and S. Zhang, The visible hand behind properties. *Microstructures*, **1**, 2021001 (2021).

[209] M. S. Kim, J. G. Fisher, S. J. L. Kang, and H. Y. Lee, Grain growth control and solid-state crystal growth by Li_2O/PbO addition and dislocation introduction in the PMN-35PT system. *J. Am. Ceram. Soc.*, **89**, 1237–1243 (2006).

[210] J. B. Lim, S. Zhang, H. Y. Lee, T. R. Shrout, Solid state crystal growth of $BiScO_3$-$Pb(Mg_{1/3}Nb_{2/3})O_3$-$PbTiO_3$. *J. Electroceramics*, **29**, 139–143 (2012).

[211] P. T. King, E. P. Gorzkowski, A. M. Scotch, D. J. Rockosi, H. M. Chan, and M. P. Harmer, Kinetics of {001} $Pb(Mg_{1/3}Nb_{2/3})O_3$–35mol%$PbTiO_3$ single crystals grown by seeded polycrystal conversion. *J. Am. Ceram. Soc.*, **86**, 2182–2187 (2003).

[212] S. Zhang, S. M. Lee, D. H. Kim, H. Lee, and T.R. Shrout, Characterization of high T_C $Pb(Mg_{1/3}Nb_{2/3})O_3$-$PbZrO_3$-$PbTiO_3$ single crystals fabricated by solid state crystal growth. *Appl. Phys. Lett.*, **90**, 232911 (2007).

[213] A. Khan, F. A. Meschke, T. Li, A. M. Scotch, H. M. Chan, and M. P. Harmer, Growth of $Pb(Mg_{1/3}Nb_{2/3})O_3$-35mol% $PbTiO_3$ single crystals from (111) substrates by seeded polycrystal conversion. *J. Am. Ceram. Soc.*, **82**, 2958–2962 (1999).

[214] A. Khan, E. P. Gorzkowski, A. M. Scotch, E. R. Leite, T. Li, H. M. Chan, and M. P. Harmer, Influence of excess PbO additions on {111} single-grystal growth of $Pb(Mg_{1/3}Nb_{2/3})O_3$-35mol%$PbTiO_3$ by seeded polycrystal conversion. *J. Am. Ceram. Soc.*, **86**, 2176–2181 (2003).

[215] S. Zhang, S. M. Lee, D. H. Kim, H. Y. Lee, and T. R. Shrout, Elastic, piezoelectric, and dielectric properties of $0.71Pb(Mg_{1/3}Nb_{2/3})O_3$-$0.29PbTiO_3$ crystals obtained by solid-state crystal growth. *J. Am. Ceram. Soc.*, **91**, 683–686 (2008).

Chapter 4. Sample preparation and characterization techniques

This chapter discusses the results of ceramic sample preparation. Using a pre-synthesized ceramic sample is an efficient way of fabricating pyrochlore-free high-quality single crystals [1-4]. Therefore, prior to single crystal growth, ceramic samples were prepared, and then their properties were compared to other references. Based on this property study, ceramic samples for single crystals were prepared. This chapter also discusses the characterization techniques that were used for property confirmation.

4.1 Material Characterization Techniques

The prepared ceramic samples were characterised using the following techniques:

4.1.1 Dielectric measurements

The principle of dielectric measurement is that a series capacitor measures the capacitance of the sample in the Sawyer-Tower circuit. The dielectric constant is calculated from this measurement by the following equation:

$$C = \frac{\varepsilon\, \varepsilon_0\, A}{t}, \tag{4.1}$$

where C is the capacitance of the sample, A is sample area with applied electrode, t is the thickness, ε is the relative permittivity, and ε_0 is the permittivity of free space (8.8514×10^{-12} F/m).

Measuring the temperature dependence of the dielectric constant is an effective way of studying the dielectric property of piezoelectric material. In this method, the capacitance and dielectric loss tangent are directly measured. Using Equation (4.1), the dielectric constant is calculated. This method is also able to provide the values of other important properties including the dielectric loss tangent, and the phase transition and the Curie temperatures (T_C). The measurement is performed within a wide range of temperature and at a range of frequency. In this work, the temperature dependence of the dielectric constant is measured using two dielectric measurement systems (PK-CPT1504, PolyK Tech., USA and TZDM-RT-800, Harbin Julang Tech., China). A cryocooler and a computer-controlled oven (-150 °C–

200 °C and room temperature to 800 °C, respectively) and an inductance-capacitance-resistance (LCR) meter (4980AL, Keysight, USA) were also employed. The heating rate was set as ±2.0 °C during the capacitance and loss measurements. For ceramic samples, the 100 Hz to 1 MHz frequency range was applied

4.1.2 Measurement of piezoelectricity

Several methods are used to measure piezoelectric coefficients. The Berlincourt d_{33} method is a "quasi-static" way of measuring the longitudinal piezoelectric coefficient. Using this method, d_{31} and d_{15} can also be measured with a specific adaptor. The operation is simple and gives a quick result. Such measurements could possibly lead to errors, however, the sources of which are derived from mismatch between the sample and the device sensor and non-standard geometry of the sample.

Longitudinal and lateral piezoelectric coefficients are also obtained from measurements of strain induced by electric field (S-E curve), determined by $d = \Delta S/\Delta E$. Using this method, d_{33}, d_{31}, and d_{32} can be determined. With this method, a field induced ferroelectric-to-ferroelectric phase transition could occur under high electric field. Only low field could therefore be used in this method. In this thesis work, a TF Analyser 2000 (aicACCT Systems GmbH, Aachen, Germany) was used to measure the uniaxial strain look at 1 Hz and up to 20 kV/cm. The high-field d^*_{33} was calculated at varying electric fields by calculating the slope of the strain versus the applied E.

In this work, piezoelectric coefficients of ceramic samples were measured using the Berlincourt method.

4.1.3 X-ray Diffraction (XRD)

To characterise the composition and phase of samples, we used XRD measurements. Bragg's law is expressed as follows:

$$2d_{hkl}sin\theta = n\lambda \qquad (4.2)$$

Here, d is the interplanar spacing of the indicated set of lattice planes, θ is the angle of incidence of the X-ray, λ is the wavelength of the X-rays, and n is an integer. When Bragg's law is satisfied, the diffracted X-rays constructively interfere and can be determined. From the obtained diffraction pattern, it is possible to detect different phases in a material.

In this work, we used a GBC MMA diffractometer or a PANalytical Empyrean X-ray diffraction goniometer, both with Kα radiation, where the wavelength is 1.540562 Å.

4.2 Ceramic sample preparation

For high-quality single crystal growth, high purity powders of raw materials could be used. Using a pre-synthesized ceramic sample is an efficient way of growing pyrochlore-free single crystal [3-5]. For this purpose, the ceramic materials were prepared prior to the single crystal growth and their properties were controlled. The following sections describe the method for ceramic sample preparation.

4.2.1. Two-step Columbite method

Ceramic samples were prepared using the two-step Columbite method [2]. This method was discovered to be suitable for the synthesis of pyrochlore-free PMN ceramic material. In this method, the precursor $MgNb_2O_6$ is, in advance, synthesized from MgO and Nb_2O_5 oxides in order to avoid parasitic phases that could be produced by the easy reaction between PbO and Nb_2O_5 oxides.

$MgNbO_6$ is the product of the following high temperature reaction:

$$MgO + N_2O_5 \rightarrow MgNb_2O_6 \qquad (4.3)$$

Thereafter, the synthesized $MgNbO_6$ is mixed with lead oxide and then calcined at a high temperature. $MgNb_2O_6$ reacts with PbO to form $Pb(Mg_{1/3}Nb_{2/3})O_3$ as expressed by the following formula:

$$1/3MgNb_2O_6 + PbO \rightarrow Pb(Mg_{1/3}Nb_{2/3})O_3 \qquad (4.4)$$

In this work, both this synthesized $MgNb_2O_6$ and commercially available $MgNb_2O_6$ material were used. **Table 4.1** shows the list of high-purity materials that were used for this thesis work.

4.2.1.1 Synthesis of precursor $MgNb_2O_6$

MgO and Nb_2O_5 oxides are stoichiometrically weighed and batched in a polytetrafluoroethylene (PTFE) milling jar. An excess of MgO ensures that pyrochlore-free perovskite phase will be formed in ceramic material [6-12], while an excess of MgO helps the completion of reaction between MgO and Nb_2O_5 [7] and improves the grain size [7,8,12]. In this work, 2 wt% MgO excess was added to the batch.

99% ethanol and yttrium stabilized zirconia balls 5 mm in diameter were also added to the jar as milling media. Here, the volume ratio of the powder to the milling media was approximately 1:3. The volume ratio of the powder mixture to the ethanol was 1:1. The batch was mixed using planetary ball milling for 24 h. Thereafter, the milled slurry was dried in a drying oven at 120 °C overnight. The dried powder was then ground and introduced into an alumina crucible. The closed alumina crucible was placed in a muffle furnace for calcination. The precursor was calcined at 1200 °C for 2 h. After calcining, the precursor was ground in an agate mortar. Then, to grind to an appropriate smaller size for experiments, the calcined precursor was milled via planetary ball milling with the yttrium stabilized zirconia balls and ethanol. The milled powder was then dried in a drying oven. The dried precursor powder was ground using agate mortar and then sieved through an 80 mesh sift.

Figure 4.1 shows the XRD pattern of the calcined $MgNb_2O_6$ precursor. **Figure 4.1a** illustrates a pure formation of Columbite phase. Commercially available $MgNb_2O_6$ precursor (H. C. Starck Tantalum & Niobium, 99.00 %) was also purchased and used for fabrication of ceramic samples. It is shown that the XRD pattern of the synthesized precursor sample is virtually identical to that of the manufactured precursor (**Figure 4.1b**)). We could therefore use either the synthesized precursor or the purchased precursor.

Table 4.1 Materials used for experiments.

Material	Provider	Purity, %
PbO	Hammond Group	99.00
MgO	Tateho	99.99
Nb_2O_5	Stanford advanced materials	99.90
$MgNb_2O_6$	H. C. Starck Tantalum & Niobium	99.00
TiO_2 rutile	Bio Scientific	99.80
In_2O_3	Alfa Aesar	99.99
Sm_2O_3	Alfa Aesar	99.95
MnO_2	Alfa Aesar	99.99

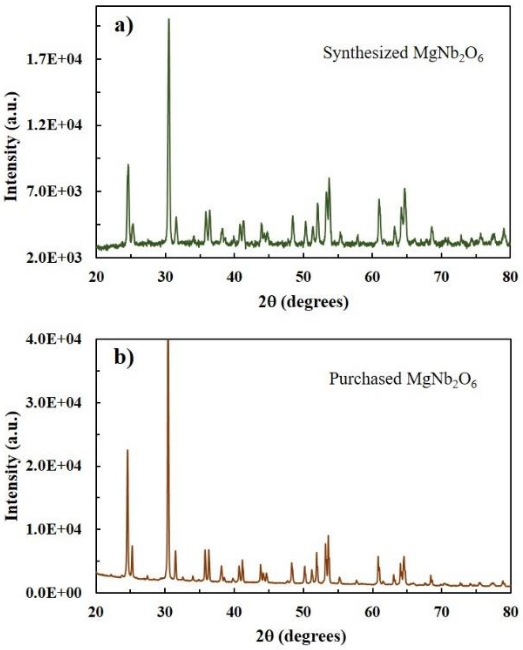

Figure 4.1 XRD patterns of precursors: a) synthesized $MbNb_2O_6$ and b) purchased $MgNb_2O_6$.

4.2.2 Ceramic fabrication

4.2.2.1 Study of the optimal conditions

It is important to fabricate high quality raw ceramic samples for single crystal growth. To do so, the conditions for ceramic processing and properties of fabricated ceramics need to be studied. The compositions of PMN-0.31PT ceramics were studied to obtain optimal conditions. For the study of optimal conditions, the amount of lead excess, calcination, and sintering were all investigated. The effects of cold isotropic pressing (CIP) and the annealing process were also studied. After ceramics fabrications, the dielectric and piezoelectric properties and the density of each patch were measured and compared to those of the references.

Oxide mixture

$MgNb_2O_6$, PbO, and TiO_2 were weighed out at their stoichiometric ratio. The oxide mixture was introduced into a PTFE milling jar. An excess of 0 – 3 %wt PbO was also added to the batch jar. Then, ethanol (Sigma-Aldrich, 99%) was added into the jar up to one third of its volume. The batch jar also included yttrium stabilized zirconia milling balls 5 mm in diameter that was added up to the surface of the ethanol. The contents of the batch jar were then mixed using a planetary ball milling machine for 24 h. After mixing, the slurry was dried in a drying oven overnight. The dried powder was lightly ground and preserved for the next step of the ceramic processing.

Calcination

PMN-PT ceramics are calcined at a temperature between 700 °C and 1000 °C for various periods [6,8,9,12-16]. In this experiment we calcined the samples within the temperature range of 750 °C to 900 °C. The calcination lasted from 2 h to 6 h. **Figure 4.2** presents the XRD patterns of PMN-0.31PT calcined at different temperatures. The patterns show that pure perovskite phases formed at 780 °C, 850 °C, and 900 °C. It is difficult, however, to distinguish small amounts of pyrochlore or excess lead oxide that could affect the properties of ceramics. Therefore, we evaluated the effects of the calcination temperature using measurements of the dielectric and piezoelectric properties of ceramics along with their densities. The temperature-dependence of the density and the longitudinal piezoelectric coefficient of PMN-0.31PT ceramics are shown in **Figure 4.3**. At 760 °C, the values of the density and piezoelectric coefficient in PMN-0.31PT ceramic are at their lowest (7.50 g/cm^3 and 350 pC/N, respectively) while they were the highest (7.80 g/cm^3 and 470 pC/N) in the sample that was calcined at 850 °C. The sample that was calcined at 900 °C showed the middle values (7.6 g/cm^3 and 410 pC/N). **Figure 4.4** presents the temperature dependence of the dielectric constant and loss of PMN-0.31PT samples calcined at 750 °C and 850 °C. It can be seen that the room temperature dielectric constant is 1300 for the sample calcined at 750 °C, but this is 2350 for the sample calcined at 850 °C. Also, the Curie temperatures are 165 °C and 148 °C in the 750 °C and 850 °C calcined samples, respectively.

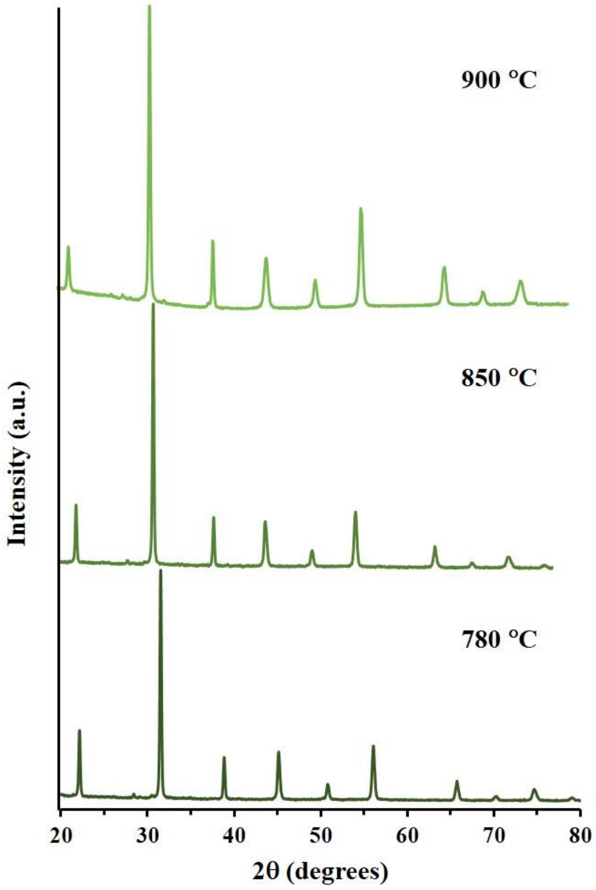

Figure 4.2 XRD patterns of PMN-0.31PT samples calcined at different temperatures.

The reason for the lowest values of dielectric and piezoelectric properties and density in the sample calcined at 750 °C could be the presence of pyrochlore phase. When the sample was calcined at a temperature lower than 770 °C, a small amount of pyrochlore could still remain, which was not detected by XRD measurements. It was reported that suppression of pyrochlore phase only starts above 750 °C, and pure-perovskite phase appeared from 850 °C [8,10]. Therefore, in our sample, the pyrochlore phase could still be present in lower calcination temperature.

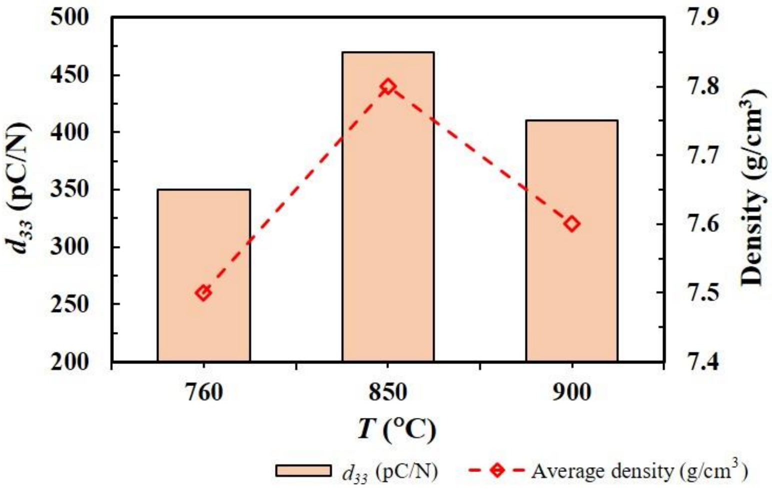

Figure 4.3 Longitudinal piezoelectric coefficient and density of PMN-0.31PT ceramics calcined at different temperatures.

Another reason for the low property values of the ceramic calcined at 750 °C is excess of lead oxide. **Figure 4.5** shows samples of PMN-0.29PT powder calcined at 750 ° C and 850 °C. The color of 750 ° calcined sample is orange-red, indicating the presence of lead oxide in **figure 4.5a**. This excess lead oxide was not due to added lead oxide but a remnant of the incomplete high-temperature solid-state reaction at low temperature. The excess of lead oxide is existed between grain boundaries and then became an insulating layer that reduced the dielectric property [11,17-19]. This excess promoted a higher Curie temperature [15], as shown in **figure 4.4a**. Free lead oxide can possibly avoid detection by XRD measurements [11]. In contrast, in **Figure 4.5b**, the sample calcined at 850 °C took on a white-yellow color and became denser after calcination, meaning that the high-temperature solid-solution reaction had been completed. Therefore, the dielectric and piezoelectric properties, as well as the density, were higher than those of the sample calcined at 750 °C (**Figure 4.3** and **Figure 4.4b**). The

Curie temperature was 148 °C in **Figure 4.4b** as well. For the sample calcined at 900 °C, when temperature was higher than 850 °C, it made the lead oxide volatile. Therefore, the density of the ceramic is lower than that of the 850 °C sample (**Figure 4.3**). The porosity in the polycrystalline material leads to decreases in the dielectric and piezoelectric constants and increases the dielectric loss [6,17-19].

Therefore, for calcination, the optimal conditions were found to be as 830-860 °C for 4 h.

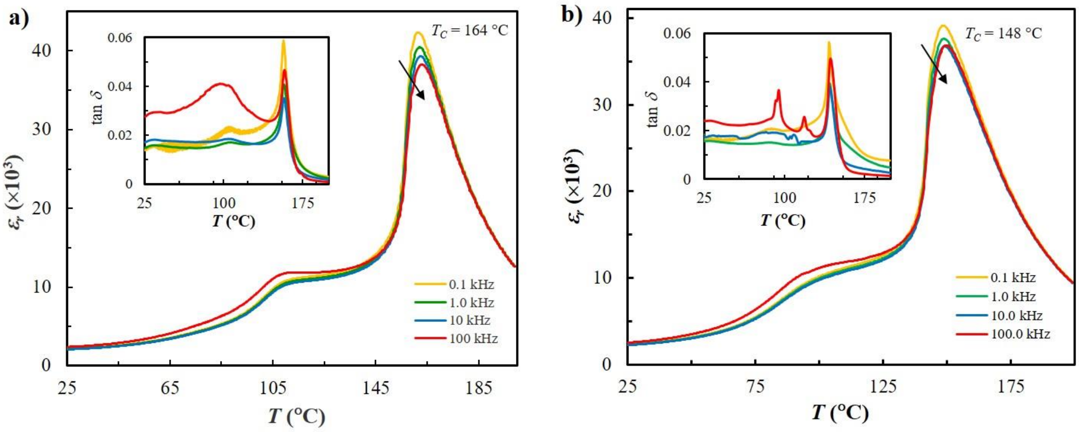

Figure 4.4 Temperature dependence of the dielectric constant and dielectric loss (insets) of PMN-0.31PT ceramic measured at frequencies from 100 Hz to 1 MHz: a) calcined at 750 °C and b) calcined at 850 °C.

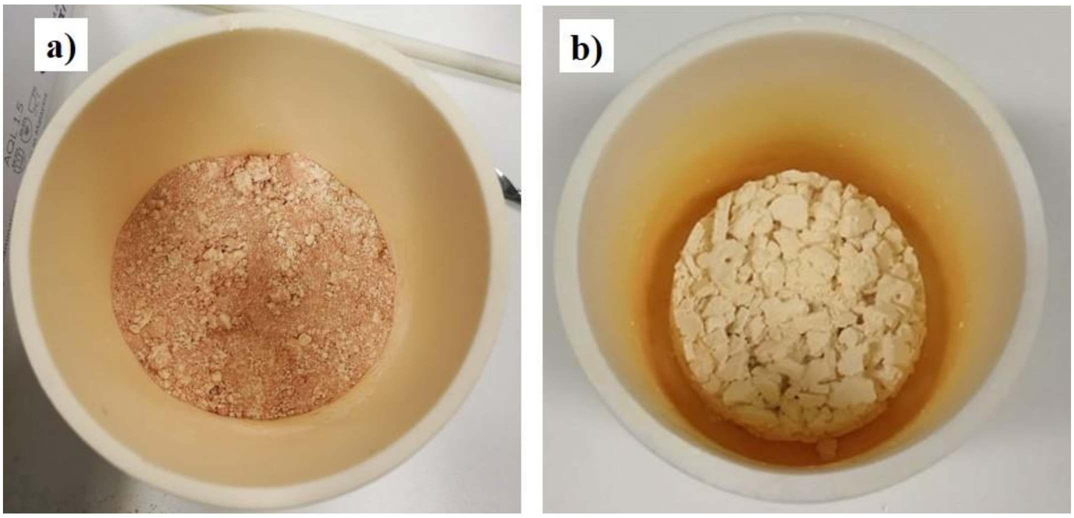

Figure 4.5 Calcined PMN-0.29PT samples: a) calcined at 760 °C and b) calcined at 850 °C.

Sintering

The calcined powder was pre-ground by mortar and pestle until the hard bulks were crushed sufficiently to make the particles small enough for ball milling. Then, the powder was added into a PTFE milling jar with yttrium stabilized zirconia milling balls. The volume ratio of the powder to the milling balls was 1 to 5. Ethanol (Sigma-Aldrich, 99%) was also introduced into the jar with approximately 1 wt% vinyl alcohol binder. The calcined PMN-PT powder was milled using a planetary ball milling machine for 24 h. The milled slurry was dried at 120 °C in a drying oven overnight. The dried powder was crushed using an agate mortar and then sieved through an 80-mesh sift.

The sieved powder was uniaxially pressed at 40 MPa to produce compact pellets 12 mm in diameter. In order to remove organic residuals of the binder, the pellets were heated at 600 °C for 2 h with heating speed of 1 °C/min in air using a conventional muffle furnace. After cooling to room temperature, the pellets were placed on Pt foil and covered by alumina in a crucible for sintering. **Figure 4.6a** shows green ceramic pellets placed on platinum foil. The pellets were surrounded by self-source powder in order to provide a PbO-rich environment to prevent PbO evaporation loss from the ceramic sample during the sintering. We used $PbZrO_3$ (PZ) and PMN-PT powders for the self-source powders. **Table 4.2** demonstrates the mass loss of sintered ceramic and the dependence of the dielectric constant on the self-source. In the case of the PZ self-source powder, only a slight mass loss or almost no loss was observed. This could be due to the adsorbed extra PbO from the easy decomposition of $PbZrO_3$ at high temperature. Adsorbed PbO in ceramics became incorporated into grain boundaries. Therefore, more excess lead oxide could lead to decreases in the piezoelectric coefficient, implying that the dielectric constant was also reduced [11,18,19]. When using PMN-PT powder as a sacrificial powder, the mass loss after sintering was ~1.4-1.8 wt.%. This loss was due to the volatilization of free lead oxide. In a four-hour sintering, the mass loss was higher than that in a two-hour, implying that more free lead oxide was released, and the piezoelectric coefficient was increased. Therefore, in this experiment, we used PMN-PT as the self-source powder.

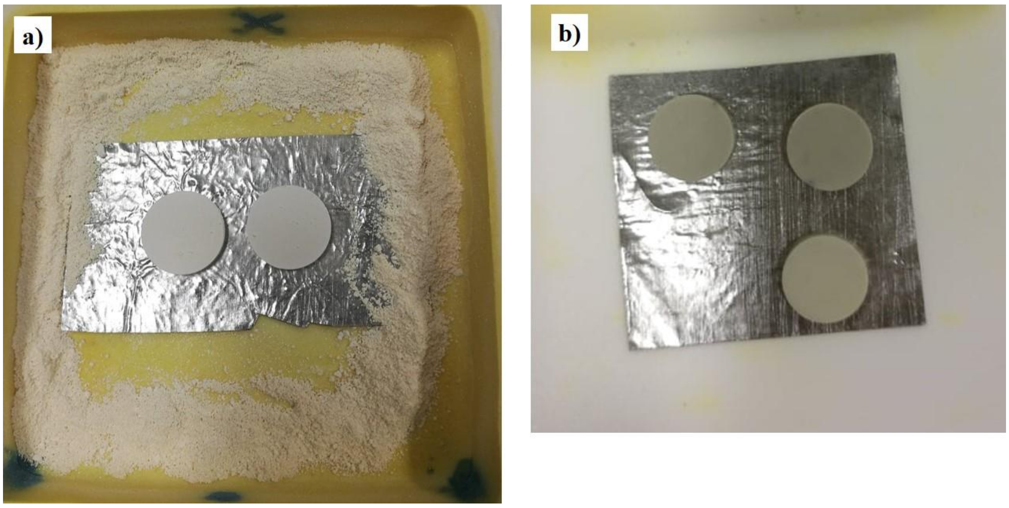

Figure 4.6 Green ceramic pellets. a) before sintering and b) after sintering.

Table 4.2 Effect of self-source powders on the longitudinal piezoelectric coefficient and mass loss of sintered PMN-0.31PT ceramic.

	PMN-0.31PT, sintered 2 h at 1250 °C		**PMN-0.31PT, sintered 4 h at 1250 °C**	
Self-source	**Mass loss (wt.%)**	**Piezoelectric coefficient (pC/N)**	**Mass loss (wt.%)**	**Piezoelectric coefficient (pC/N)**
PMN-PT	-1.4	440	-1.8	460
$PbZrO_3$	-0.05	400	- 0.01	390

Table 4.2 also shows the effect of sintering time. In the case of four-hour sintering, more mass loss occurred than for the two-hour sintering. A longer period of sintering could release a sufficient insulating lead oxide layer in the grain boundaries, and this increases dielectric constant. Also, increasing the sintering time enlarges the grains, which improves the dielectric property [23]. As a result, the piezoelectric property was enhanced, as shown in **Table 4.2**. The temperature effect was also studied. PMN-PT polycrystalline is usually sintered at 1170-1270 °C [16]. The sintered ceramic samples are shown in **Figure 4.6b**. In **Figure 4.7**, the density, mass loss, and dielectric and longitudinal piezoelectric coefficients of PMN-PT are shown as functions of the sintering temperature. Here, the samples were sintered at 1200 °C, 1220 °C, 1250 °C, and 1270 °C for 2 h. At 1200 °C, the lowest density and mass loss occurs, as well as the lowest dielectric and piezoelectric values. The highest density and mass loss

were observed when the ceramic was sintered at 1270 °C. For the sample sintered at 1250 °C, the mass loss and density were slightly lower than for the sample sintered at 1270 °C, although the values of the dielectric and piezoelectric responses were of the same order. The values of these properties in the sample sintered at 1220 °C were in the middle between those in the samples at 1200 °C and 1250 °C. When the sample was sintered at 1200 °C, the lowest densification occurred, and the low densification of the ceramic contributed to the property degradation [20-22]. It was also reported that low temperature sintering leads to pyrochlore [14]. With increasing temperature, the grain size of the ceramics was enlarged, leading to property enhancement [20, 23-28]. Therefore, our results show that the best property improvements were achieved when the sintering temperature was 1250°C or 1270 °C.

For sintering, a temperature of 1250°C to 1270 °C, a sintering period of four hours, and the use of PMN-PT as a self-source powder resulted in the best properties in the ceramic samples.

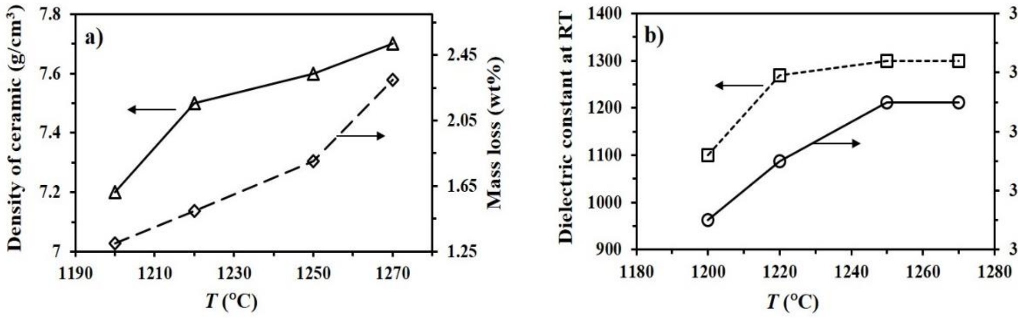

Figure 4.7 Density and mass loss as functions of sintering temperature (left), and the dielectric constant and longitudinal piezoelectric coefficient as functions of sintering temperature (right).

Effect of PbO excess

A certain amount of PbO excess helps to promote liquid phase in grain boundaries, which improves grain growth, thus aiding the ceramic densification [8,10,14,28-31]. As a result, the dielectric property increases. Extra excess lead oxide, however, could turn PbO into an insulating layer in grain boundary, leading to a gradient in the dielectric property [6,7,32]. It is therefore important to find the correct amount of PbO excess for optimal properties of ceramics. The longitudinal piezoelectric coefficient in PMN-0.31PT polycrystalline samples as a function of lead oxide excess is shown in

Figure 4.8. In this experiment, PbO excesses of 0, 1, 1.5, 2, and 3 wt% were used. When the lead excess started with 1 wt%, the piezoelectric property was improved, but when the excess amount was between 1 wt% and 3 wt%, only a very slight property difference was observed. For ceramic fabrication, we therefore used 1.5-2.0 wt% lead excess.

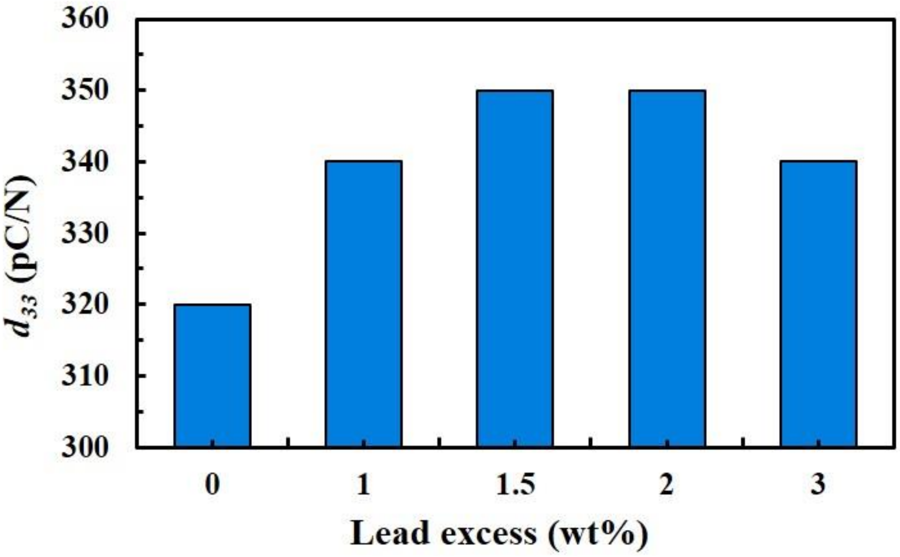

Figure 4.8 Longitudinal piezoelectric coefficient of PMN-0.31PT ceramic as a function of PbO excess.

Effect of annealing

After sintering, a high-temperature annealing process helps to evaporate the free lead oxide in grain boundaries and aids in growing grains [20,23]. The samples were annealed at 1100 °C for 2-4 h in open air after sintering at 1250 °C for 2 h. After annealing, we measured the dielectric and piezoelectric properties. It was found, however, that almost no property difference between the un-annealed and annealed samples could be detected. To save time, we therefore left out the annealing step during ceramic fabrication.

Effect of Cold Isostatic Pressing (CIP)

We also studied the effects of CIP. CIP is used to increase the density and reduce the porosity of ceramics [19,33,34]. To do so, after organic binder burn-off, the pellets were pressed by CIP at 200 MPa for 5 min. The results showed that there was only a very slight difference in properties between the

CIP-pressed sample and the un-pressed sample. Therefore, we ignored CIP to save time for ceramic preparation.

4.2.2.2 Fabrication of PMN-PT ceramics

For PMN-PT ceramics, compositions of 0.72PMN-0.28PT, 0.71PMN-0.29PT, and 0.69PMN-31PT were fabricated. Ceramic compositions were prepared based on the study of optimal conditions.

Oxide mixture

For each oxide composition, 0.72PMN-0.28PT, 0.71PMN-0.29PT, and 0.69PMN-31PT, $MgNb_2O_6$, PbO and TiO_2 were weighed out at their stoichiometric ratio and introduced into a PTFE milling jar. 2 wt% PbO excess was added to the jar. Ethanol and milling balls were also added at the ratio described in section 4.2.2.1. The oxide mixture was milled using a planetary ball milling machine for 24 h. The slurry was dried in a drying oven at 120 °C.

Calcination

The dried powders were calcined at 850 °C for 4 h in a closed alumina crucible in a muffle furnace according to the obtained optimal conditions. After calcination, the powder was crushed using an agate mortar and preserved for sintering.

Sintering and characterization

The calcined powder was charged into a milling jar. Ethanol and yttrium stabilized zirconia milling balls were also brought into the jar at the ratio described in section 4.2.2.1. The calcined powder was milled in the ball milling machine. After the ball milling, the slurry was dried in the oven at 120 °C. For quality control, a small amount of powder was taken from the dried slurry. The powder was then milled with 1 wt% vinyl alcohol binder for 4 h. The rest of dried slurry was preserved for single crystal growth. The milled powder was then dried and sieved with an 80-mesh sift. After that, the powder was uniaxially pressed, as described in section 4.2.2.1. The organic residuals in the pellets from the binder were burned off in a conventional muffle furnace, as mentioned in section 4.2.2.1. The green ceramic pellets were put on Pt foil and surrounded by PMN-PT self-source powder. According to the optimal conditions in section 4.2.2.1, the samples were sintered at 1250 °C for 4 h in a conventional muffle furnace. After sintering, the surfaces of the ceramic pellets were polished using silica carbide sandpaper to remove the damage and pyrochlores. The polished samples were then cleaned in an ultrasonic cleaner with distilled water and followed by ethanol. Average densities of the sintered ceramics were 7.75 g/cm^3 in PMN-28PT, 7.83 g/cm^3 in PMN-29PT, and 7.80 g/cm^3 in PMN-0.31PT, which are ~95 % of theoretical values. In order to study their electric properties, the sintered pellets had silver electrodes applied on their top and bottom faces, and they were then fired at 850 °C for 5 min. Thereafter, the ceramic samples were poled with a 20 kV/cm dc field at room temperature. Before characterization was begun, the poled samples were left at least for 24 hours at normal ambient condition.

In figure 4.9, the XRD patterns confirm that all components of the sintered samples were pyrochlore-free and pure perovskite phases. In (200) diffraction peak, there is no broadening or splitting observed, indicating the existence of rhombohedral phases in all components. **Table 4.3** shows the properties determined for the PMN-PT compositions and their comparisons to the reference values. Here the reference values are taken from reference materials [10,32-38]. The values for dielectric constants, dielectric loss, piezoelectric coefficients, and Curie temperatures in PMN-PT compositions are shown to be quite close to those of the references, indicating that good quality ceramic samples were fabricated. **Figures 4.10a** and **b** shows the dielectric constants and dielectric losses in the PMN-0.31PT composition as functions of temperature. Two dielectric anomalies were found in the temperature dependent dielectric constant curve. The first anomaly was observed at around 95 °C, which corresponds to the rhombohedral-to-tetragonal phase transition. The other anomaly was shown at 148 °C, and this was accord with the tetragonal-to-paraelectric phase transition.

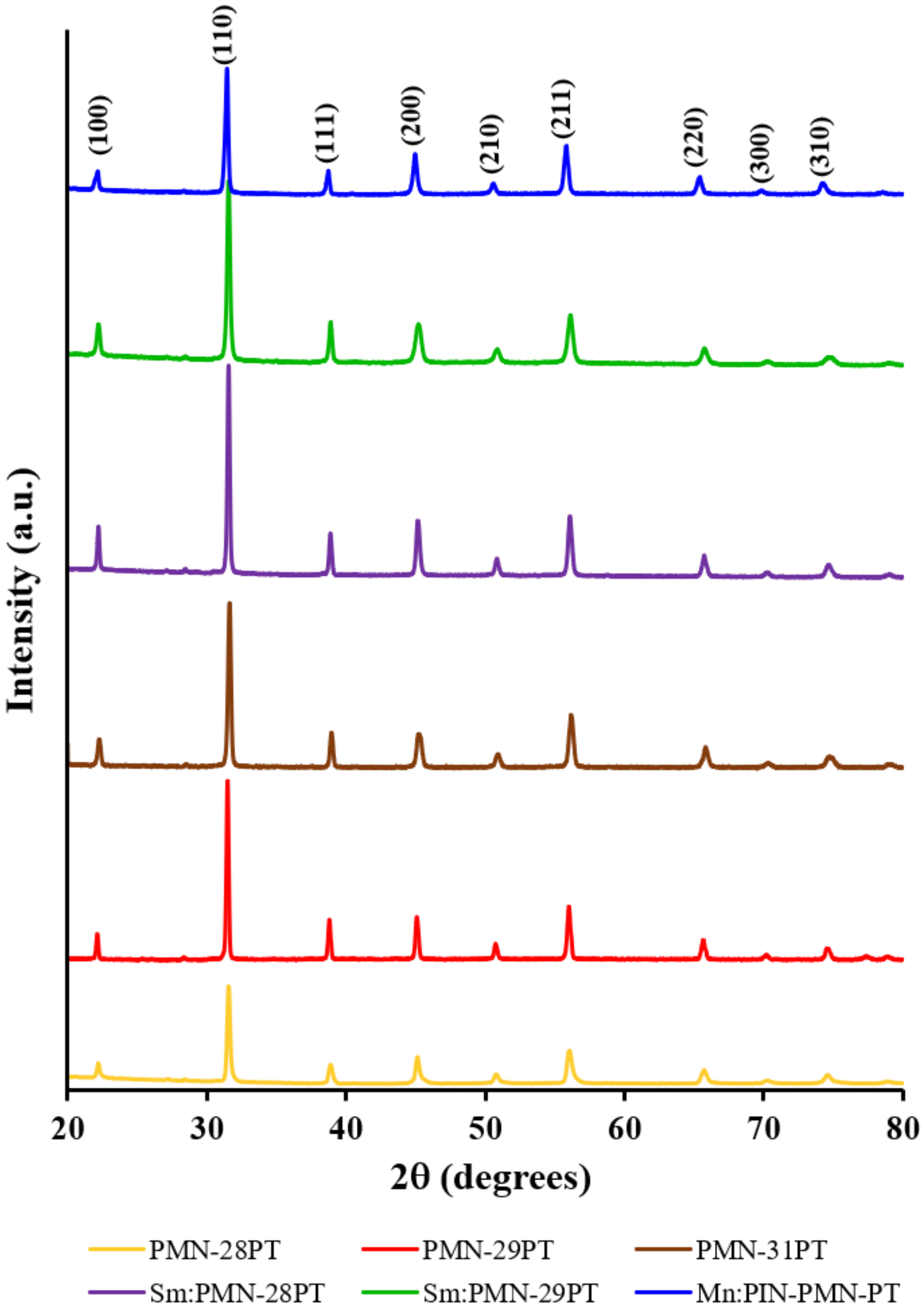

Figure 4.9 X-ray diffraction patterns for ceramic samples fabricated under optimal conditions.

Table 4.3 Properties of the synthesized ceramics in comparison to the reference values [10,32-38].

Composition	d_{33}, (pC N^{-1})		$\varepsilon^T/\varepsilon_0$, at RT		Loss factor at 1 kHz		T_C (°C)	
	Result	Ref. val.	Result	Ref. val.	Result`	Ref. val.	Result	Ref. val.
PMN-0.28PT	310	320	2000	2200	0.012	0.020	137	136
PMN-0.29PT	370	360	2400	2600	0.012	0.020	144	140
PMN-0.31PT	470	450	2630	2900	0.018	0.020	148	145
PMN-0.28PT-0.01Sm	410	420	2300	2500	0.011	0.022	117	118
PMN-0.29PT-0.01Sm	470	460	2860	2800	0.017	0.020	118	120
0.28PIN-43PMN-0.29PT-0.01Mn	265	-	1050	-	0.007	-	190	192

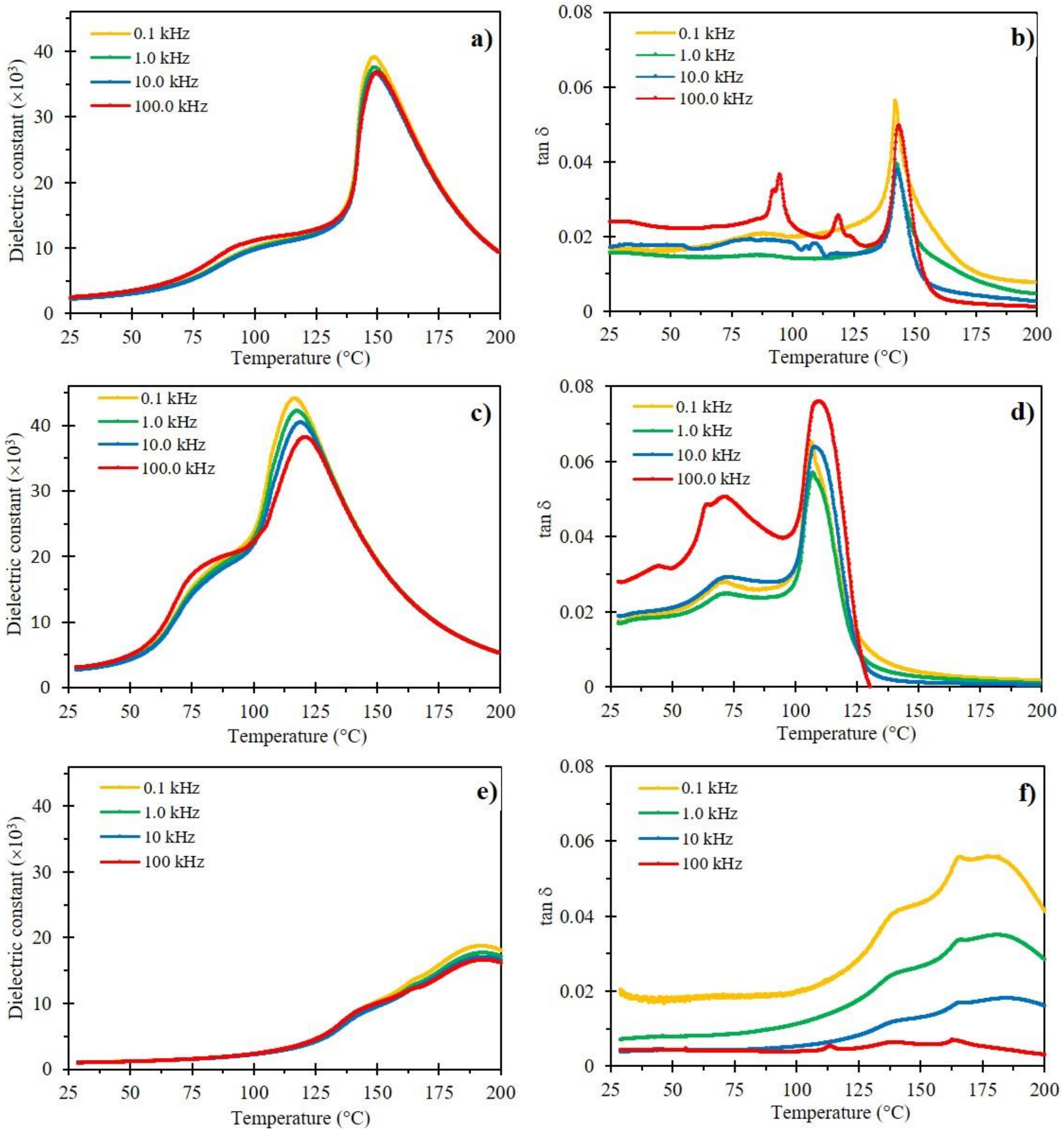

Figure 4.10 Dielectric property and loss as functions of temperature and frequency in compositions of (a, b) PMN-0.31PT, (c, d) Sm-PMN-0.29PT, and (e, f) Mn-PIN-PMN-0.29PT crystals, respectively.

Ceramic pellet preparation for single crystals growth

The 0.72PMN-0.28PT and 0.71PMN-0.29PT compositions were prepared for single crystal growth, and their pellets were pressed according to the shape of the Pt crucible. The crucible constitutes the main part of the cylinder with a diameter of 25 mm and a tapered lower part with a diameter of 10 mm, as shown in **Figure 4.11**. Therefore, two different sizes of sintered ceramics needed to be prepared. The calcined powders after milling were ground using an agate mortar and then sieved with an 80-mesh sift. For the 0.71PMN-0.29PT ceramic, the powder was then pressed to produce pellets 30 mm and 11 mm in diameter in stainless steel pressing dies at 30 MPa. For 0.72PMN-0.28PT, only sample pellets 30 mm in diameter were prepared. The reason for this will be explained in section 5.3.1. The pellets were sintered at 1250 °C for 4 h. After sintering, the 30 mm and 11 mm diameter raw ceramics had shrunken to approximately 24 mm and 9 mm (20 % shrinkage), respectively. **Figure 4.12** shows the bigger pellets that were sintered. Therefore, these sizes of ceramics fit quite well into the Pt crucible. If a ceramic pellet contained a residual of organic compound or any other contamination, this could react with Pt during the single crystal growth. The binder was therefore not used for those samples.

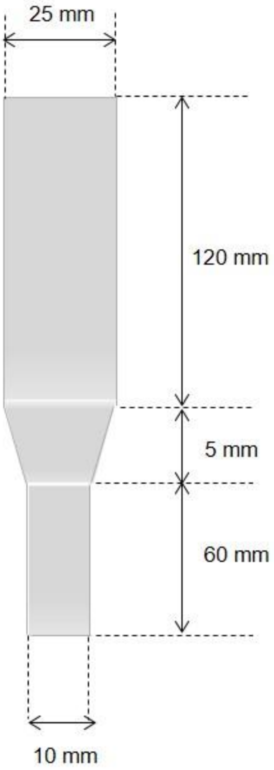

Figure 4.11 Dimensions of Pt crucible.

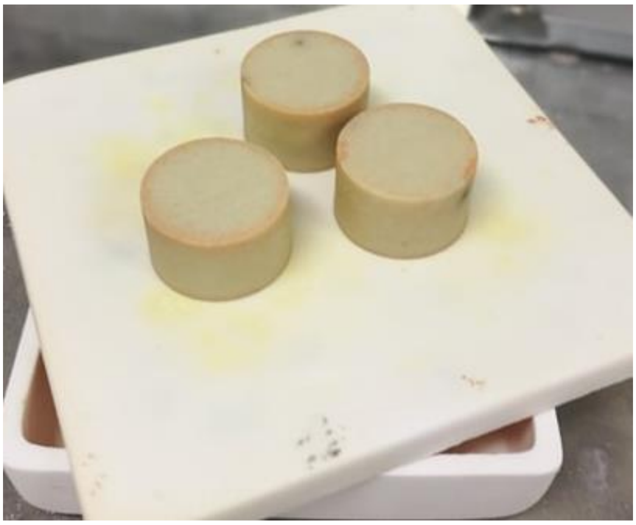

Figure 4.12 Sintered big pellets of PMN-PT ceramic.

4.2.2.3 Fabrication of Sm-doped PMN-PT ceramic

For Sm-doped ceramic samples, we fabricated compositions of Sm-0.72PMN-0.28PT and Sm-0.72PMN-0.29PT. As with previous compositions, after ceramic fabrication, the properties of the prepared samples were tested.

Oxide mixture

For Sm-doped PMN-PT, the oxides of $MgNb_2O_6$, PbO, and TiO_2, were stoichiometrically weighed and put into a milling jar. For Sm doping, 1 mol% Sm_2O_3 was added to the jar. Also, 2 wt% PbO excess was added. The ethanol and the milling balls were also introduced in their proper ratio. The oxide mixture was mixed in the way that described in section 4.2.2.1. The mixed slurry was dried in the oven.

Calcination

The dried mixture was introduced into an alumina crucible. The sample was calcined with the cap closed at 850 °C for 4 h. The processes of drying and milling after calcination were followed according to section 4.2.2.2.

Sintering and characterisation

As described in section 4.2.2.1, some amount of milled powder was taken for property tests. The conditions for milling, binder, and drying were all as same as those in described in section 4.2.2.1.

In the next steps, the powders were pressed to make ceramic pellets with pressing dies 12 mm diameter, and then the organic residual was burned off according to the same method as in section 4.2.2.1. The sintering process also followed the method in section 4.2.2.1. The samples were sintered at 1250 °C for 4 h. The XRD patterns in **Figure 4.9** show that the pure perovskite phase was formed after sintering. The average densities of the sintered samples were 7.77 g/cm^3 in Sm-PMN-0.28PT, and 7.75 g/cm^3 in Sm-PMN-0.29PT, and these values are > 95 % of the theoretical density. Polishing and silver-electrode fire-on processes also followed. The samples were poled at 20 kV/cm. After that, the samples were aged for 24 h. After aging, their dielectric and piezoelectric properties were measured under the same conditions as in section 4.2.2.1. **Figures 4.10c** and **d** shows the dielectric constant and loss depending on temperature in the Sm-PMN-0.29PT composition. In the dielectric constant vs temperature curve, two anomalies were observed. The anomalies in dielectric constants curve is more broadened when compared to the those of pure PMN-0.31PT crystal, confirming lower PT content and more relaxor behaviour. The first anomaly was appeared near 75 °C, indicating the rhombohedral-to-tetragonal phase transition. The second anomaly was shown at 118 °C, signifying the tetragonal-to-paraelectric phase transition. The dielectric loss vs temperature curve also proves these two anomalies in **Figure 4.1d**.

Table 4.3 shows that the dielectric constants and dielectric loss factors in 0.72PMN-0.28PT-0.01Sm and 0.72PMN-0.29PT-0.01Sm compositions were 2300, 2860, and 0.011 and 0.017, respectively. The piezoelectric coefficients were 410 pC/N in 0.72PMN-0.28PT-0.01Sm and 470 pC/N in 0.72PMN-0.29PT-0.01Sm. These values are quite identical to those of the references. The piezoelectric and dielectric property values in Sm-doped ceramic were increased compared to those of pure PMN-0.29PT and PMN-0.29PT composition but similar to those of pure PMN-0.31PT composition. However, the Curie temperatures were decreased much lower. The specific reasons for those property changes were clearly discussed in **Chapter 3.1.2**. Therefore, the results of characterisation indicate that good quality Sm-doped ceramic materials were fabricated using the optimal conditions.

Ceramic pellet preparation for single crystal growth

For single crystal growth of the Sm-doped samples, the ceramic preparation followed the same steps described in the previous section. For the 0.71PMN-0.29PT-0.01Sm composition, the pellets were pressed in 30 mm diameter and 11 mm diameter pressing dies, respectively. For the 0.72PMN-0.28PT-0.01Sm sample, only 30 mm pellets were prepared. The prepared pellets were sintered at 1250 °C for 4 h. After sintering, the shrinkage and mass loss were measured, and then the pellets were preserved for single crystal growth.

Fabrication of Mn-doped PIN-PMN-PT ceramics

For the Mn-modified ceramic samples, only the 0.28PIN-0.43PMN-0.29PT-0.01Mn composition was fabricated. The ceramic preparation followed all the previous processes based on the study of optimal conditions. The quality of prepared ceramic sample was then characterised.

Oxide mixture

For Mn-PIN-PMN-PT, $MgNb_2O_6$, PbO, TiO_2, and In_2O_3 were stoichiometrically weighed and put into a milling jar. 1 mol% of MnO_2 was added to the oxide mixture. Also, 2 wt% PbO excess was put into the mixture. Ethanol and milling balls were added to the mixture. The jar mixture was mixed under the same conditions as for the previous ceramic compositions. The drying process was also followed.

Calcination

The mixed oxides were calcined in a closed alumina crucible in a conventional muffle furnace at 850 °C for 4 h. The calcined sample was milled in the way described in section 4.2.2.1. After milling, the slurry was dried in the oven and sieved with an 80-mesh sift.

Sintering and characterisation

For property tests, some powder was taken and milled with 1 wt% binder and dried. The pellets were prepared using a 12 mm pressing die. The organic residual was removed by the method in section 4.2.2.1. The green ceramic pellets were placed on Pt foil with PMN-PT self-source powder. The samples were sintered at 1270 °C for 4 h. After that, the sintered samples were polished using carbide sandpaper and cleaned in water and then ethanol using an ultrasonic machine. The average density of the Mn-PIN-PMN-PT composition was 8.08 g/cm^3, so a very high-density ceramic was prepared.

The ceramic samples were pasted with silver paste for the electrodes and fired at 850 °C for 5 min. All samples were poled under 20 kV/cm for 60 s. The samples were stayed at room condition for 24 hours. Then, the samples were characterised. **Figure 4.10e** and **f** shows the dielectric constant and loss as functions of temperature**.** In the dielectric constant vs temperature curve, two peaks were shown as dielectric constant anomalies. The first peak was appeared near 140 °C, indicating the rhombohedral-to-tetragonal phase transition. The second peak was exhibited at 190 °C, signifying the tetragonal-to-paraelectric phase transition. These phase transition temperatures were increased much higher than those of pure or donor-doped PMN-PT crystals. The specific details of the increases were discussed in chapter 1 and 2. The dielectric loss anomalies also confirm these phase transitions in **Figure 4.1f**.

In **Table 4.3**, the dielectric constant and dielectric loss at room temperature are 1050 and 0.007 at 1 kHz. The dielectric loss is significantly lower than those of the previously prepared samples. This is because of “hardening effect” induced by Mn ions in the ceramic. The longitudinal piezoelectric coefficient is 265 pC/N. This value is lower than those of the previously prepared samples because of restricted domain wall motion due to the “hardening effect” [17]. The specific details of “hardening effect” was discussed in **Chapter 3.1.2**. These values show the good quality of ceramic samples.

Ceramic pellet preparation for single crystal growth

The pellets of the Mn doped sample were pressed in 30 mm diameter and 11 mm diameter pressing dies, respectively. The prepared pellets were sintered at 1250 °C for 4 h. After sintering, the shrinkage and mass loss were measured, and then the pellets were preserved for single crystal growth.

4.3 Conclusion

Ceramic samples of PMN-0.29PT, PMN-0.31PT, Sm-PMN-0.28PT, Sm-PMN-0.29PT, and Mn-PIN-PMN-0.29PT compositions were prepared using the two-step Columbite method [1]. Optimal condition for ceramic preparation was studied. For calcination, the temperature and time were set at 850 °C and 4 h. When the calcination temperature was less than 780 °C, an incomplete high-temperature reaction was occurred, so the properties of the ceramic sample were degraded. For sintering, the optimal temperature and time were obtained to be 1230-1250 °C and 3-4 h, respectively. A higher temperature and a longer period of sintering resulted in less density of the ceramic sample. Hence, the properties of the samples were degraded. Furthermore, it was found that CIP and annealing processes did not result in outstanding property improvements. The excess of lead oxide was set at 2-3 wt%. After the optimal conditions were found, all the compositions were characterised, and their properties were compared to other references to confirm the proper properties of the ceramics. For property characterisation, dielectric and piezoelectric responses were studied. All values of the dielectric and piezoelectric properties in the ceramic samples were observed to be quite consistent with other references. The characterization values therefore indicated high quality of the ceramic samples.

Based on the optimal conditions and property study results, raw ceramic samples for single crystal growth were prepared. Without any binder, the calcined powders were pressed with two different pressing dies. The samples were sintered under optimal conditions for each composition.

References

[1] P. Han, J. Tian, and W. Yan, Bridgman growth and properties of PMN-PT-based single crystals. In *Handbook of Advanced Dielectric, Piezoelectric and Ferroelectric Materials: Synthesis, Properties and Applications*; Ye, Z.G., Ed.; Woodhead: Cambridge, UK, 2008; pp. 3–37.

[2] S. L. Swartz and T. R. Shrout, "Fabrication of Perovskite Lead Magnesium Niobate," *Mater. Res. Bull.*, **17**, 1245–50 (1982).

[3] J. Lu and S. Zhang, Advances in the growth and characterization of relaxor-PT-based ferroelectric single crystals, *Crystals*, **4**, 306-330 (2014).

[4] P. Han, J. Tian, and W. Yan, Bridgman growth and properties of PMN-PT-based single crystals. In *Handbook of Advanced Dielectric, Piezoelectric and Ferroelectric Materials: Synthesis, Properties and Applications*; Ye, Z.G., Ed.; Woodhead: Cambridge, UK, 2008; pp. 3–37.

[5] W. Hackenberger, J. Luo, X. N. Jiang, K. A. Snook, P. W. Rehrig, S. J. Zhang, and T. R. Shrout, Recent developments and applications of piezoelectric crystals. In *Handbook of Advanced Dielectric, Piezoelectric and Ferroelectric Materials–Synthesis, Characterization and Applications*; Ye, Z.G., Ed.; Woodhead: Cambridge, UK, 2008; pp. 73–100.

[6] M. Villegas, A. C. Caballero, M. Kosec, C. Moure, P. Duráan, and J. F. Fernandez, Effects of PbO excess in Pb $(Mg_{1/3}Nb_{2/3})$ O_3–$PbTiO_3$ ceramics: Part I. Sintering and dielectric properties. *J. Mater. Res.*, **14**, 891-897 (1999).

[7] H. C. Wang and W. A. Schulze, The role of excess magnesium oxide or lead oxide in determining the microstructure and properties of lead magnesium niobate. *J. Am. Ceram. Soc.*, **73**, 825-832 (1990).

[8] K. Kusumoto and T. Sekiya, Processing and properties of $(1-x)Pb(Mg_{1/3}Nb_{2/3})O_3 \cdot xPbTiO_3$ solid solutions from PbO-and MgO-excess compositions, *Mater. Res. Bull.* **33**, 1367-1375 (1998).

[9] E. Goo, T. Yamamoto, and K. Okazaki, Microstructure of Lead-Magnesium Niobate Ceramics. *J. Am. Ceram. Soc.*, **69**, C-188 (1986).

[10] P. Augustine, and M. R. Rao, Realization of device quality PMN–PT ceramics using modulated heating method. *Ceram. Int.*, **41**, 11984-11991 (2015).

[11] H. C. Ling, A. M. Jackson, M. F. Yan, and W.W. Rhodes, Effect of PbO evaporation on the composition and dielectric properties of PbO-MgO-Nb_2O_5 based dielectrics, *J. Mater. Res.*, **5**, 629-639 (1990).

[12] J. Kelly, M. Leonard, C. Tantigate, and A. Safari, Effect of composition on the electromechanical properties of (1-x)$Pb(Mg_{1/3}Nb_{2/3})O_3$–x$PbTiO_3$ ceramics, *J. Am. Ceram. Soc.*, **80**, 957–964 (1997).

[13] F. Li, D. Lin, Z. Chen, Z. Cheng, J. Wang, C. Li, Z. Xu, Q. Huang, X. Liao, L. Q. Chen, T. R Shrout, and S. Zhang, Ultrahigh piezoelectricity in ferroelectric ceramics by design. *Nat. Mater.*, **17**, 349-354 (2018).

[14] Y. C. Liou and L. Wu, Effect of heating rate on the dielectric properties of the PMN-PT relaxor ceramics, *J. Am. Ceram. Soc.*, **77**, 3255-3258 (1994).

[15] E. M. Sabolsky, S. Trolier-McKinstry, and G. L. Messing, Dielectric and piezoelectric properties of ⟨001⟩ fiber-textured $0.675Pb(Mg_{1/3}Nb_{2/3})O_3 - 0.325PbTiO_3$ ceramics, *J. Appl. Phys.*, **93**, 4072 (2003).

[16] M. H. Lente, A.L. Zanin, S.B. Assis, I.A. Santos, J.A. Eiras, and D. Garcia, Effect of the composition and sintering process on the electrical properties in $Pb(Mg_{1/3}Nb_{2/3})O_3$–$PbTiO_3$ ceramics, *J. Eur. Ceram. Soc.*, **24**, 1529–1533 (2004).

[17] W. R. Jeffe Cook and H. Jaffe, Piezoelectric Ceramics." Academic Press Inc. (London) Ltd, 1971, pp 8-15.

[18] P. Papet, J. P. Dougherty, and T. R. Shrout, Particle and grain size effects on the dielectric behavior of the relaxor ferroelectric $Pb(Mg_{1/3}Nb_{2/3})O_3$, *J. Mater. Res.*, **5**, 2902-2909 (1990).

[19] M.N. Rahaman, "Ceramic Processing and Sintering", Marcel Dekker, 1995, New York, pp. 49-118, 778-841.

[20] L. Jin, Y. Huang, L. Zhang, R. Jing, L. Huang, Q. Hu, D. Guo, G. Wang, X. Wei, X. Lu, F. Wei, and G. Liu, Enhanced dielectric and ferroelectric properties in lead magnesium niobate-lead titanate ferroelectrics solid solutions by controlling the sintering protocols, *Ceram. Int.*, **46**, 25608-25618 (2020).

[21] H. Luo, W. Y. Shih, and W. H. Shih, Double precursor solution coating approach for low-temperature sintering of $[Pb(Mg_{1/3}Nb_{2/3})O_3]0.63[PbTiO_3]_{0.37}$ solids, *J. Am. Ceram. Soc.*, **90**, 3825–3829 (2007).

[22] I. Fujii, R. Yoshida, T. Imai, S. Yamazoe, and T. Wada, Fabrication of Transparent $Pb(Mg_{1/3}Nb_{2/3})O_3$–$PbTiO_3$ based ceramics by conventional sintering, *J. Am. Ceram. Soc.*, **96**, 3782–3787 (2013).

[23] E. R. Leite, A. M. Scotch, A. Khan, T. Li, H. M. Chan, M. P. Harmer, S.-F. Liu, and S.-E. Park, Chemical heterogeneity in PMN–35PT ceramics and effects on dielectric and piezoelectric properties, *J. Am. Ceram. Soc.*, **85**, 3018–24 (2002).

[24] U.-J. Chung, W. Jo, J.-H. Lee, N.-M. Hwang, and D.-Y. Kim, Coarsening process of penetration-twinned grains in PMN-35 mol% PT ceramics, *J. Am. Ceram. Soc.*, **87**, 125-128 (2004).

[25] M.H. Lente, A.L. Zanin, S.B. Assis, I.A. Santos, J.A. Eiras, and D. Garcia, Effect of the composition and sintering process on the electrical properties in $Pb(Mg_{1/3}Nb_{2/3})O_3$–$PbTiO_3$ ceramics, *J. Eur. Ceram. Soc.*, **24**, 1529–1533 (2004).

[26] M. Algueró, B. Jiménez, and L. Pardo, Transition between the relaxor and ferroelectric states for $(1-x)Pb(Mg_{1/3}Nb_{2/3})O_3$–$xPbTiO_3$ with x=0.2 and 0.3 polycrystalline aggregates, *Appl. Phys. Lett.*, **87**, 082910 (2005).

[27] M. Algueró, J. Ricote, R. Jiménez, P. Ramos, J. Carreaud, B. Dkhil, J. M. Kiat, J. Holc, and M. Kosec, Size effect in morphotropic phase boundary $Pb(Mg_{1/3}Nb_{2/3})O_3$–$PbTiO_3$, *Appl. Phys. Lett.* **91**, 112905 (2007).

[28] H. Amorin, H. Urisic, P. Ramos, J. Holc, R. Moreno, D. Chateigner, J. Ricote, and Miguel Alguero, $Pb(Mg_{1/3}Nb_{2/3})O_3$–$PbTiO_3$ textured ceramics with high piezoelectric response by a novel templated grain growth approach, *J. Am. Ceram. Soc.*, **97**, 420–426 (2014).

[29] J. P. Guha, D. J. Hong, and H. U. Anderson, Effect of excess PbO on the sintering characteristics and dielectric properties of $Pb(Mg_{1/3}Nb_{2/3})O_3$-$PbTiO_3$-based ceramics, *J. Am. Ceram. Soc.*, **71** C-152 (1988).

[30] C. E. Seow, D. Y. Yoon, J. S. Wallace, and J. E. Blendell, Dependence of grain shape and growth on PT content in PbO-excess PMN–PT, *J. Am. Ceram. Soc.*, **89**, 1668–1672 (2006).

[31] S. L. Swartz, T. R. Shrout, W. A. Schulze, and L. E. Cross, Dielectric properties of lead-magnesium niobate ceramics, *J. Am. Ceram. Soc.*, **67**, 311-314 (1984).

[32] J. Chen and M. P. Harmer, Microstructure and dielectric properties of lead magnesium niobate-pyrochlore diphasic mixtures, *J. Am. Ceram. Soc.*, **73**, 68-73 (1990).

[33] A. D. Moriana and S. Zhang, Enhancing electromechanical properties of $Pb(Sc_{1/2}Nb_{1/2})O_3$- $PbZrO_3$-$PbTiO_3$ piezoelectric ceramics via templated grain growth, *Adv. Electron. Mater.*, 2100919 (2021).

[34] Y. Zhang, D. Xue, H. Wu, X. Ding, T. Lookman, and X. Ren, Adaptive ferroelectric state at morphotropic phase boundary: coexisting tetragonal and rhombohedral phases, *Acta Mater.*, **71** 176–184 (2014).

[35] S. W. Choi, T. R. Shrout, S. J. Jang, and A. S. Bhalla, Influence of manganese doping to the full tensor properties of morphotropic phase boundary in Pb $(Mg_{13}Nb_{23})$ O_3-$PbTiO_3$ system, *Mater. Lett*, **8**, 253-255 (1989).

[36] F. Li, S. Zhang, Z. Xu, Xi. Wei, J. Luo, T. R. Shrout, Composition and phase dependence of the intrinsic and extrinsic piezoelectric activity of domain engineered $(1-x)Pb(Mg_{1/3}Nb_{2/3})O_3-xPbTiO_3$ crystals, *J. Appl. Phys.* **108**, 034106 (2010).

[37] O. Noblanc, P. Gaucher, G. Calvarin, Structural and dielectric studies of $Pb(Mg_{1/3}Nb_{2/3})O_3$–$PbTiO_3$ ferroelectric solid solutions around the morphotropic boundary, *J. Appl. Phys.* **79**, 8 (1996).

[38] E. Sun, R. Zhang, F. Wu, B. Yang, W. Cao, Influence of manganese doping to the full tensor properties of $0.24Pb(In_{1/2}Nb_{1/2})O_3$-$0.47Pb(Mg_{1/3}Nb_{2/3})O_3$-$0.29PbTiO_3$ single crystals. *J. Appl. Phys.*, **113**, 074108 (2013).

Chapter 5. Single crystal growth

This chapter will discuss the results of single crystal growth. Three single crystals were grown with the PMN-PT, Sm-PMN-PT, and Mn-PIN-PMN-PT compositions. The features and significance of each composition have been discussed in Chapters 2 and 3.

The furnace used for single crystal growth is introduced in this chapter. Also, this chapter includes the results of dummy run experiments for testing the furnace's operations.

5.1 Furnace

The furnace used for crystal growth is a Vertical Bridgman Furnace, manufactured by the Mellen Company, USA, as shown in **Figure 5.1**. The general layout of this furnace is given in **Figure 3.8.** The furnace comprises two zones separated by an adiabatic layer. 16 SiC heating element are set in each zone. Three thermocouples (TCs) are used to control the entire system. The first and second thermocouples measure the temperatures of zone I and zone II, respectively. A third thermocouple measures the temperature of the charge. The operation of the furnace is monitored by the ADAPT TCAS computer control program. This program is able to set the conditions and log all the data of the operations. The furnace is installed in a vertical position, and the translation system is lodged underneath it. The translation system is able to operate in the axial and radial directions. The translation and its speed are controlled by the Setup Motion Controlling program.

After the furnace was installed in the laboratory, several small modifications were made in order to fit into our experimental conditions. The alumina tube for the translation was changed to shorter one for easy sample loading. The third thermocouple was also cut to fit into the length of the modified alumina tube. Some safety protections were also used. High-temperature insulation bricks were used to cover the top of the furnace to prevent it from releasing high heat into the ceiling. During the operation of the furnace, frequent environmental controls were performed.

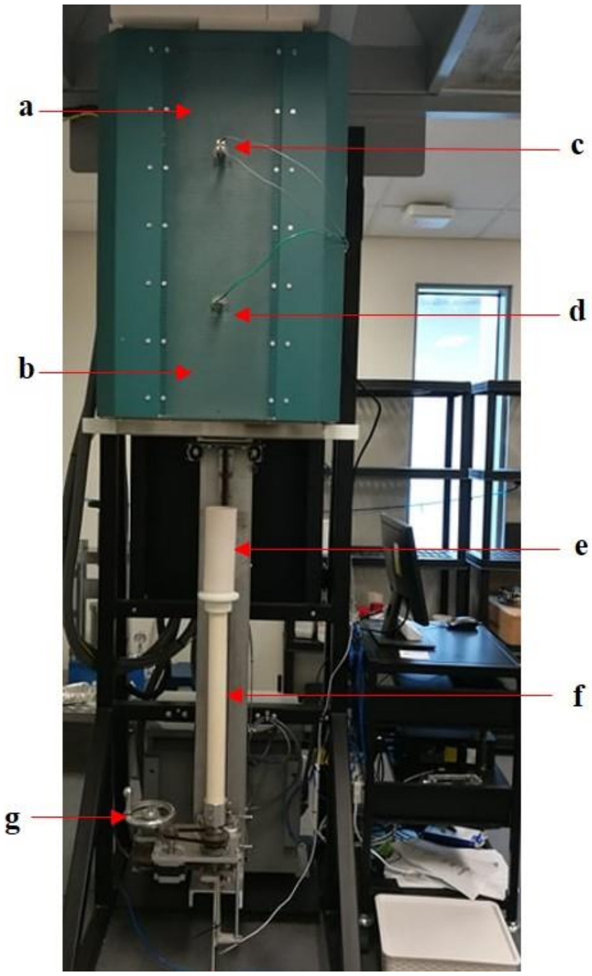

Figure 5.1 Vertical Bridgman furnace used for the experiments: a. zone I (upper), b. zone II (lower), c. thermocouple for zone I, d. thermocouple for zone II, e. alumina cylinder crucible, f. supporting alumina tube, and g. manual lifting.

5.2 Dummy runs 1 and 2

It is important to determine the proper temperature gradient for crystal growth. Furthermore, choosing a proper position for sample melting makes it possible to find the correct point where the material could be congruently melted with sufficient dwell time. To do so, two dummy run experiments were conducted prior to crystal growth. The temperature gradient profile is generated when the charge is being vertically translated from the higher temperature zone (zone I) to the lower temperature zone (zone II). An alumina crucible with inner diameter of 100 mm and height of 220 mm (shown in **Figure 5.2**) was filled with alumina sand that had a particle diameter of 0.1 mm. This sand-filled crucible represented the charge for dummy runs. The charge was then placed on the top of the translation tube. The alumina crucible has a hole 10 mm in diameter at its bottom, and the end of the oxygen flow tube and the probe of the third thermocouple could penetrate through this hole. In other words, the oxygen tube enables us to supply oxygen through the charge while the thermocouple measures the temperature of the charge. As shown in **Figure 5.3**, the probe of thermocouple is 30 mm above the bottom of the crucible. The end of the oxygen tube is 10 mm above the bottom of the crucible. Real images of the thermocouple probe and the oxygen tube end are shown in **Figure 5.4**. The charge was then placed on the top of the translation tube. The charge was lifted up to a position above the adiabatic layer of the furnace or at the beginning of zone I. This position is denoted as the reference position. The charge positions for the next dummy runs and crystal growth were chosen either above or below the reference position. After that, operation was started using ADAPT TCAS computer control. Zone I was heated up at the rate of 1.53 °C/min, while the temperature of zone II was raised at the rate of 1.22 °C/min. When the temperatures of the two zones reached their set points, the temperature of the charge was stabilised at 1345 °C, and the charge then started moving down. The total translation was 150 mm land lasted for 250 h at the rate of 0.6 mm/h. **Table 5.1** lists the conditions for the dummy run experiments.

Figure 5.5 shows the temperature profiles of the two zones and the temperature gradient profiles of the first dummy run experiment. For the first dummy run, the temperatures of zone I and zone II were chosen to be 1380 °C and 1100 °C, respectively.

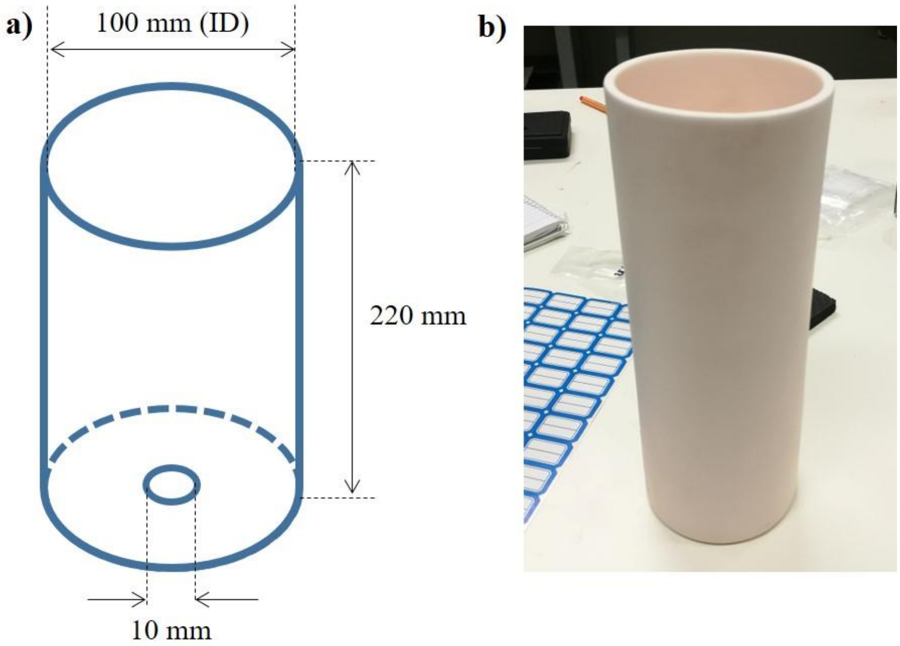

Figure 5.2 Alumina crucible. a) Dimensions of the crucible and b) real image of the crucible.

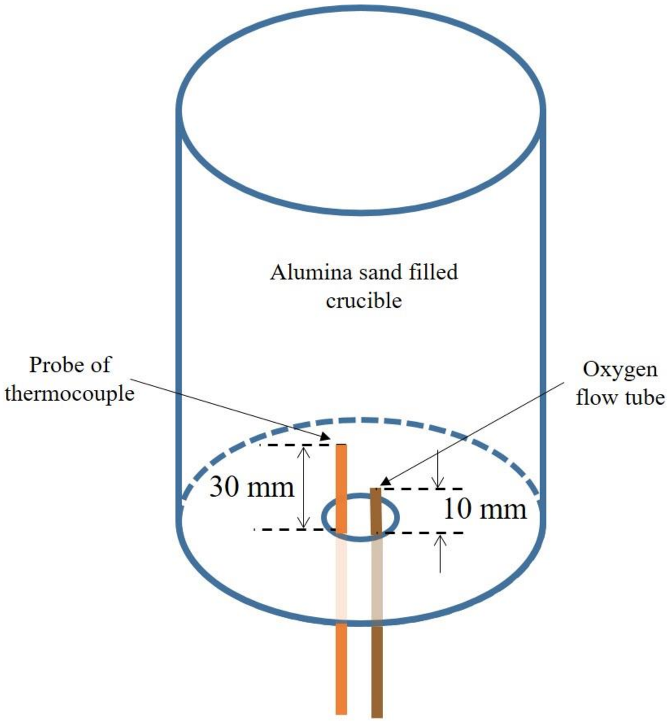

Figure 5.3 Positions of TC probe and oxygen tube inside the alumina crucible.

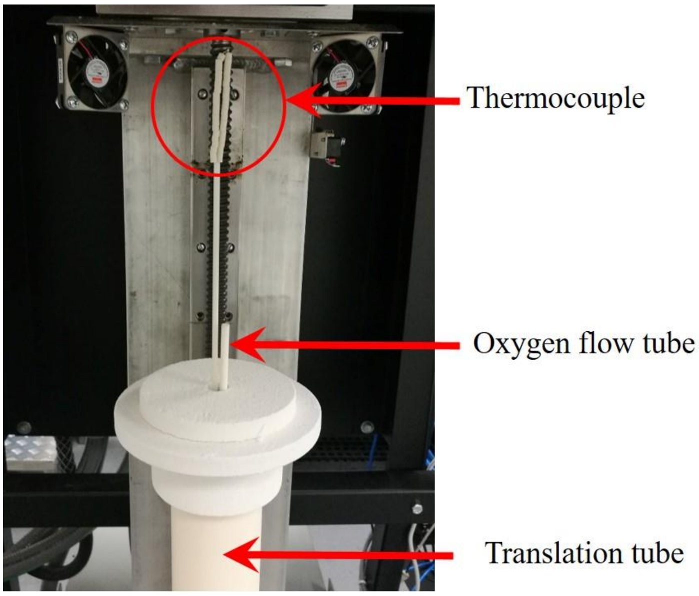

Figure 5.4 Real images of the TC probe and the end of the oxygen flow tube.

Table 5.1 Experimental conditions for dummy runs.

	Zone I temp. (°C)	Zone II temp. (°C)	Charge temp. (°C)	Translation speed (mm/h)	Translation length (mm)	Oxygen flow (m^3/h)
Dummy run 1	1380	1100	1362	0.6	150	-
Dummy run 2	1370	1050	1311	1.0	180	-

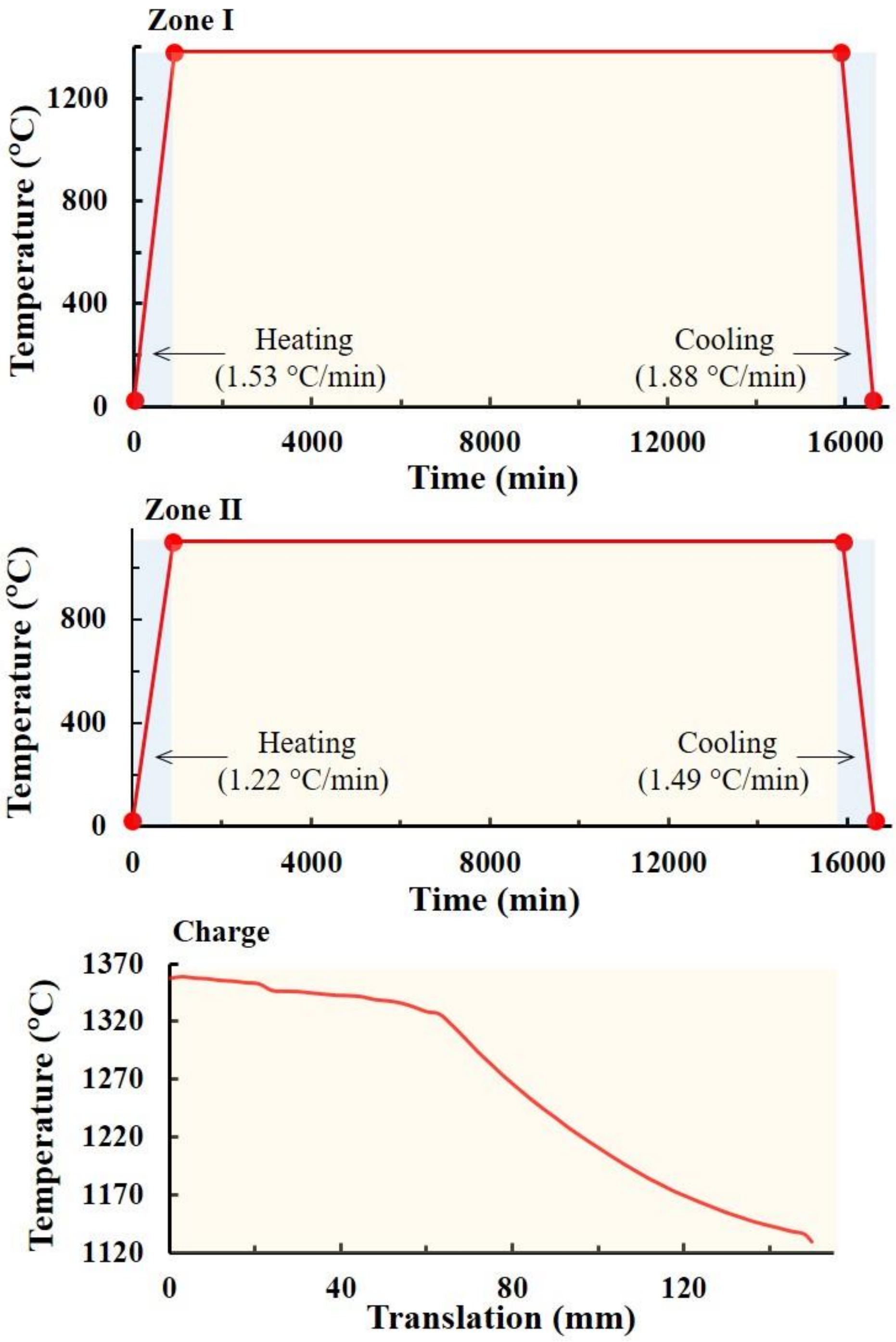

Figure 5.5 Temperature profiles of zone I and II, (upper and middle) and the temperature gradient during the translation (lower) in the dummy run 1 experiment.

In **Figure 5.5** (lower), the average temperature gradient was ~10-14 °C/cm. The optimal temperature gradient for PMN-PT crystal growth, however, is approximately 20 °C [2-5]. Therefore, a sharper gradient must be obtained.

We started the second dummy run with changing the temperatures in zones I and II. The temperatures of zones I and II were set at 1370 °C and 1050 °C, respectively. The charge was prepared in the same way as for the first dummy run. The charge was lifted up to a position 10 mm lower than the reference position that was used for the first dummy run. When the temperatures of zones I and II were brought to their set points, the temperature of the charge was stabilised at 1311 °C. The charge was started translating down at a rate of 1 mm/h. This translation lasted for 180 h. **Figure 5.6** exhibits the temperature gradient profile. For the second run, the average gradient was ~16-18 °C. This is a close value to the optimal gradient point. We hence used similar condition for the first single crystal growth as in the next section.

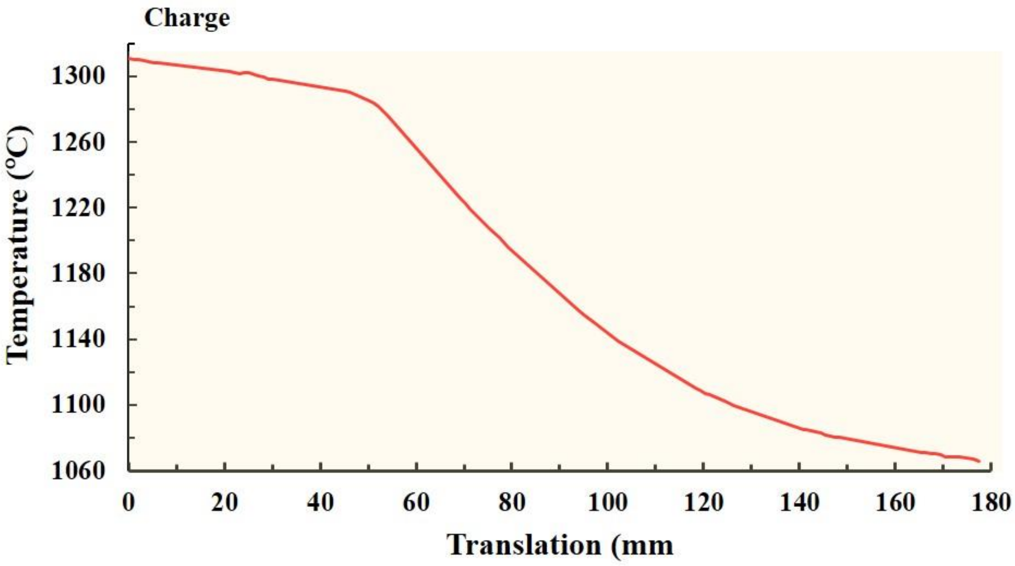

Figure 5.6 Temperature gradient profile during the translation in the dummy run 2 experiment.

5.3 Single crystal growth

5.3.1 The first single crystal growth (PMN-PT)

5.3.1.1 Charge loading

The nominal composition of the first single crystal was 0.71PMN-0.29PT. Two different compositions (0.72PMN-0.28PT and 0.71PMN-0.29PT) of sintered ceramics were used in order to reduce compositional segregation during growth. The ceramic fabrication process is provided in section 4.2.2.2. **Figure 5.7a** and **b** shows the empty Pt crucible and the Pt crucible filled with ceramic pellets, respectively. The mass share of PMN-0.28PT and PMN-0.29PT compositions in Pt crucible is amounted to 42 % and 58 %, respectively. To express clear ratio of two compositions, their amounts were expressed in the unit of mass. Also, to fit into the volume and design of Pt crucible, proper amount of raw material is needed. Hence, masses of each composition pellets were given. In the tapered part of the Pt crucible, PMN-0.29PT pellets 11 mm in diameter (reduced to ~9 mm diameter after sintering) were packed in 7 pieces of small ceramic pellets were used here, and their total mass was approximately 44 g. The cone-shaped part of the crucible was loaded with calcined PMN-0.29PT powder to fill the gap between the tapered and the main cylindrical parts. The main cylindrical part of the Pt crucible was filled with PMN-0.29PT ceramic pellets 25 mm in diameter (< 23 mm diameter after sintering). Roughly 55 g of PMN-0.29PT pellets 25 mm in diameter and 4 pieces of pellets were used here. Furthermore, 142 g of PMN-0.28PT ceramic pellets 25 mm in diameter (<23 mm in diameter after sintering) were added to the Pt crucible, as shown in **Figure 5.7b**. After all the ceramic pellets were added, the Pt crucible was sealed with a Pt lid using micro-welding apparatus in order to prevent PbO evaporation. The charged Pt crucible was then placed in the alumina crucible, as shown in **Figure 5.8**. The gap between the two crucibles was filled with alumina sand with particle diameter of 0.1 mm. The function of this alumina sand is to support the heavy load in the Pt crucible and to adsorb any volatiles from the crystalizing materials. Then the charge in the alumina crucible was placed on the translation tube. The thermocouple probe and oxygen flow tube penetrated through the hole of the alumina crucible, as shown in **Figure 5.3**. The hole in the alumina crucible is shown in **Figure 5.2a**. The probe of the thermocouple was placed 30 mm above the bottom of Pt crucible. Therefore, the third thermocouple measures the temperature around 30 mm in height from the bottom of the charge-containing Pt crucible. Oxygen flow with rate of 1 cc/min was supplied during the crystallization process. The oxygen supply prevents oxygen defects from being generated in the growing crystal [2,3]. Then, the charge was lifted up to Zone I. The charge was located at a position that is 5.0 mm lower than the reference point.

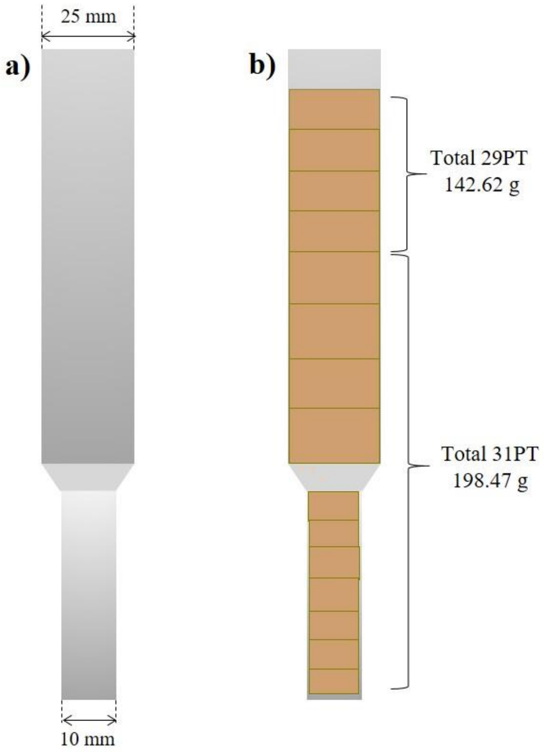

Figure 5.7 Schematic diagram of empty a) Pt crucible and b) crucible filled with ceramic pellets.

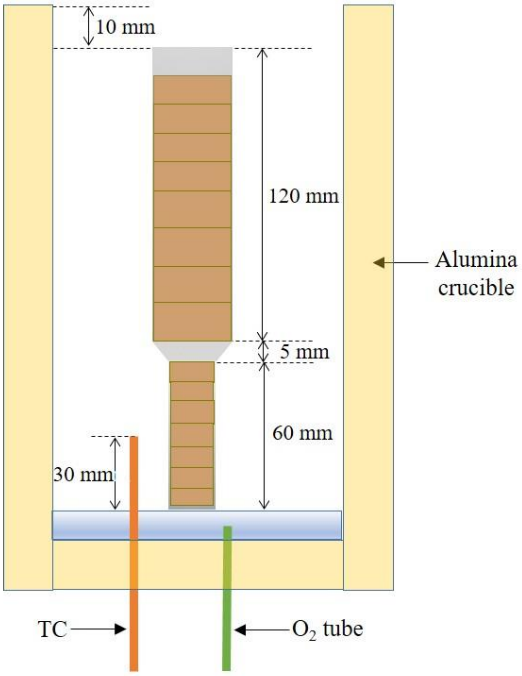

Figure 5.8 Schematic diagram of the charge including the filled Pt crucible, the TC probe and the oxygen flow tube.

5.3.1.2 Single crystal growth

Figure 5.9 shows the temperature profiles of zone I (upper), zone II (middle), and the charge (lower). The temperatures of zone I and zone II were set at 1340 °C and 1050 °C, respectively. The temperature in zone I was reached with a heating rate of 1.5 °C/min. Zone II was heated at a rate of 1.17 °C/min. After the temperatures in zone I and zone II reached the set points, the temperature of the charge

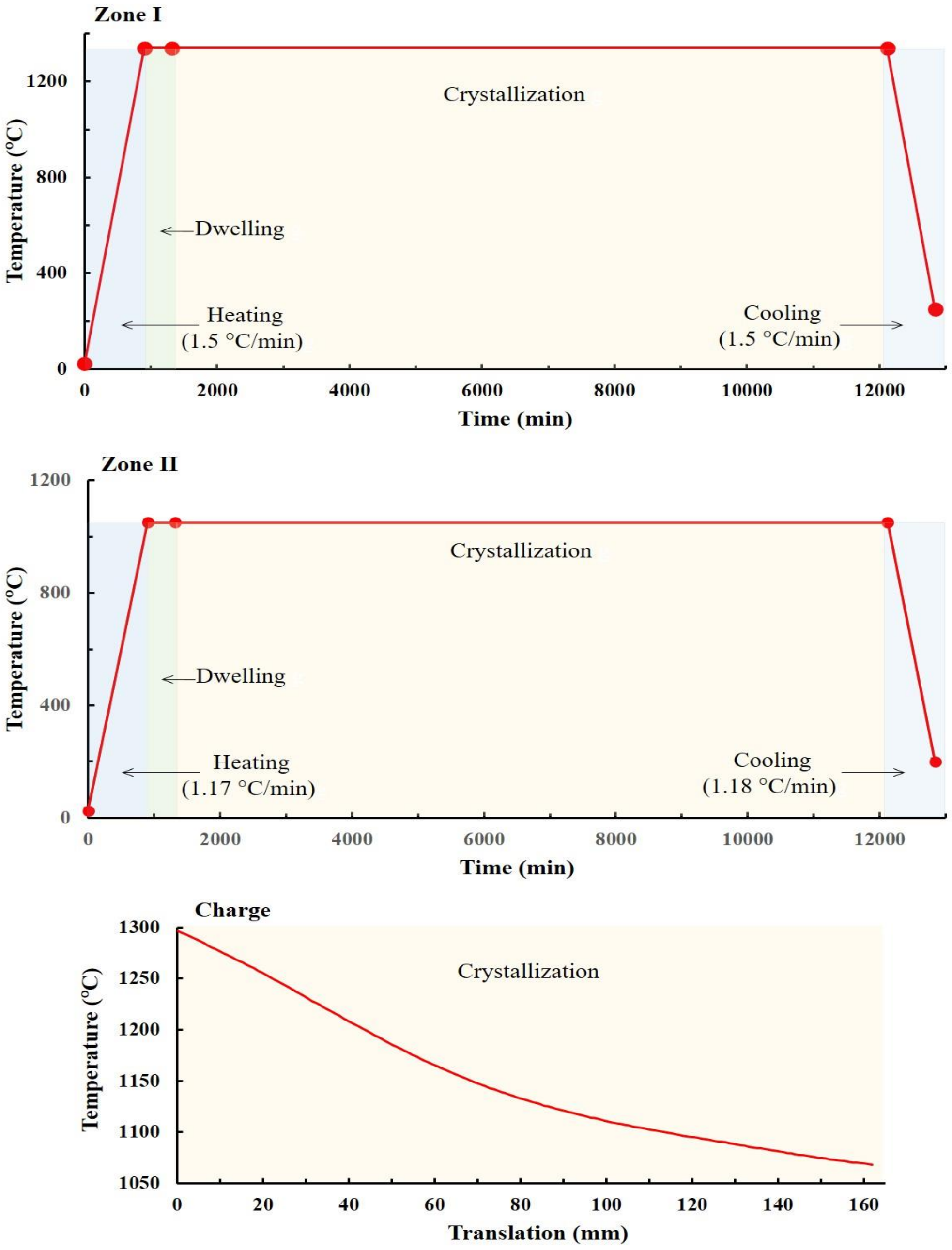

Figure 5.9 Temperature profiles of zones I and II, (upper and middle) and the temperature gradient during the translation (lower) in the first crystal growth (PMN-PT).

was stabilised at 1297 °C. After the charge temperature was stabilised, in order to provide sufficiently melted materials, the charge was given several hours of dwell time [2-4]. In our case, the dwell time for the charge was 5 h. After the 5 h dwell time, the charge began to be moved down. 1 cc/min of oxygen gas was provided to the charge during the translation. The lower panel in **Figure 5.9** shows the temperature profile of the charge translation. The approximate temperature gradient was > 16 °C/cm. The charge translation was moved down 150 mm over the course of 180 h. After the translation was completed, both zones were slowly cooled down. Slow cooling prevented any cracks, damage, or defects in the newly grown crystal [1,3,4]. Zone I was cooled at a rate of 1.5 °C/min to 250 °C, while the temperature of the other zone was cooled at 1.17 °C/min to 200 °C/min. The charge was left overnight to let it cool to room temperature, and the charged alumina crucible was taken from the translation tube. Then, the as-grown single crystal was obtained by ripping off the Pt crucible.

Figure 5.10 shows the as-grown boule. An approximately 150 mm long single crystal was grown. It is evident that the crystallization started 50 mm above the end of the ceramic specimen, indicating that the melting only occurred from this point. It is obvious that the ~50 mm long narrow part is still in the form of ceramic pellets, indicating that this part was not melted. The reason for unmelted ceramic is that the charge was not lifted sufficiently to a position where the ceramic could fully melt in the higher zone.

Figure 5.10 As-grown boule of PMN-PT.

The probe of the third thermocouple was placed 30 mm above the bottom of Pt crucible, as shown in **Figure 5.3**. The temperature was stabilised at 1297 °C during the dwell time of the charge. In the equilibrium phase diagram of the PMN-PT binary system in **Figure 5.11**, the phase equilibrium between solid and liquid near the 0.71PMN-0.29PT composition is approximately at 1305 °C. Therefore, in our experiment, the temperature (1297 °C) near the tapered part of the Pt crucible was lower than the melting point, leaving the unmelted ceramic pellets. It can be seen that crystallization started from the cone-shaped part in **Figure 5.12**. **Figure 5.12** shows a cross-section of conical part in the as-grown boule, proving that it consists of pure crystallized phase. The colour of as-grown crystal was visually dark green brown. However, when a torch was shone through the crystal, slightly colour change was observed. This indicates compositional segregation [2,5-11]. PMN and PT melt at 1340 °C and 1295 °C, respectively. Furthermore, there are wide density differences among the oxide components. For instance, the density of magnesium oxide is 3.58 g/cm^3, while lead oxide has a density of 9.53 g/cm^3. Due to these property variations, the as-grown single crystal could not avoid compositional segregation along the axial direction [2,3]. The compositional segregation leads to that Mg-rich compound appears at the beginning of the crystallized boule, while Ti-rich compound accumulated in the end of the boule [2]. The main

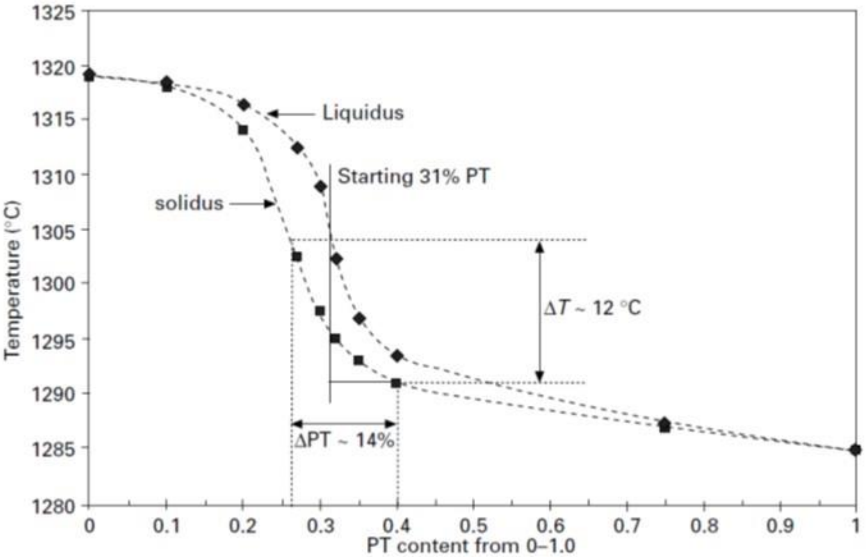

Figure 5.11 Equilibrium phase diagram of PMN-PT binary system [2].

body of the boule is cloudy. **Figure 5.13** shows a cross-sectional cut of the main body of as-grown boule. This cloudy crystal indicates that several domains were nucleated at the top of the tapered part of the Pt crucible. **Figure 5.13** also shows side views of the boule. **Figure 5.14** shows marked grain boundaries in a cross-sectional cut of the as-grown boule. The reason for the creation of several grains was that the crystallization started from a solid-liquid interface at upper level than the expected location. Basically, when crystallization starts through the temperature gradient, several competitive grains are nucleated from the bottom of the at the solid-liquid interface. It is expected that the solid-liquid interface is generated at bottom of the tapered part. Then, when the charge is lowered through the temperature gradient, the grains begin to compete with each other in order to grow further through the tapered part in a vertical direction.

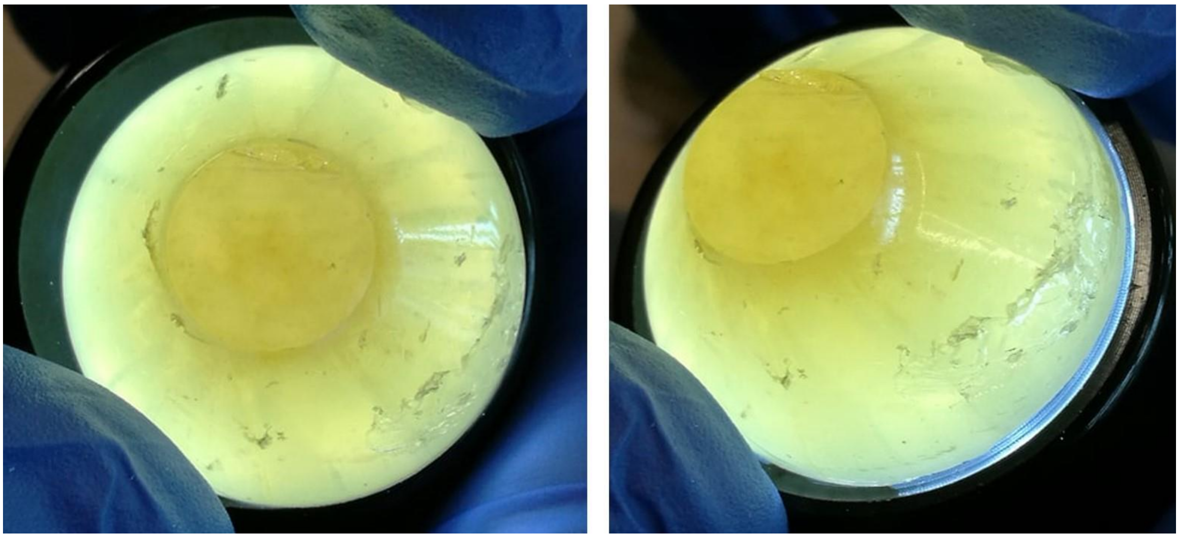

Figure 5.12 Cross-section of cone-shaped part in the as-grown single crystal.

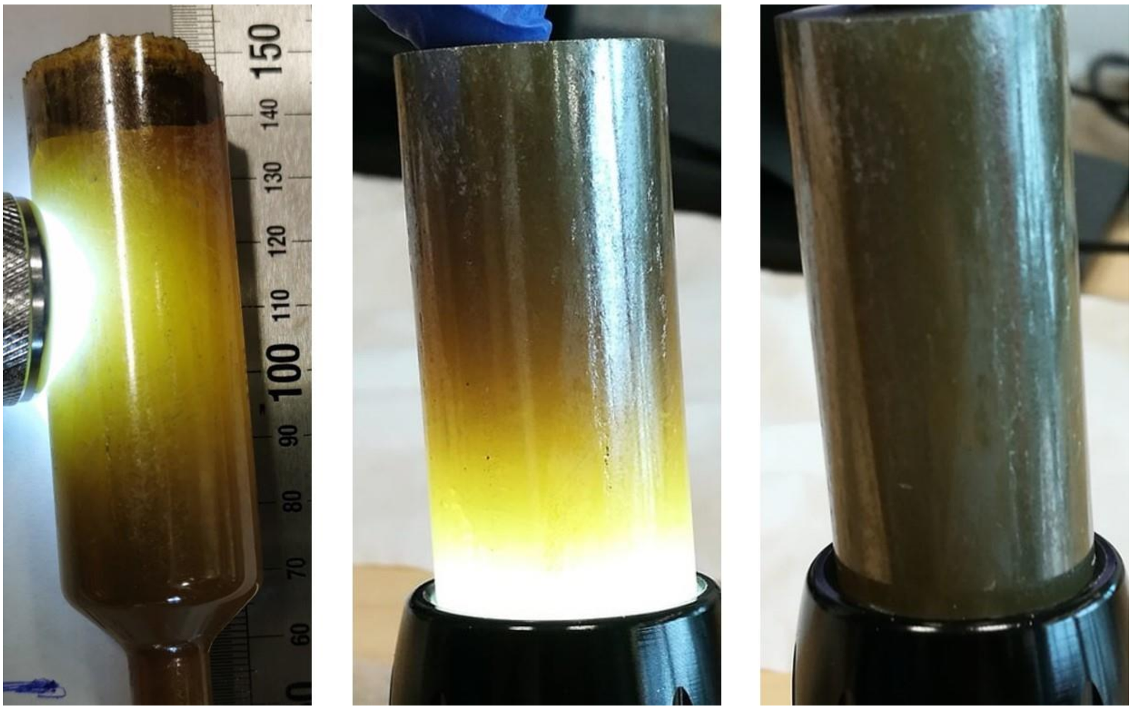

Figure 5.13 The main body of as-grown single crystal.

The most competitive grain will then win and grow advantageously. This completion occurs in the narrow or tapered part of the PT crucible and is the reason for its tapered shape. Furthermore, the temperature gradient profile is shown in the lower panel of **Figure 5.9**, and it indicates that the average gradient is ~16 °C, which is lower than the optimal value [3,4]. This is because the temperature difference between the two zones is not sufficient to create a better value for the temperature gradient. It was suggested that the best temperature gradient is 20 °C/cm for congruent melts of PMN and PT [3,4,9]. The quality of the as-grown single crystal was different from our expectations. Therefore, different growth conditions were investigated to find the optimal ones.

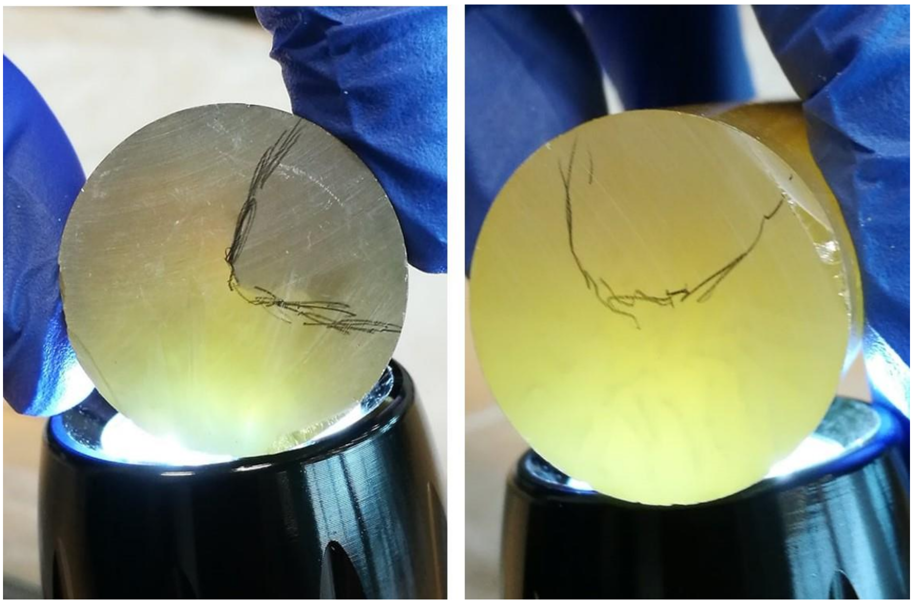

Figure 5.14 Cross-sectional cut of as-grown PMN-PT crystal.

5.3.2 Dummy runs 3 and 4

As learned from the first single crystal growth, it was necessary to re-determine the proper charge position in upper zone (zone I) and to redraw a suitable temperature gradient profile. Dummy run experiments were therefore conducted again. To provide a sufficient temperature gradient, the difference between the two zones' temperatures was set higher than for the first single crystal. The temperatures were set at 1370 °C in zone I and 1000 °C in zone II. In order to find a proper position for the onset of crystallization where the entire ceramic specimen could be melted, the charge position was set 5 mm higher than that of the first single crystal growth experiment. For this dummy run experiment, only the alumina-sand-filled alumina crucible was used to represent the charge. Then, the "charge" was lifted to the targeted position. The temperature profiles of zones I and II are given in **Figure 5.15** (upper) and (middle). The temperature gradient profile is also shown here as a function of translation length (lower). When the temperatures of zones I and II reached their targeted points, the temperature of the charge was stabilised at 1341 °C. This temperature was measured using the third thermocouple, the probe of which was located 30 mm above the bottom of the charge. It can be seen that our experimental charge temperature (1341 °C) is far above the melting point of PMN-PT composition (**Figure 5.11**). Therefore, the position chosen was the right place for the material's melting process. **Figure 5.15** (lower) shows the temperature gradient profile as a function of translation length. Then, the charge was started moving down at the rate of 3 mm/h. Oxygen flow was also supplied during the translation. It can be seen that the average gradient is approximately 20 °C/cm, the optimal value. Therefore, the temperature settings in zones I and II were at the proper points to draw the expected temperature gradient.

The temperature gradients at different temperatures of the zones (dummy run 4) were also investigated. We set temperatures of 1380 °C and 1050 °C for zone I and II, respectively. **Figure 5.16** presents the gradient profile. Here, the charge translation was started from a position that was 5 mm higher than that of reference position. Oxygen flow was also supplied during the translation. It can be seen that the average gradient is approximately 20 °C/cm, the optimal value.

Hence, based on results of dummy runs 3 and 4, and the published literature, it could be expected that these conditions would be good for relaxor-PT single crystals. We used those condition for the next single crystal growth, and the details of the results will be presented in the next sections.

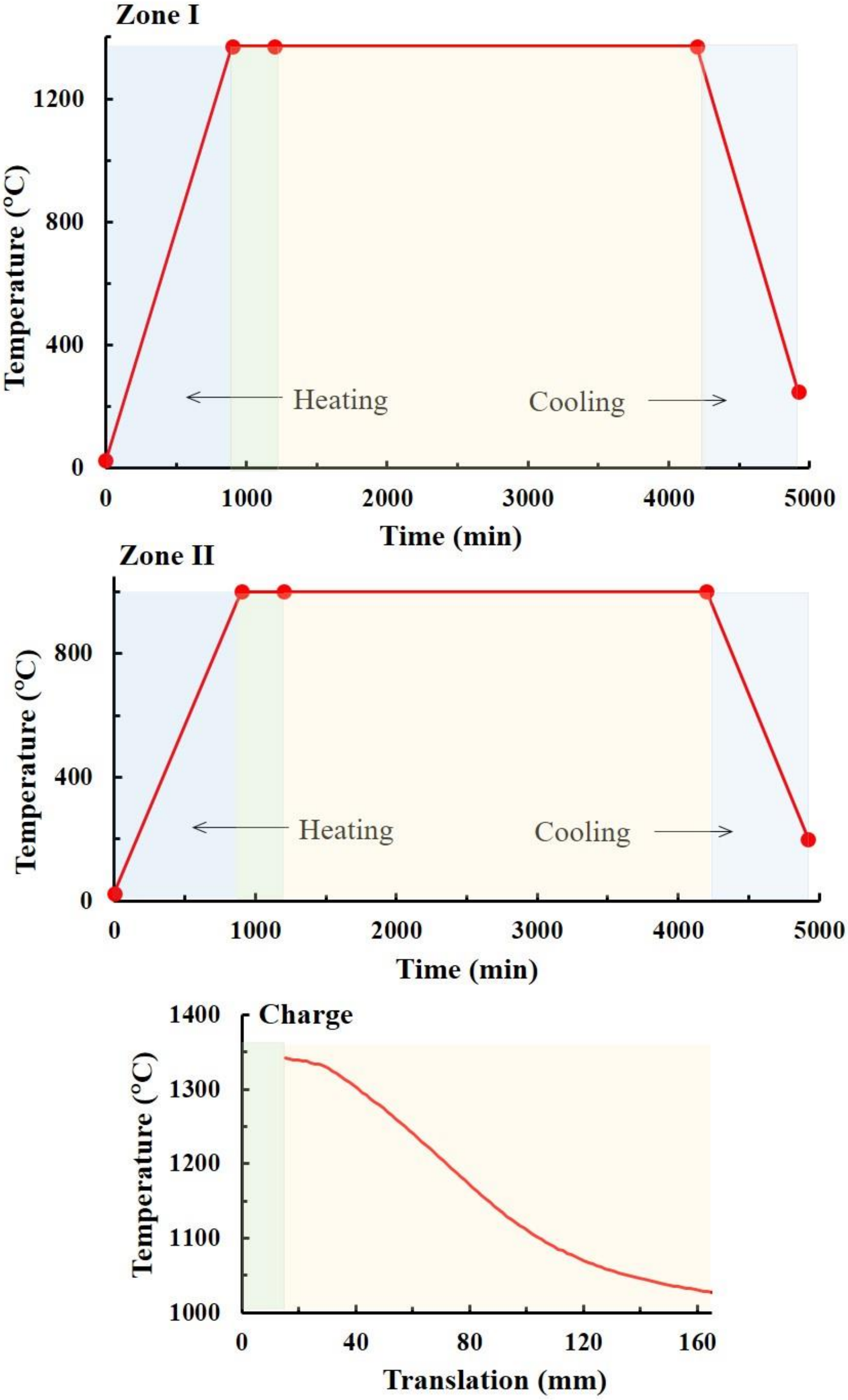

Figure 5.15 Temperature profiles of zone I and II, (upper and middle) and temperature gradient during the translation (lower) in dummy run 3.

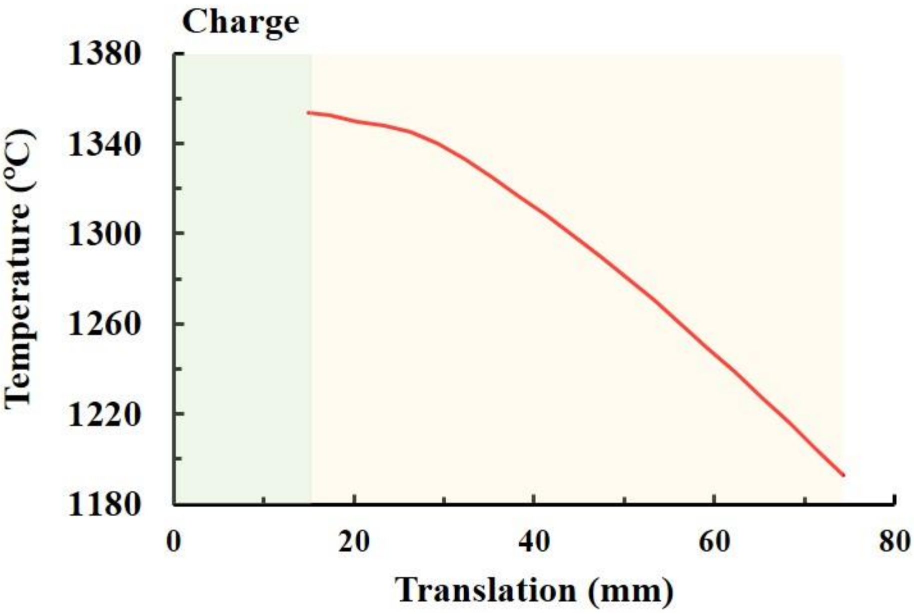

Figure 5.16 Temperature gradient profile during the translation in the dummy run 4 experiment.

5.3.3 Second single crystal growth (Sm-PMN-PT)

5.3.3.1 Charge loading

The composition of the second single crystal was based on 0.01Sm-0.72PMN-0.28PT and 0.01Sm-0.71PMN-0.29PT. To reduce compositional segregation, two compositions were used. The Sm-doped ceramic sample preparation is given in section 4.2.2.3. A schematic diagram of the ceramic-filled Pt crucible is shown in **Figure 5.17**. 7 pieces of small ceramic pellets of Sm-PMN-0.29PT were introduced into the tapered part of Pt crucible. The cone-shaped part of the crucible was filled with Sm-PMN-0.29PT powder. 4 pieces of ceramic pellets were added to the main cylinder part of the crucible, and the total mass of Sm-PMN-0.29PT was 192.6 g. Above them, 4 pieces of Sm-PMN-0.28PT ceramic pellets were added, and their total mass was 134.7 g. To express clear ratio of two compositions, their amounts were expressed in the unit of mass.

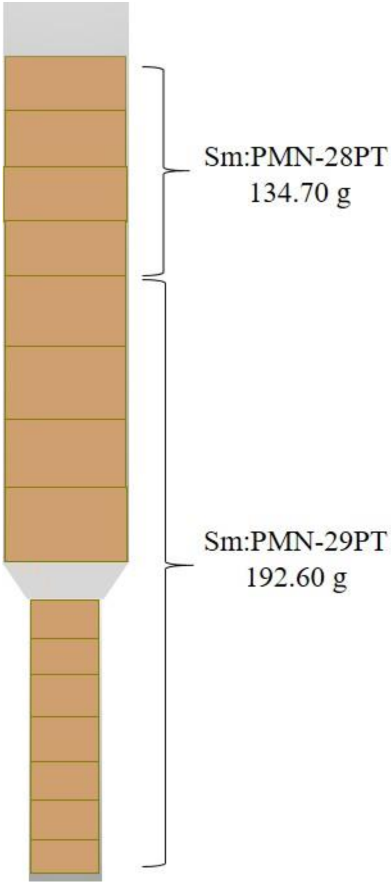

Figure 5.17 Schematic diagram of Pt crucible filled with Sm-PMT-PT ceramics.

The platinum crucible was then sealed with a platinum lid, and the charged crucible was then put into the alumina crucible. Alumina sand was poured into space between the two crucibles. The charged alumina crucible was placed on top of the translation tube, and the charge was lifted up. The probe of the third thermocouple was 30 mm above the bottom of the platinum crucible. Oxygen flow was supplied during the crystallization.

5.3.3.2 Single crystal growth

The crystal growth conditions used for this experiment were based on results of dummy runs

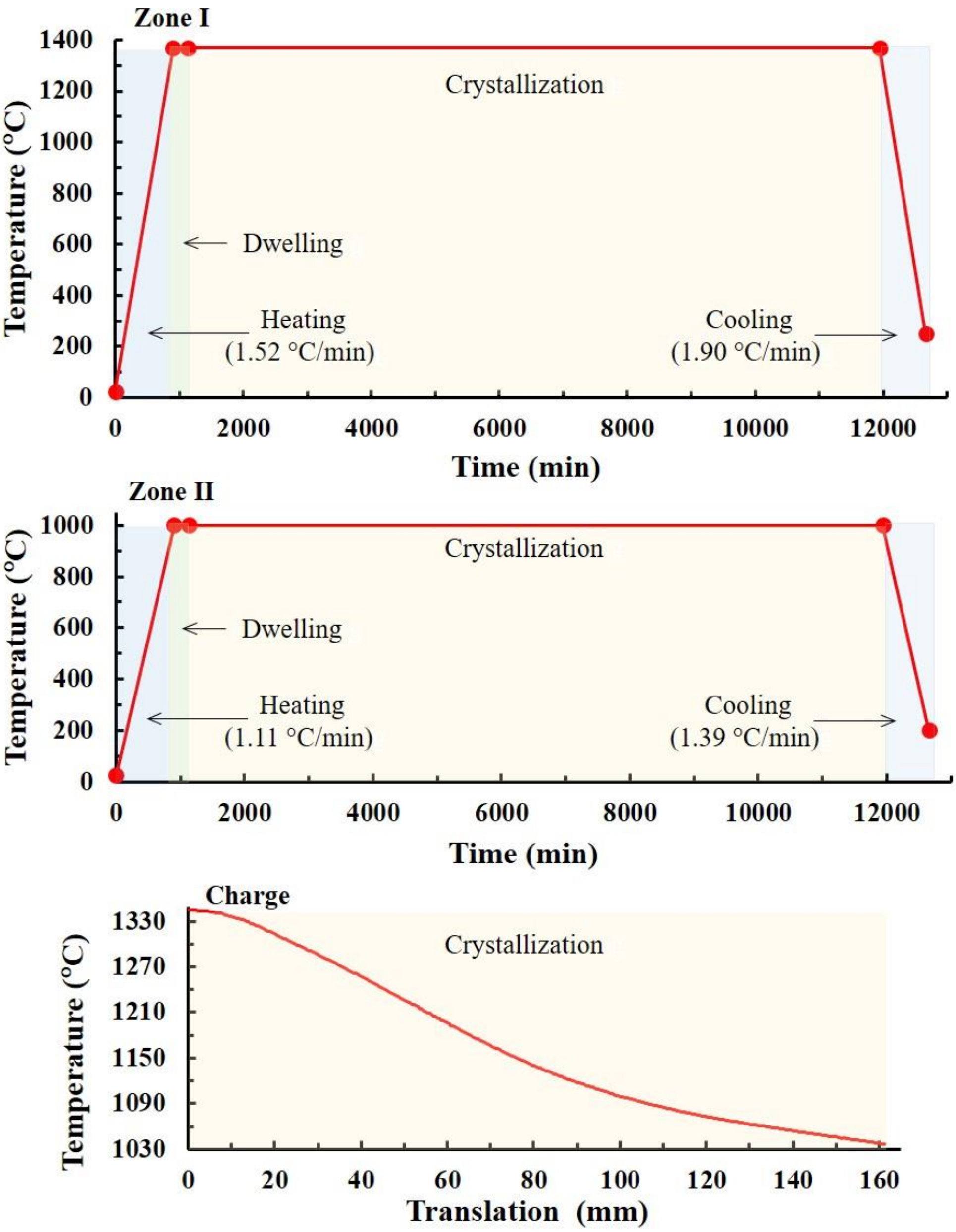

Figure 5.18 Temperature profiles of zones I and II, (upper and middle) and the temperature gradient during the translation (lower) for the second single crystal (Sm-doped PMN-PT).

3 and 4. The temperatures of zones I and II were set at 1370 °C and 1000 °C. This time, the temperature difference between two zones was larger than for the first single crystal growth. The charge was lifted to a position that was 5 mm higher than that for the first single crystals growth. **Figure 5.18** shows the temperature profiles of zones I and II during the crystal growth. This figure also includes the temperature gradient profile of the charge as a function of translation length. When temperatures of zone I and II

reached their set points, the temperature of the charge was stabilised at 1340 °C, which was sufficient for fully melting the ceramic materials in the Pt crucible. After a 4 h dwell time, the charge was moved down at the rate of 0.9 mm/h. The total length of the translation was 162 mm. The crystallisation lasted for 180 h. The average temperature gradient was ~20 °C/cm. After the translation of the charge was stopped, zone I was cooled down to 250 °C at the rate of 1.90 °C/min while the temperature of zone II was lowered to 200 °C at the rate of 1.39 °C. The slow cooling prevented any cracking of damage to the newly-grown single crystal. After the temperatures were reached the targeted points, the charge was kept in the furnace chamber overnight. Then, the charge was taken out from the furnace. The newly-grown boule was collected from the platinum crucible by ripping it off.

Figure 5.19 shows the as-grown boule of Sm-doped PMN-PT single crystal. A single crystal was grown approximately 150 mm in length. The colour of the boule changed from dark yellow and orange at the narrow end to dark brown at the other end, signifying compositional segregation.

Figure 5.19 As-grown boule of Sm-PMN-PT.

Figure 5.20 shows the grown crystal from the tapered part. It confirms that, this time, the ceramics in the tapered part were all melted so they were grown into crystallised material. It shows that a pure and transparent high-quality crystal started growing from the narrow part. To compare with the first crystal growth, in this growth, only a single grain was grown. The main body of the as-grown boule is shown in **Figure 5.21**.

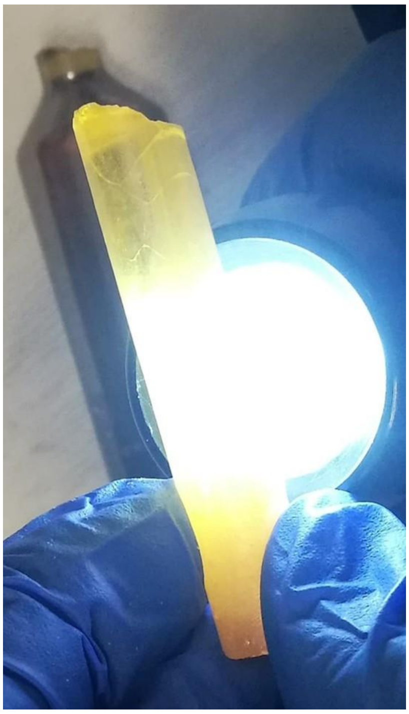

Figure 5.20 Tapered as-grown boule of Sm-PMN-PT.

When torch light was incident on the as-grown boule along the axial direction, the compositional segregation could be seen. Near the conical part of the boule, there was pure and transparent single crystal. The boule became slightly cloudy in the middle and dark brown coloured at the end. This could be due to compositional segregation. Some cracks were appeared, which could have been caused by the large c/a ratio in the tetragonal phase and generate the cracks during the cooling.

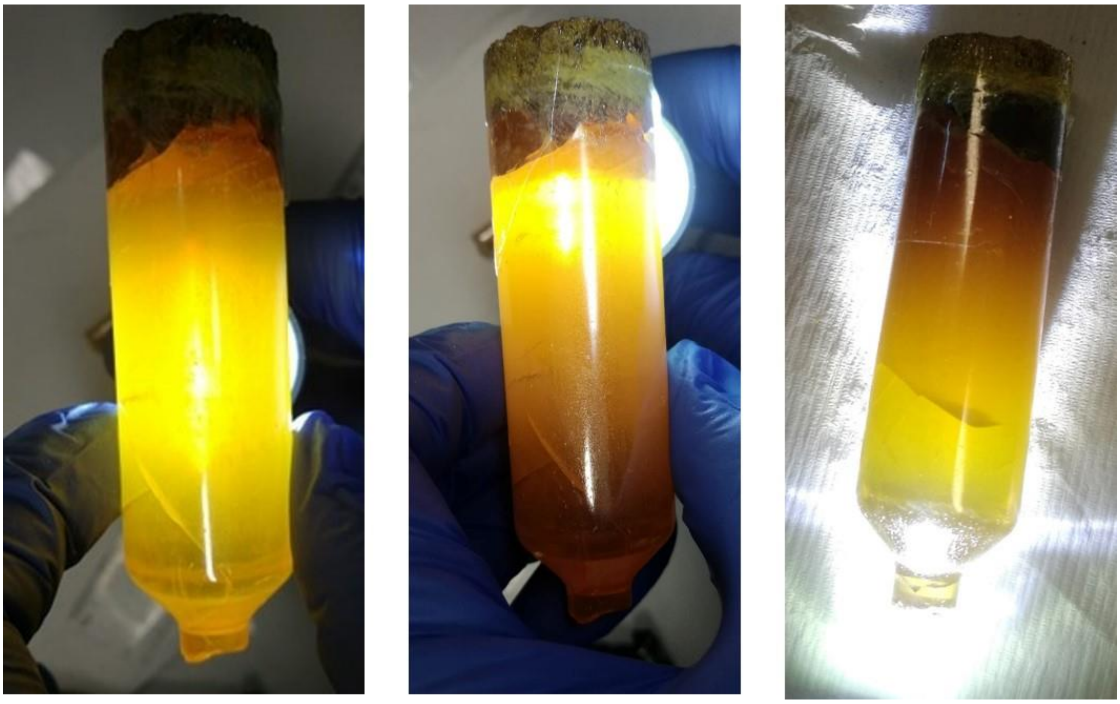

Figure 5.21 The main body of as-grown Sm-doped single crystal.

This time, the conditions were right for crystal growth because the physical appearance of the boule in the figures above confirms the good-quality of single crystal.

5.3.4 Third single crystal growth (Mn-PIN-PMN-PT)

5.3.4.1 Charge loading

The composition of the third single crystal was 0.28PIN-43PMN-0.29PT-0.01Mn. 8 pieces of small Mn-modified ceramic pellets were introduced into the tapered part of the Pt crucible, as shown in **Figure 5.22**. To fit into the volume and design of Pt crucible, proper amount of raw material is needed. Hence, total mass of pellets was given. Another 8 big pellets were added into the main cylindrical part. The conical part of the crucible was filled with powder of the same composition. The platinum crucible was sealed with a platinum lid to minimise evaporation of compounds at high temperature during the crystal growth. The sealed platinum crucible was put into the alumina crucible. The space between two crucibles was filled with alumina sand for support of the charged platinum crucible and adsorption of any evaporated materials at high temperature. The charged alumina crucible then put on the top of the translation tube. The charge was lifted up to a position 5 mm above the reference position.

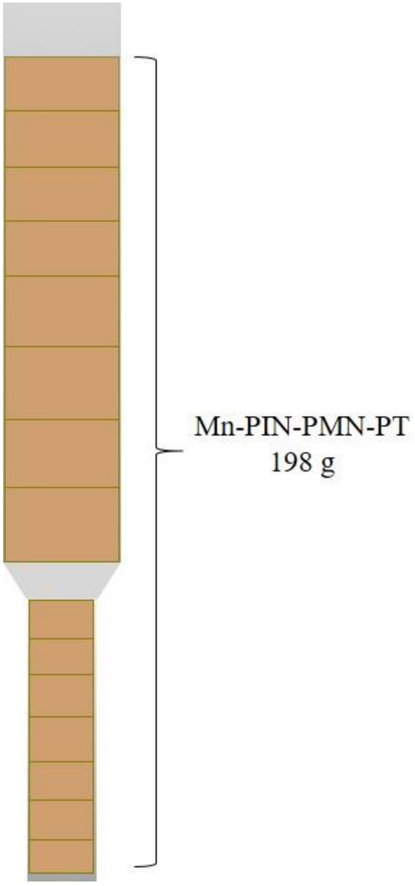

Figure 5.22 Schematic diagram of Pt crucible filled with Mn-PIN-PMT-PT ceramics.

5.3.4.2 Crystal growth

Based on the obtained results of dummy runs 3 and 4, the same conditions were used for the third crystal growth. The temperatures profiles of the two zones are shown in **Figure 5.23**. Temperatures in the higher (zone I) and lower zones (zone II) were 1360 °C and 1000 °C, respectively. The charge temperature was stable at 1330 °C. This temperature was sufficient for congruently melting for the composition considering the melting temperature of the ternary compound (approximately 1300 °C) [12]. After the charge temperature was stabilised, a 4 h dwell time was applied. After dwelling, the translation was started. The translation starting positions was also same as that of the second single crystal growth. The temperature gradient profile is shown in the lower part of **Figure 5.23**. The average temperature gradient was ~20 °C/cm. Hence, temperature difference between the two zones was sufficient for an adequate gradient. The charge translation was 145 mm long and lasted for 160 h. After the translation was completed, the temperatures of the two zones were cooled at the rates of 1.11 °C/min and 1.39 °C/min to 250 and 200 °C, respectively, to avoid any cracking or damage to the as-grown crystal. The as-grown boule of Mn-modified PIN-PMN-PT is shown in **Figure 5.24**. The dark colour is due to the influence of the manganese ions. Under incident torchlight, the dark brown pure crystal is revealed. A single crystal approximately 160 mm was grown. In the case of the Mn-doped single crystal, it is hard to review the physical appearance of the as-grown boule. When torch light was incident on the crystal, some features appeared. When liga1ht was shone on the tapered part of as-grown boule along the axis direction, it can be seen that a dark brown colour appeared (**Figure 5.25**). In **Figure 5.26**, there is a small crack on the end of tapered part where the crystallized compound is seen. This crack is not related to the grown process but it is only mechanical damage that was occurred when we ripped the Pt crucible to separate from the as-grown single crystal. As seen from its physical appearance, pure and high-quality single crystal was grown.

The results for the third single crystal growth proved that good quality single crystal could be successfully grown.

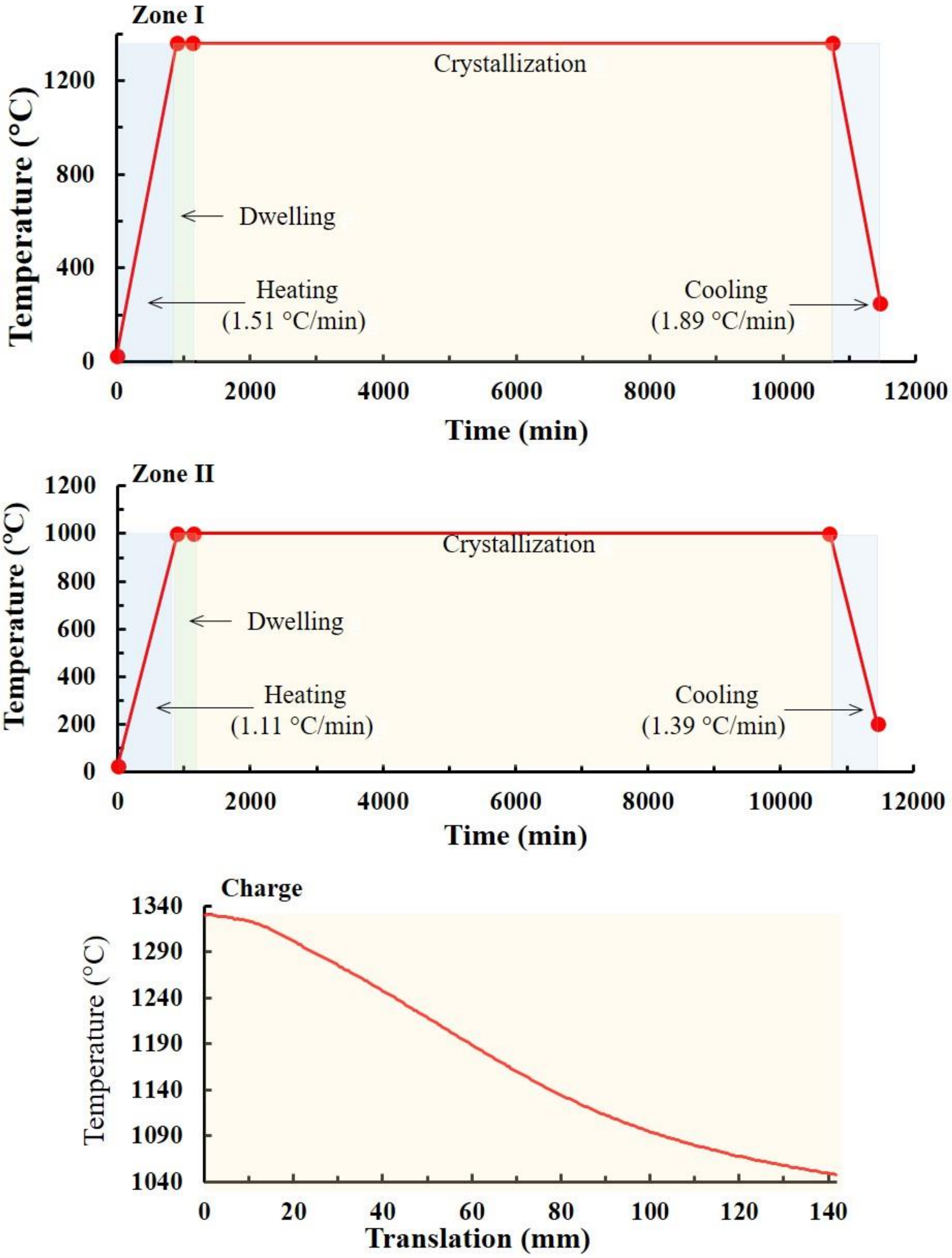

Figure 5.23 Temperature profiles of zones I and II, (upper and middle) and the temperature gradient during the translation (lower) for the third single crystal (Mn-doped PIN-PMN-PT).

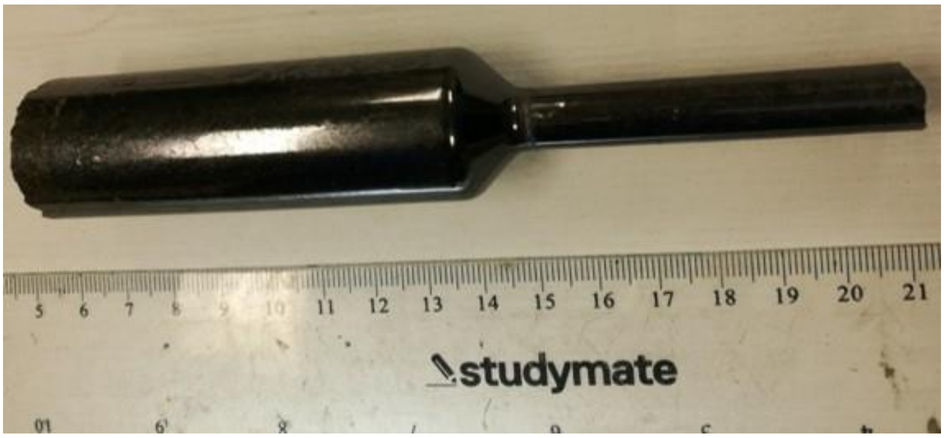

Figure 5.24 As-grown single crystal of Mn:PIN-PMN-PT.

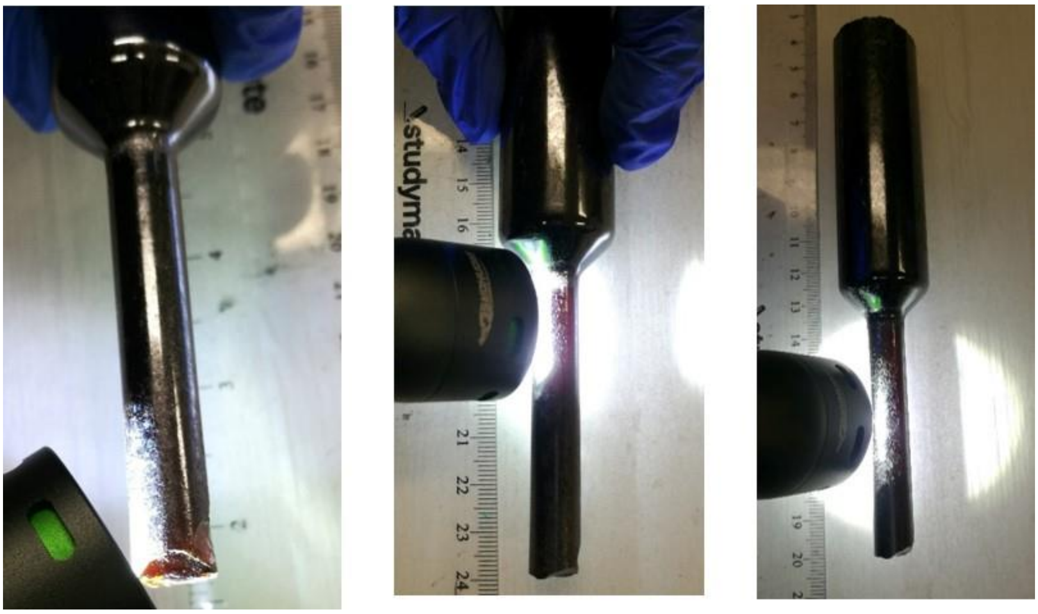

Figure 5.25 Mn-PIN-PMN-PT single crystal under torch light.

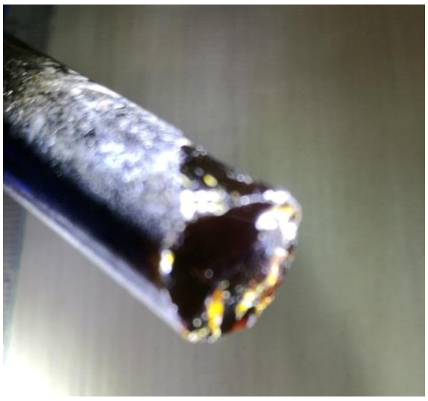

Figure 5.26 End of the as-grown boule.

5.4 Future work

In the future, it is planned to characterize the grown single crystals. A certain crystallographic orientation is dominantly developed when the single crystal is being grown. Therefore, it is necessary to determine the orientation of developed facets. To detect the orientation, the Laue X-ray diffraction method will be used. In our team's current project, the Laue X-ray diffraction equipment was already planned to install in our laboratory. After administrative and financial discussions are finalized, new equipment will be set in our laboratory, enabling us to determine the orientation of our grown single crystals. Once orientations are experimentally defined, sample preparation procedures will be followed, including cutting, polishing, annealing and electroding. The compositional heterogeneity will be studied along growing direction using the Curie temperature. Also, dielectric and piezoelectric properties will be investigated.

The as-grown single crystals will be used to study the ultra-high piezoelectric phenomenon, doping effect, and property improvement research in relaxor-ferroelectric materials. Also, these sample could be employed for applications. Especially, the single crystal could be experimented for underwater acoustic devices. All of these follow-up plans will be undertaking with collaborations of partner researchers and teams.

5.5 Conclusion

To obtain the temperature gradient and to test the operation of the vertical Bridgman furnace, several dummy run experiments were conducted.

Prior to single crystal growth, several dummy run experiments were conducted. PMN-PT single crystal was grown from two compositions: PMN-0.29PT and PMN-0.31PT to reduce compositional segregation. The bottom part of the ceramic sample in the Pt crucible was found to be unmelted. This indicated that the charge was not lifted to a position where the entire sample could melt. Also, the difference in temperature was observed to be insufficient to provide a proper temperature gradient. Therefore, the growth conditions needed to be optimized for growth of high-quality single crystal. From these results, in next dummy run experiments, the difference between the temperatures of the two zones was increased to obtain a steeper temperature gradient. Also, the charge was lifted up to higher position for fully congruent melting. As a result, we successfully grew high-quality of Sm-doped PMN-PT and Mn-doped PIN-PMN-PT single crystals under the new growth conditions.

References

[1] S. L. Swartz and T. R. Shrout, Fabrication of perovskite lead magnesium niobate, *Mater. Res. Bull.*, **17**, 1245–5120 (1982).

[2] P. Han, J. Tian, and W. Yan, Bridgman growth and properties of PMN-PT-based single crystals. In *Handbook of Advanced Dielectric, Piezoelectric and Ferroelectric Materials: Synthesis, Properties and Applications*; Ye, Z.G., Ed.; Woodhead: Cambridge, UK, 2008; pp. 3–37.

[3] W. Hackenberger, J. Luo, X. N. Jiang, K. A. Snook, P. W. Rehrig, S. J. Zhang, and T. R. Shrout, Recent developments and applications of piezoelectric crystals. In *Handbook of Advanced Dielectric, Piezoelectric and Ferroelectric Materials–Synthesis, Characterization and Applications*; Ye, Z.G., Ed.; Woodhead: Cambridge, UK, 2008; pp. 73–100.

[4] J. Lu, and S. Zhang, Advances in the growth and characterization of relaxor-PT-based ferroelectric single crystals, *Crystals*, **4**, 306-330 (2014).

[5] K.T. Zawilski, M. Custodio, C. Claudia, R.C. DeMattei, S.G. Lee, R.G. Monteiro, H. Odagawa and, R.S. Feigelson, Segregation during the vertical Bridgman growth of lead magnesium niobate–lead titanate single crystals, *J. Cryst. Growth*, **258**, 353–367 (2003).

[6] H. Luo, G. Xu , P. Wang, Z. Yin, Growth and characterization of relaxor ferroelectric PMNT single crystals, *Ferroelectrics*, **231:1**, 97-102 (1999).

[7] Z. W. Yin, H. Luo, P. C. Wang, G. S. Xu, Growth, characterization and properties of relaxor ferroelectric PMN-PT single crystals, *Ferroelectrics*, **229**, 207-216 (1999).

[8] K. Song, Z. Li, H. Guo, Z. Xu, and S. Fan**,** Compositional segregation and electrical properties characterization of [001]- and [011]-oriented co-growth $Pb(In_{1/2}Nb_{1/2})O_3$-$Pb(Mg_{1/3}Nb_{2/3})O_3$ $PbTiO_3$ single crystal, *J. Appl. Phys.*, **123**, 154107 (2018).

[9] W. Zhang, Z. Wang, X. Yang, X. Long, and C. He, Composition uniformity of $Pb(In_{1/2}Nb_{1/2})O_3$-Pb $(Mg_{1/3}Nb_{2/3})O_3$-$PbTiO_3$ single crystals grown in ⟨001⟩ direction, *J. Cryst. Growth*, **560**, 126061 (2021).

[10] W. Cao, Full-set material properties and domain engineering principles of ferroelectric single crystals. In Handbook of Advanced Dielectric, Piezoelectric and Ferroelectric Materials; Ye, Z.G., Ed.; Woodhead: Cambridge, UK, 2008; pp. 235–265.

[11] H. Luo, G. Xu, H. Xu, P. Wang, and Z. Yin, Compositional homogeneity and electrical properties of lead magnesium niobate titanate single crystals grown by a modified Bridgman technique. *Jpn. J. Appl. Phys*. **39**, 5581 (2000).

[12] S. Zhang, F. Li, N. P. Sherlock, J. Luo, H. J. Lee, R. Xia, R. J. Meyer Jr, W. Hackenberger, and T. R. Shrout, Recent developments on high Curie temperature PIN–PMN–PT ferroelectric crystals, *J. Cryst. Growth* 318, 846–850 (2011).

Chapter 6. Conclusions

We have reviewed the recent development of relaxor-PT single crystals. The review includes the single crystal growth methods, property improvement approaches, anisotropic features, and application perspectives based on the recent progress. The modified Bridgman growth and solid-state conversion growth methods are discussed in the review because the crystal products of these methods are the most suitable for scientific and commercial applications. The property improvement part of the review investigated the recent progress of the doping and poling strategies. Donor-doping offers dramatic enhancement of the piezoelectric and electromechanical properties in relaxor-PT ferroelectric crystals. Acceptor-doping in relaxor-PT crystals endows them with a higher mechanical quality factor that for un-doped single crystals. All this progress offers great potentials for dramatic enhancement of their potential for electromechanical applications. This work was published as a review article in in *L. Baasandorj and Z. Chen, Crystals **2022**, 12, 56* [1].

It is necessary to use sintered ceramic samples for congruent-melting of compounds and grow pyrochlore-free single crystals [2-4]. Ceramic samples were therefore prepared for single crystal growth. Before the fabrication of polycrystalline samples for crystal growth, their properties were investigated to check their quality. The ceramic fabrication conditions were also studied to determine the optimal conditions. For ceramic fabrication, the optimal calcination temperature was found to be 830-850 °C. When the temperature was lower than 830 °C, the high-temperature reaction was not completed. When this temperature was higher than 850 °C, some compounds were easily volatilised, and mass loss was increased. The calcination period was set at 4-6 h. For sintering, the optimal temperature and time period were found to 123-1270 °C and 4 h. At lower temperatures and shorter periods than those of the optimal conditions, sintering was not completed. Also, at higher temperatures and longer periods, Pb-compounds were easily volatilised, and mass loss was increased. The densities of samples fabricated under optimal conditions were 94-97% of their theoretical values. The dielectric and piezoelectric properties of the fabricated ceramics were studied and compared to references. The results of the dielectric and piezoelectric responses were quite close to those of the reference values. The results of the ceramics characterization indicate that high-quality ceramic samples were prepared.

In this work, three single crystals were grown. The first crystal to be grown was PMN-PT single crystal. To reduce the compositional segregation, two compositions, PMN-0.28PT and PMN-0.29PT, were used. In this growth, the lower part of the raw ceramic material in the PT crucible was not melted. This was because the charge was not placed up to a position where the entire ceramic sample could melt. Also, the temperature difference between the two zones was not sufficient to provide a proper temperature gradient. The color of the single crystal was cloudy brown. Several grains appeared to have been nucleated in the conical part of the Pt crucible, and most of them were grown along the axis direction. After that, two more dummy run experiments were conducted. Using these experiments, we obtained the optimal temperature gradient and charge position. In accordance with the dummy run experiments, the samples for the next crystal growths were lifted to a higher position. Also, proper temperatures were provided. Consequently, the single crystals of the Sm-doped PMN-PT and Mn-doped PIN-PMN-PT compositions were successfully grown. In the case of the Sm-doped PMN-PT single crystal, two compositions (Sm-PMN-0.28 and Sm-PMN-0.29PT) were applied. The as-grown boule of Sm-doped PMN-PT was transparent and orange-brown in color. In the case of the Mn-modified single crystal, only the 0.28PIN-43PMN-0.29PT-0.01Mn composition was used. The physical appearance of this single crystal indicated that a good quality single crystal had been fabricated.

References

[1] L. Baasandorj, and Z. Chen, Recent developments on relaxor-$PbTiO_3$ ferroelectric crystals. *Crystals*, **12**, 56 (2022).

[2] P. Han, J. Tian, and W. Yan, Bridgman growth and properties of PMN-PT-based single crystals. In *Handbook of Advanced Dielectric, Piezoelectric and Ferroelectric Materials: Synthesis, Properties and Applications*; Ye, Z.G., Ed.; Woodhead: Cambridge, UK, 2008; pp. 3–37.

[3] J. Luo and S. Zhang, Advances in the growth and characterization of relaxor-PT-based ferroelectric single crystals. *Crystals*, **4**, 306–330 (2014).

[4] S. L. Swartz and T. R. Shrout, Fabrication of Perovskite Lead Magnesium Niobate, *Mater. Res. Bull.*, **17**, 1245–50 (1982).

Appendix Publication

L. Baasandorj, and Z. Chen, Recent developments on relaxor-$PbTiO_3$ ferroelectric crystals. *Crystals*, **12**, 56 (2022).